

Surface-confined metalloporphyrin complexes



John-Patrick Beggan B.Sc.
Dublin City University
School of Physical Sciences

A thesis submitted for the degree of
Doctor of Philosophy

Supervisor
Dr. A. A. Cafolla

July 2013

Declaration

I hereby certify that this material, which I now submit for assessment on the programme of study leading to the award of Doctor of Philosophy is entirely my own work, that I have exercised reasonable care to ensure that the work is original, and does not to the best of my knowledge breach any law of copyright, and has not been taken from the work of others save and to the extent that such work has been cited and acknowledged within the text of my work.

Signed: _____(Candidate) ID No.: _____

Date: _____

Dedication

For my Parents

Acknowledgements

First and foremost, I would like to thank my supervisor, Dr. Tony Cafolla, for giving me the opportunity to carry out this research. His guidance and great patience were invaluable in bringing this thesis to fruition. I would also like to extend my gratitude to Dr. Mary Pryce and Prof. Matthias Senge for their significant contribution to this work. I wish to thank Dr. Sergey Krasnikov for his support and tutorship during my early years. My thanks also to the academic and support staff of the DCU School of Physical Sciences for their help throughout the course of this work.

I must thank my lab mates, both past and present, whose warmth and friendliness made the day to day experience a real pleasure: Claire, Catherine, Hooi-Ling, John and Tom. As well as working alongside some great people, I have been fortunate to follow old friends to DCU and to have met some new ones too; a special thanks to Wayne, Paddy and Barry. Monika you are forever in my gratitude; thanks too for helping with the structures.

Lastly, and most importantly, I owe my deepest gratitude to my Parents and Brother. Without the unconditional support of my Parents, none of this would have been possible. To finish I must include a heartfelt, Alleluia!

Contents

Declaration	ii
Dedication	iii
Acknowledgements	iv
Contents	v
Abstract	viii
1 Introduction	9
1.1. Concerning porphyrins	9
1.1.1. Conformational flexibility	9
1.1.2. Biomimetic catalysis	11
1.1.3. On-surface synthesis	12
1.2. Thesis outline	13
1.3. References	15
2 Experimental methods	19
2.1. Surface sensitive techniques	19
2.1.1. Scanning tunnelling microscopy	19
2.1.2. Low energy electron diffraction	21
2.1.3. X-ray photoelectron spectroscopy	23
2.2. Ultra-high-vacuum system	24
2.3. Substrates	26
2.3.1. Ag/Si(111)-($\sqrt{3} \times \sqrt{3}$)R30°	26
2.3.2. Ag(111)	27
2.3.3. Au(111)-($22 \times \sqrt{3}$)	28
2.4. References	29

3	Surface-templated assembly of nickel(II) porphine molecules	31
3.1.	Introduction	31
3.2.	Experimental methods	32
3.3.	Results and discussion	33
3.3.1.	NiP on the Ag/Si(111)-($\sqrt{3} \times \sqrt{3}$)R30° surface	33
3.3.2.	NiP on the Ag(111) surface	39
3.4.	Summary	44
3.5.	References	44
4	On-surface synthesis of covalently coupled zinc(II) porphyrins	48
4.1.	Introduction	48
4.2.	Experimental methods	50
4.3.	Results and discussion	50
4.3.1.	Assembly on the Ag(111) surface: metal-directed polymerisation	50
4.3.2.	Thermally assisted assembly: polymerisation through radical addition	59
4.3.3.	Self-assembly on the Au(111)-($22 \times \sqrt{3}$) surface: reconstruction dependant adsorption	63
4.3.4.	Thermally assisted assembly: radical-radical addition	70
4.4.	Summary	71
4.5.	References	72
5	Control of the axial coordination of a surface-confined manganese(III) porphyrin complex	77
5.1.	Introduction	77
5.2.	Experimental methods	79
5.3.	Results and discussion	80
5.3.1.	Molecular organization: self-assembly and registry with the Ag(111) surface	80
5.3.2.	Thermal lability: dissociation of the axial Cl ligand	87

5.3.3.	Axial coordination: the formation of a dioxygen adduct of the MnTPP molecule	95
5.3.4.	Controlling axial coordination: thermal lability and the presence of the axial Cl ligand	108
5.4.	Summary	110
5.5.	References	110
6	Conclusions and future work	118
6.1.	Conclusions	118
6.1.1.	Surface-templated assembly of nickel(II) porphine molecules	118
6.1.2.	On-surface synthesis of covalently coupled zinc(II) porphyrins	119
6.1.3.	Control of the axial coordination of a surface-confined manganese(III) porphyrin complex	120
6.2.	Future work	121
6.2.1.	Selective peripheral substitution of surface-templated metalloporphyrin assemblies	121
6.2.2.	On-surface covalent coupling of metalloporphyrins catalysed by both intrinsic and extrinsic adatoms	122
6.2.3.	Axial coordination of dinitrogen to a surface-confined metalloporphyrin complex	122
6.3.	References	123
	Publications	124
	Appendix A	126

Abstract

This thesis examines the self-assembly of metalloporphyrins on well-defined surfaces. Within this framework, distinct features of surface-confined synthesis are investigated. Characterisation of the surface-confined systems has been performed under ultra-high-vacuum conditions using complementary surface sensitive techniques; namely, scanning tunnelling microscopy, low energy electron diffraction and x-ray photoelectron spectroscopy.

The templated self-assembly of (porphyrinato)nickel(II) (NiP) molecules has been investigated on the Ag/Si(111)-($\sqrt{3} \times \sqrt{3}$)R30° and Ag(111) surfaces. The NiP molecules self-assemble on both the Ag/Si(111)-($\sqrt{3} \times \sqrt{3}$)R30° and Ag(111) surfaces, growing epitaxially in a manner consistent with coincidence on the former, and point-on-line coincidence on the latter. While no transition from the lattice structure of the first layer is found on the Ag/Si(111)-($\sqrt{3} \times \sqrt{3}$)R30° surface, the formation of parallel molecular rows aligned along the primitive lattice vectors of the underlying layer is observed on Ag(111).

On-surface covalent coupling of (5,10,15,20-tetrabromothien-2-ylporphyrinato)-zinc(II) (ZnTBrThP) molecules has been investigated on the Ag(111) and Au(111)-($22 \times \sqrt{3}$) surfaces. When adsorbed on both surfaces, the ZnTBrThP molecules display a latent thermal lability, resulting in the fragmentation of the bromothienyl groups upon annealing. The di- and tetra- (thienyl)porphyrin derivatives are found to predominate on the Ag(111) surface, while the latter is exclusively observed on Au(111)-($22 \times \sqrt{3}$). Subsequent on-surface covalent coupling follows a divergent linkage pattern.

Control of the axial coordination of chloro(5,10,15,20-tetraphenylporphyrinato) manganese(III) (Cl-MnTPP) molecules been investigated on the Ag(111) surface. The thermally induced dissociation of the Cl ligand occurs through a heterolytic cleavage of the metal-ligand bond, without the demetallation of the porphyrin complex. Upon exposure of the MnTPP molecules to molecular oxygen, dioxygen axially coordinates to the central Mn atom in a symmetric egde-on geometry, consistent with a peroxo-like oxidation state. The oxygenation of the MnTPP molecules is reversible, with the molecular monolayer behaving as a so-called oxygen carrier.

Introduction

Developing methods for the synthesis and characterisation of complex supramolecular systems is a key challenge in nanoscience.^{1, 2} Molecular self-assembly demonstrates the emergence of this complexity by the spontaneous association of molecules through noncovalent synthesis. It has long been recognised as one of the few practical synthetic approaches for obtaining true macromolecules.³ Recent investigations reveal that well-defined surfaces, under ultra-high-vacuum conditions, provide versatile platforms for characterising molecular self-assembly in unprecedented detail.⁴

1.1. Concerning porphyrins

1.1.1. Conformational flexibility

Porphyrins are a large family of tetrapyrrole macrocycles.⁵ The parent macrocycle (porphine) is composed of four pyrrole rings linked together via methine bridges, as shown in Figure 1.1(a).⁶ Tetrapyrrole macrocycles are fundamental to a multitude of biological processes, the naturally occurring heme proteins of respiration and chlorophyll pigments of photosynthesis being the archetypal examples.⁵ The structural formulae of heme, also called iron protoporphyrin IX, is noted Figure 1.1(b). The functional versatility of porphyrins is uniquely related to their conformational flexibility.⁷ Though this flexibility allows for nonplanar deformations, the parent macrocycle has an essentially planar conformation, due to its extended π conjugation.⁸ Taken together, these properties make porphyrins particularly well suited to surface-templated assembly. The extended π system of the porphyrin macrocycle tends to lead to flat surface geometries, and in so doing

permits lateral interaction, through which self-organization can occur. The peripheral substitution of the macrocycle allows for the fine tuning of the molecular conformation and, hence, the physicochemical properties of the porphyrin.⁹ Electrophilic aromatic substitution of the peripheral hydrogen atoms may take place at two distinct sites on the macrocycle (Fig. 1.1(a)); the so called meso-carbon and pyrrole- β positions. Conversely, the corresponding metallated (metallo)porphyrin is formed by displacement of the inner pyrrole hydrogens of the porphine core. In this respect, the model substituted porphyrin, 5,10,15,20-tetraphenylporphyrin (TPP) (Fig 1.1(c)), and its homologues, have been the subject of intense research.¹⁰

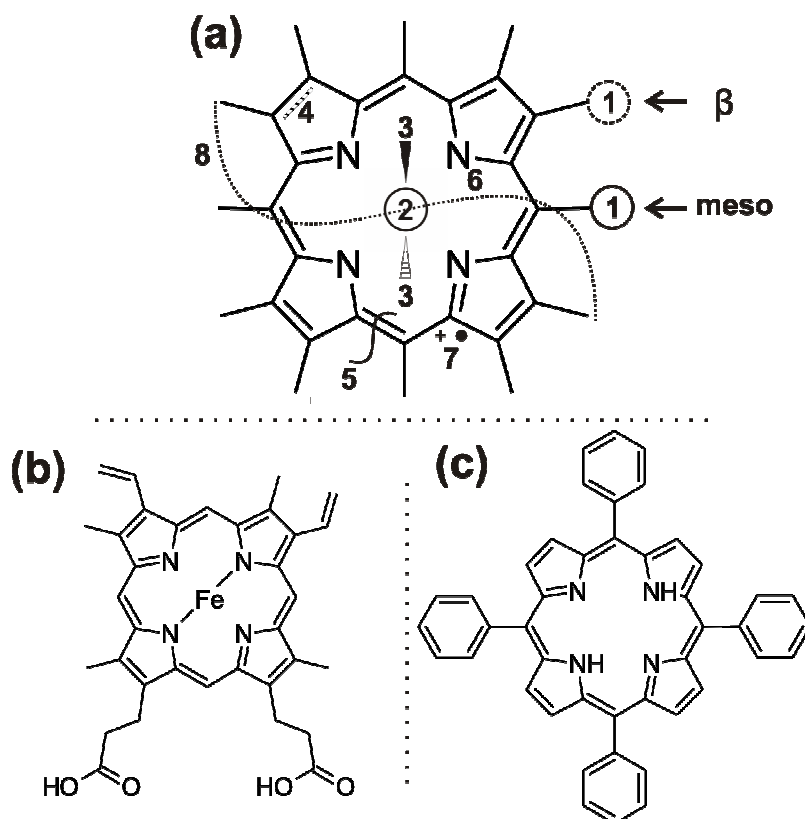


Figure 1.1. (a) Illustration of several possibilities for chemically modifying the core porphine macrocycle: 1) peripheral substitution; 2) metalation; 3) axial ligation; 4) ring reduction; 5) alteration of the conjugated system; 6) N-substitution; 7) cation radical formation; 8) “strapping” of the macrocycle via linkage of meso-carbon and pyrrole- β positions; after reference 7. (b) and (c) structural formulae of heme (iron protoporphyrin IX) and tetraphenylporphyrin, respectively.

1.1.2. Biomimetic catalysis

Many metalloporphyrin complexes are able to react directly with molecular oxygen, in its triplet ground state, to form dioxygen adducts that can participate in the oxygenation of singlet organic molecules.¹¹ In enzymatic oxygenase reactions, such metalloporphyrins commonly take the form of the active cofactor. Heme-containing oxygenases are among the most important enzymes found in nature.¹² As structural analogues of heme, and potential oxygenase models, synthetic metalloporphyrins have received much attention.^{12, 13}

Cytochrome P450 is a widely distributed heme-containing oxygenase, which catalyzes the incorporation of oxygen from molecular oxygen into organic substrates.¹¹ In modelling cytochrome P450, the reductive activation step of the natural catalytic cycle can be replaced by an oxo compound with a partially reduced oxygen atom. Through this so-called peroxide shunt, the metalloporphyrin chloro(5,10,15,20-tetraphenylporphyrinato)iron(III) was shown to catalyze the hydroxylation and epoxidation of hydrocarbons using iodosobenzene as an oxidant (Appendix A, Figure 1).¹⁴ Modelling the natural catalytic cycle, where the reductive activation of molecular oxygen is followed, requires the use of a suitable co-reductant. By this means, chloro(5,10,15,20-tetramesitylporphyrinato)manganese(III) was found to catalyze the epoxidation of alkenes using molecular oxygen as an oxidant and sodium borohydride as a co-reductant (Appendix A, Figure 2).¹⁵ In a similar way, various substituted metallo-TPP complexes, notably of chloro-iron,¹⁶ chromium,¹⁷ ruthenium,¹⁸ and manganese,¹⁹ have been shown to be efficient oxygen transfer catalysts.

In the cytochrome P450 system, access of the substrate to the active heme-iron centre is controlled by the surrounding (apo)protein environment.⁷ The metalloporphyrin analogues have evolved following a similar synthetic approach from simple sterically hindered models, to more elaborate mono- and bis-faced protected porphyrins;²⁰ an illustrative example of the latter type is the so called picnic basket porphyrin (Appendix A, Figure 3)²¹. Further developments have also focused on combining the interplay of axial ligation and self-assembly in the synthesis of supramolecular systems which demonstrate shape-selective oxygenation reactions. Recently, a manganese(III) porphyrin catalyst self-assembled at the interface of a Au(111) surface and n-tetradecane liquid phase was reported

to catalyze the epoxidation of alkenes using molecular oxygen as an oxidant; significantly, reductive activation of the catalyst is brought about by coordination of the metal surface.²² A noteworthy feature of this model system is the higher selectivity demonstrated for cis-alkenes compared to the corresponding trans-isomers, despite the essentially flat porphyrin periphery.

1.1.3. On-surface synthesis

Surface confinement is a promising synthetic strategy to obtain macromolecules and molecular assemblies of targeted dimensionality.²³ The on-surface synthesis of porphyrin ensembles holds particular interest not only for their biological relevance, but also for their chemical versatility. Peripheral substitution of the porphine macrocycle gives synthetic access to ensembles whose dimensionality depends on the geometric and chemical nature of the substituents that mediate their assembly. In this way, a multitude of functional groups can potentially direct assembly through noncovalent and covalent synthesis. Furthermore, the typically low vapour pressure of crystalline porphyrins (at room temperature)²⁴ enables sublimation under ultra-high-vacuum (UHV) conditions, making possible characterisation by a range of surface-sensitive techniques.

Synthesis through noncovalent molecular self-assembly relies on the association of molecules by many weak, reversible interactions.³ Shape-dependent self-assembly of porphyrin molecules arising from weak multipoint van der Waals (vdW) interactions can be made more directional by the selective incorporation of stronger hydrogen-bonding and electrostatic interactions. This synthetic approach has been effectively demonstrated for the self-assembly of 5,10,15,20-tetrakis-(3,5-di-tertiarybutylphenyl)porphyrin (H₂-TBPP) molecules on the Au(111) surface (Appendix A, Figure 4).²⁵⁻²⁸ The “unfunctionalised” H₂-TBPP molecules exhibit a close-packed arrangement on the Au(111) surface, arising from vdW interactions between adjacent di-tertiarybutylphenyl (tBP) groups. To induce directed assembly, one or more of the four bulky tBP substituents is replaced (*de novo*) by a functional group mediating stronger intermolecular interaction. The first such report made use of cyanophenyl groups to mediate stronger electrostatic dipole-dipole interactions.²⁵ Replacing one of the tBP meso-substituents with a cyanophenyl group was found to result

in the assembly of well defined trimeric aggregates. Further replacement in a cis-configuration leads to tetrameric aggregates, while trans-substitution gives rise to linearly self-assembled nanolines. In a similar manner, subsequent studies have employed carboxylphenyl groups, bearing a fundamental hydrogen bonding system, to control molecular self-assembly.²⁷ Significantly, the resulting dimensionality of these supramolecular systems directly reflects the substitution pattern of the interacting groups.

Beyond supramolecular self-assembly lies the synthesis of macromolecules by irreversible covalent coupling. Radical addition is a simple reaction type that has been successfully applied in the synthesis of covalently coupled porphyrin aggregates.²⁹⁻³² In general, the reaction pathway involves an activation process, in which the positions of the covalent-interlinks are predetermined by the substitution pattern of labile functional groups. The seminal study of on-surface covalent coupling through radical addition featured 5,10,15,20-tetrakis(4-bromophenyl)porphyrin (Br₄TPP) molecules, which bear thermally labile halophenyl groups (Appendix A, Figure 5).²⁹ At room-temperature, the Br₄TPP molecules self-assemble (on the Au(111) surface) forming a well defined square lattice structure. By thermally inducing the dissociation of labile bromine moieties, either on-surface or at sublimation, the resulting porphyrin species are brought to couple through addition reactions. Control of the dimensionality of the coupled structures was demonstrated by incorporating one, two or four terminal Br moieties into the TPP precursor; following the same protocol, molecular dimers, nanolines and networks, respectively, were formed. This synthetic approach was recently elaborated on by partitioning the reaction pathway into discrete coupling steps, involving different halophenyl substituents which exhibit distinct bond dissociation energies.³⁰

1.2. Thesis outline

In this thesis the self-assembly of metalloporphyrins on well-defined surfaces is examined. Within this framework, distinct features of surface-confined synthesis are investigated; namely, templated self-assembly, covalent coupling and axial coordination chemistry.

Characterisation of the surface-confined systems has been performed under UHV conditions, using complementary surface sensitive methods.

The thesis continues in Chapter 2 with a description of the experimental methods and set-up. The basic principle and theory of operation of the surface sensitive methods used in this work are presented; specifically, those of scanning tunnelling microscopy, low energy electron diffraction and x-ray photoelectron spectroscopy. An illustration then follows of the UHV system within which the experimental work has been carried out. A brief description of the different substrate surfaces used as the template environments for molecular assembly is then given.

The surface-templated assembly of unsubstituted metalloporphyrins offers a potential route toward controlled porphyrin functionalisation. In Chapter 3, the templated self-assembly of (porphyrinato)nickel(II) molecules (Fig. 1.2(a)) on both the Ag(111) and Ag/Si(111)-($\sqrt{3} \times \sqrt{3}$)R30° surfaces is investigated. The findings offer a valuable insight into the epitaxial nature of peripherally unsubstituted porphyrins on well defined surfaces. Notably, a substrate specific control of the supramolecular assembly, expressed by parallel molecular rows which are separated by uniform “missing row” structures, is reported.

The functionalisation of metalloporphyrins by labile multitopic ligands provides both selectivity and directionality in on-surface synthesis. Chapter 4 investigates the covalent coupling of [5,10,15,20-(tetra-5-bromothien-2-yl)porphyrinato]zinc(II) molecules (Fig. 1.2(b)) on both the Ag(111) and Au(111)-($22 \times \sqrt{3}$) surfaces. The results of this work yield a fundamental understanding of (substrate-directed) metalloporphyrin assembly mediated by (hemilabile) bromothienyl substituents. The structural motifs of the thermally-assisted coupling are presented.

Surface-confinement is a promising strategy to control the diverse axial coordination properties of metalloporphyrins. In Chapter 5, the axial lability of chloro(5,10,15,20-tetraphenylporphyrinato)manganese(III) molecules (Fig. 1.2(c)) on the Ag(111) surface is investigated. The findings provide a valuable insight into the latent coordination properties of surface-confined metalloporphyrins. The manganese porphyrin complex is demonstrated to have latent unoccupied coordination site, arising from the thermal lability of the axial chloride ligand. Significantly, the formation of a dioxygen adduct upon exposure to molecular oxygen is reported.

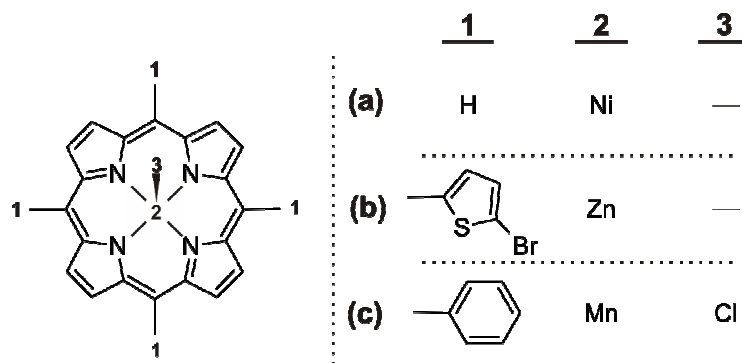


Figure 1.2. Structural formulae of the metalloporphyrin complexes studied in this thesis; (a) (porphyrinato)nickel(II), (b) [5,10,15,20-(tetra-5-bromothiien-2-yl)porphyrinato]zinc(II), (c) chloro(5,10,15,20-tetraphenylporphyrinato)manganese(III); explicit hydrogens omitted for clarity.

Finally Chapter 6 presents the conclusions of the thesis, and outlines the possible direction of future work. The chapters of the thesis have been written in such a way that they are largely self-contained. With the exception of the experimental methods sections, it is possible read individual chapters without the need to access others.

1.3. References

- (1) Feynman, R. P. There's plenty of room at the bottom. *Eng. Sci.* **1960**, 23, 22-36.
- (2) Barth, J. V.; Costantini, G.; Kern, K. Engineering atomic and molecular nanostructures at surfaces. *Nature* **2005**, 437.
- (3) Whitesides, G. M.; Mathias, J. P.; Seto, C. T. Molecular self-assembly and nanochemistry - A chemical strategy for the synthesis of nanostructures. *Science* **1991**, 254.
- (4) Barth, J. V. Molecular architectonic on metal surfaces. *Annu. Rev. Phys. Chem.* **2007**, 58, 375-407.
- (5) Milgrom, L. R. (1997) *The colours of life: an introduction to the chemistry of porphyrins and related compounds*. Oxford: Oxford University Press.

- (6) Merritt, J. E.; Loening, K. L. Nomenclature of tetrapyrroles. *Pure & Appl. Chem.* **1978**, *51*, 2251-2304.
- (7) Senge, M. O. Exercises in molecular gymnastics - bending, stretching and twisting porphyrins. *Chem. Commun.* **2006**, 243-256.
- (8) Rosa, A.; Ricciardi, G.; Baerends, E. J. Synergism of porphyrin-core saddling and twisting of meso-aryl substituents. *J. Phys. Chem. A* **2006**, *110*, 5180-5190.
- (9) Roeder, B.; Buechner, M.; Rueckmann, I.; Senge, M. O. Correlation of photophysical parameters with macrocycle distortion in porphyrins with graded degree of saddle distortion. *Photochem. Photobiol. Sci.* **2010**, *9*, 1152-1158.
- (10) Senge, M. O. Stirring the porphyrin alphabet soup - functionalization reactions for porphyrins. *Chem. Commun.* **2011**, *47*, 1943-1960.
- (11) Sono, M.; Roach, M. P.; Coulter, E. D.; Dawson, J. H. Heme-containing oxygenases. *Chem. Rev.* **1996**, *96*, 2841-2887.
- (12) Meunier, B. Metalloporphyrins as versatile catalysts for oxidation reactions and oxidative DNA cleavage. *Chem. Rev.* **1992**, *92*, 1411-1456.
- (13) Feiters, M. C.; Rowan, A. E.; Nolte, R. J. M. From simple to supramolecular cytochrome P450 mimics. *Chem. Soc. Rev.* **2000**, *29*, 375-384.
- (14) Groves, J. T.; Nemo, T. E.; Myers, R. S. Hydroxylation and epoxidation catalyzed by iron-porphine complexes - oxygen-transfer from iodosylbenzene. *J. Am. Chem. Soc.* **1979**, *101*, 1032-1033.
- (15) Tabushi, I.; Koga, N. P-450 Type oxygen activation by porphyrin-manganese complex. *J. Am. Chem. Soc.* **1979**, *101*, 6456-6458.
- (16) Groves, J. T.; Nemo, T. E. Epoxidation reactions catalyzed by iron porphyrins - oxygen-transfer from iodosylbenzene. *J. Am. Chem. Soc.* **1983**, *105*, 5786-5791.
- (17) Groves, J. T.; Kruper, W. J. Preparation and characterization of an oxoporphinatochromium(V) complex. *J. Am. Chem. Soc.* **1979**, *101*, 7613-7615.
- (18) Groves, J. T.; Quinn, R. Aerobic epoxidation of olefins with ruthenium porphyrin catalysts. *J. Am. Chem. Soc.* **1985**, *107*, 5790-5792.
- (19) Groves, J. T.; Kruper, W. J.; Haushalter, R. C. Hydrocarbon oxidations with oxometalloporphyrins - isolation and reactions of a (porphinato)manganese(V) complex. *J. Am. Chem. Soc.* **1980**, *102*, 6375-6377.

- (20) Rose, E.; Andrioletti, B.; Zrig, S.; Quelquejeu-Ehteve, M. Enantioselective epoxidation of olefins with chiral metalloporphyrin catalysts. *Chem. Soc. Rev.* **2005**, *34*, 573-583.
- (21) Collman, J. P.; Zhang, X. M.; Hembre, R. T.; Brauman, J. I. Shape-selective olefin epoxidation catalyzed by manganese picnic basket porphyrins. *J. Am. Chem. Soc.* **1990**, *112*, 5356-5357.
- (22) Hulsken, B.; Van Hameren, R.; Gerritsen, J. W.; Khoury, T.; Thordarson, P.; Crossley, M. J.; Rowan, A. E.; Nolte, R. J. M.; Elemans, J. A. A. W.; Speller, S. Real-time single-molecule imaging of oxidation catalysis at a liquid-solid interface. *Nat. Nanotechnol.* **2007**, *2*, 285-289.
- (23) Lackinger, M.; Heckl, W. M. A STM perspective on covalent intermolecular coupling reactions on surfaces. *J. Phys. D: Appl. Phys.* **2011**, *44*, 464011.
- (24) Perlovich, G. L.; Golubchikov, O. A.; Klueva, M. E. Thermodynamics of porphyrin sublimation. *J. Porphyrins Phthalocyanines* **2000**, *4*, 699-706.
- (25) Yokoyama, T.; Yokoyama, S.; Kamikado, T.; Okuno, Y.; Mashiko, S. Selective assembly on a surface of supramolecular aggregates with controlled size and shape. *Nature* **2001**, *413*.
- (26) Fendt, L.; Stoehr, M.; Wintjes, N.; Enache, M.; Jung, T. A.; Diederich, F. Modification of supramolecular binding motifs induced by substrate registry: formation of self-assembled macrocycles and chain-like patterns. *Chem. Eur. J.* **2009**, *15*, 11139-11150.
- (27) Yokoyama, T.; Kamikado, T.; Yokoyama, S.; Mashiko, S. Conformation selective assembly of carboxyphenyl substituted porphyrins on Au (111). *J. Chem. Phys.* **2004**, *121*, 11993-11997.
- (28) Nishiyama, F.; Yokoyama, T.; Kamikado, T.; Yokoyama, S.; Mashiko, S. Layer-by-layer growth of porphyrin supramolecular thin films. *Appl. Phys. Lett.* **2006**, *88*, 253113.
- (29) Grill, L.; Dyer, M.; Lafferentz, L.; Persson, M.; Peters, M. V.; Hecht, S. Nano-architectures by covalent assembly of molecular building blocks. *Nat. Nanotechnol.* **2007**, *2*, 687-691.
- (30) Lafferentz, L.; Eberhardt, V.; Dri, C.; Africh, C.; Comelli, G.; Esch, F.; Hecht, S.; Grill, L. Controlling on-surface polymerization by hierarchical and substrate-directed growth. *Nature Chem.* **2012**, *4*, 215-220.

(31) In't Veld, M.; Iavicoli, P.; Haq, S.; Amabilino, D. B.; Raval, R. Unique intermolecular reaction of simple porphyrins at a metal surface gives covalent nanostructures. *Chem. Commun.* **2008**, 153-1538.

(32) Haq, S.; Hanke, F.; Dyer, M. S.; Persson, M.; Iavicoli, P.; Amabilino, D. B.; Raval, R. Clean coupling of unfunctionalized porphyrins at surfaces to give highly oriented organometallic oligomers. *J. Am. Chem. Soc.* **2011**, *133*, 12031-12039.

Experimental Methods

2.1. Surface sensitive techniques

2.1.1. Scanning tunnelling microscopy

When two metallic electrodes are brought to within a fraction of a nanometre of each other, a so-called tunnelling conductance is generated.¹ The application of voltage difference between these electrodes generates a small but detectable “tunnelling current”. The tunnelling electrons move from one electrode to the other, penetrating the barrier between them. This purely quantum mechanical effect, arising from the wave nature of the electron, is at the core of scanning tunnelling microscopy (STM).

A theoretical description of electron tunnelling may be given within the framework of a one-dimensional rectangular barrier, as depicted by the metal-vacuum-metal junction in Figure 2.1. In quantum mechanics, an electron in a potential $U(z)$ is described by a wavefunction $\varphi(z)$, which satisfies the Schrödinger equation

$$-\frac{\hbar}{2m} \frac{d^2}{dz^2} \varphi(z) + U(z)\varphi(z) = E\varphi(z) \quad (2.1)$$

For the given example (Fig. 2.1), $E > U$ for regions outside the vacuum barrier, and $E < U$ within the barrier. In the regions where $E > U$, equation (2.1) has oscillatory solutions of the form $\varphi(z) = \varphi(0)e^{\pm ikz}$, where $k = \sqrt{2m(E - U)}/\hbar$ is the electron wave vector. The electron moves in the positive or negative z direction with a momentum $p = \hbar k$, as is classically found. However, within the barrier region where $U > E$, equation (2.1) has a decaying solution of the form $\varphi(z) = \varphi(0)e^{-\kappa z}$, where $\kappa = \sqrt{2m(U - E)}/\hbar$ is the decay

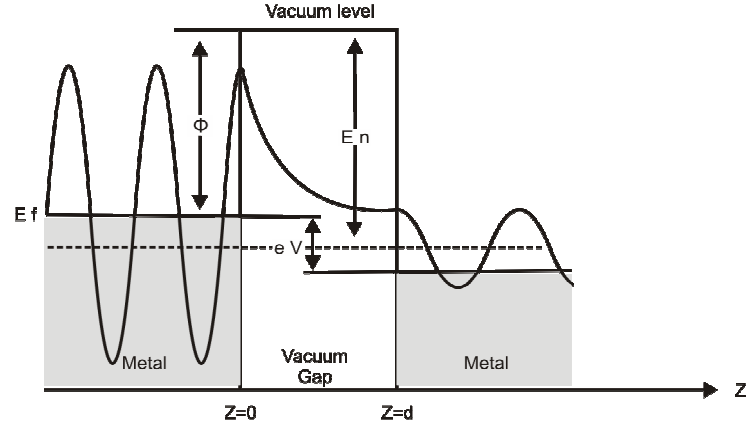


Figure 2.1. Diagram of a one dimensional metal-vacuum-metal tunnel junction, under an applied bias-voltage eV . The work functions ϕ of metals left and right of the vacuum gap are equal.

constant. This implies that the electron penetrates through the barrier in the positive z direction; a result that is classically forbidden. The probability density of observing an electron near the point $z = d$ (Fig. 2.1) is given by

$$|\varphi(d)|^2 = |\varphi(0)|^2 e^{-2\kappa d}. \quad (2.2)$$

It follows, therefore, that the electron has a non-zero probability of penetrating the barrier.¹

In the simplest case $U(z)$ represents the vacuum level, so for electron states at the Fermi level (E_f), $U - E$ corresponds to the work function ϕ of the metal. For a positive bias-voltage V much smaller than the work function (i.e. $eV \ll \phi$) only states φ_n with energy levels E_n between $E_f - eV$ and E_f can participate in tunnelling; here, the work functions of both metals are taken to be equal. The tunnelling current I_t , therefore, being proportional to the probability of electrons penetrating the barrier (equation (2.2)), is found by summing over all possible states E_n in the energy range $E_f - eV < E < E_f$,

$$I_t(V) \propto \sum_{E_n = E - eV}^E |\varphi_n(0)|^2 e^{-2\kappa z}, \quad (2.3)$$

where

$$\kappa = \frac{\sqrt{2m\phi}}{\hbar} \quad (2.4)$$

is the decay constant of electron states at the Fermi level.

Using units of eV and nm^{-1} , for ϕ and κ , respectively, the numerical value of Eqn. (2.4) is,¹

$$\kappa = 5.1\sqrt{\phi(eV)}nm^{-1} \quad (2.5)$$

For a typical work function of 5 eV, equation (2.5) yields a decay constant of 0.11 nm^{-1} . Taking as an example the typical height of a monoatomic surface step (~ 0.25 nm) for the barrier width, the tunnelling current (by equation (2.3)) will be altered by almost three orders of magnitude. This strong dependence of the tunnelling current on the barrier width is the origin of the unprecedented vertical resolution of STM.

By resolving the local electronic structure on an atomic scale, STM allows the local atomic structure to be revealed. Notably, it was with the invention of the STM,² that the first real-space determination of the Si(111) (7×7) surface reconstruction was obtained³. The principle of STM is rather straightforward. An atomically sharp metal tip (one electrode of a tunnel junction) is brought near enough a conducting surface (second electrode) that a finite vacuum tunnelling conductance is measured. Upon the application of a bias-voltage a net tunnelling current is generated. The position of the tip in three dimensions is controlled by means of piezoelectric drivers. The tip scans the surface in two dimensions, while its height is adjusted to keep the tunnelling current constant. In this way, a constant current contour of the surface is obtained.

2.1.2. Low energy electron diffraction

Due to their small mean free path lengths in solids, low energy electrons between 10–200eV are highly surface sensitive.⁴ In this energy range, electrons have deBroglie wavelengths on the order of an angstrom, slightly smaller than a typical interatomic

spacing. Incident on crystalline surfaces, an electron beam of such low energy electrons can generate a backscattered diffraction pattern, revealing information about the long and short range surface order.⁵ Surface structure determination by this means is referred to as low energy electron diffraction (LEED).

A diffracted beam of electrons will emerge from a crystalline surface whenever constructive interference occurs between successive planes of atoms, as illustrated in Figure 2.2(a). In the simple case of a square lattice, this is more generally stated by the Bragg condition for diffraction,

$$a \sin \theta = (h^2 + k^2)^{1/2} \lambda \quad (2.6)$$

where $(h^2 + k^2)^{1/2}$ is the order of diffraction. As the wavelength λ (of an electron) in the LEED energy range is of same order of magnitude as a typical lattice constant a , diffraction maxima of elastically scattered electrons display significant angular separation θ , and are thus easily resolved.

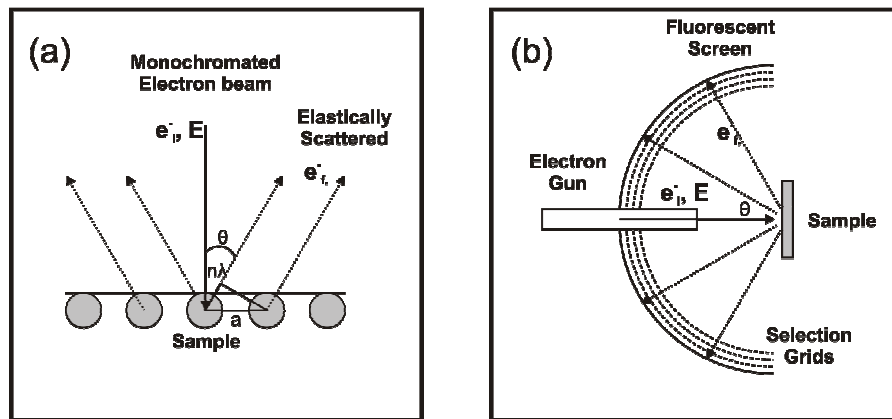


Figure 2.2. (a) Representation of diffraction from a two dimensional lattice, shown along a single azimuth. (b) Diagram of a typical LEED analyser; after reference 8.

In backscattering elastically from a crystalline surface, an incident electron undergoes a change in wavevector k not wavelength λ ; that is, only its direction changes. For this reason, LEED patterns provide surface geometry in so-called reciprocal space,

which bears an inverse relationship to the “real-space” surface lattice. The principle of LEED is well described by a typical experiment, as depicted in Figure 2.2(b). Here, a monochromatic beam of electrons, with variable energy E , is directed at normal incidence to a sample surface. Backscattered electrons pass through a set of hemispherical retarding grids, which serve to filter out the inelastic background, while the remaining elastically scattered electrons are accelerated towards a fluorescent screen. In this manner, the angular distribution of the diffracted electron beam is obtained, revealing the symmetry of the surface atomic arrangement.

2.1.3. X-ray photoelectron spectroscopy

The technique of photoelectron spectroscopy is illustrated in Figure 2.3. When a photon of energy $h\nu$ impinges on a solid, the photoexcitation of electrons may occur. If the kinetic energy of the photoexcited electron is larger than the work function ϕ of the solid surface, it may be emitted into the vacuum. Measured relative to the vacuum level of the solid, the resulting kinetic energy E_k of the photoelectron is given by

$$E_k = h\nu - \phi - E_B \quad (2.7)$$

where E_B is the electron binding energy.^{6, 7} The precise binding energy of electron core-levels of an atom or molecule is uniquely defined by its chemical environment.^{6, 7} Equation (2.7) shows that for a fixed photon energy, the binding energy E_B can be determined from the distribution of the photoelectrons emitted to vacuum.

In x-ray photoelectron spectroscopy (XPS), a monoenergetic beam of x-rays (for Al $K\alpha$, $h\nu = 1486.6\text{eV}$) is used as the excitation energy for photoemission. While x-rays have large penetration depths in solids, the mean free path length of electrons is small. Consequently, only photoelectrons near the surface of a solid are emitted to vacuum without energy loss. This principle makes XPS a versatile technique for the chemical analysis of surfaces.

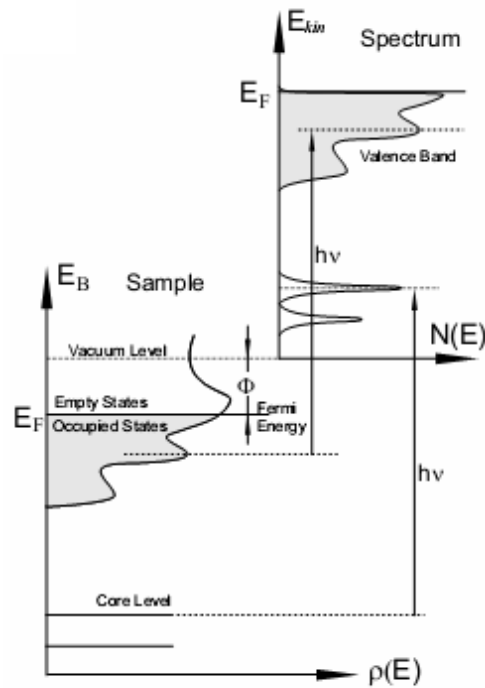


Figure 2.3. Energy diagram illustrating photoexcitation with monoenergetic photons; after ref. 8.

Experimentally, the energy distribution of the photoelectrons is measured with electrostatic energy analyzers. In a hemispherical analyser, collected electrons travel between two charged metal hemispheres that allow only those of a particular kinetic energy to pass. It is customary to hold this “pass energy” constant, and retard or accelerate the electrons before they enter the analyser. Counting of the transmitted electrons is achieved by secondary electron amplifiers, so-called Channeltron detectors. In this fashion, an energy distribution spectrum is obtained by varying the energy of the electron beam to the pass energy of the analyser.

2.2. Ultra-high-vacuum system

All experiments performed under ultra-high-vacuum (UHV) conditions were carried out using a commercially available Omicron (GmbH) UHV system. The installation consists of three chambers; one for sample introduction (a fast entry lock chamber), and two others for

sample preparation and sample analysis, respectively. Connecting chambers are separated by manually operated gate valves. Sample transfer between chambers is accomplished by magnetically coupled linear drives. A diagram of the chamber and sample-transfer system is presented in Figure 2.4.

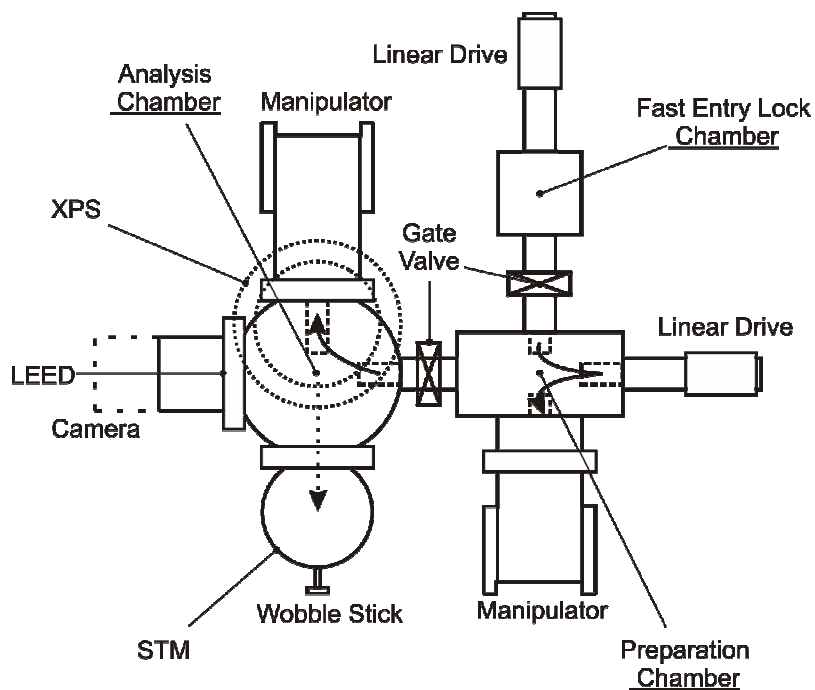


Figure 2.4. Diagram of the chamber and sample-transfer system from a top-down perspective.

UHV is achieved by a system of (Varian) ion getter pumps used in tandem with titanium sublimation pumps (TSP). A turbo-molecular pump (TP) backed by a two-stage rotary vane pump (RP) is used in pumping down from atmosphere, or in the instance of high loads (e.g. sputtering). A schematic of the pumping system is shown in Figure 2.5. Pirani and ionization gauges are used to measure pressures in the medium to ultra-high vacuum regimes, respectively. Typical base pressure in the preparation and analysis chambers (during experiments) is better than 1×10^{-10} mbar.

Samples and STM tips can be introduced to the preparation chamber, without breaking UHV conditions, by means of the fast entry load-lock chamber. The preparation chamber is equipped with an Omicron ISE 5 sputter ion source for sample surface cleaning, accompanied by a heating stage which allows for both direct current and indirect resistive

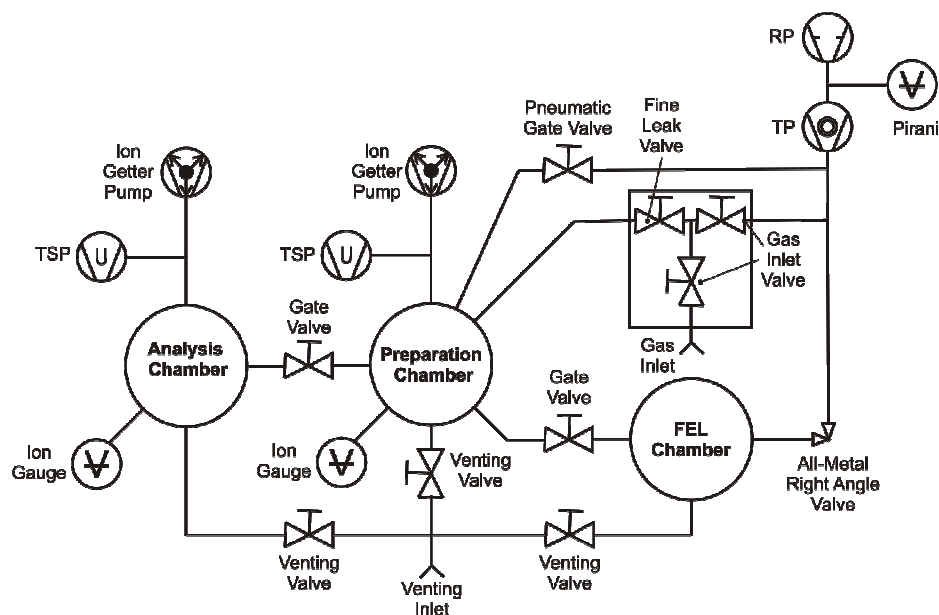


Figure 2.5. Schematic of the vacuum chamber pumping system.

heating of samples. In addition, the chamber holds a series of evaporator ports and precision leak valves for molecule deposition and gas dosing.

The analysis chamber houses an Omicron (VT-STM) scanning tunnelling microscope, a (Spectraled) low energy electron diffraction system and an (ESCA+) x-ray photoelectron spectrometer; the latter consisting of an EA 125 hemispherical energy analyzer and DAR 400 x-ray source. A pincer-wobble stick is used to transfer samples from the main chamber manipulator to the sample stage of the STM. LEED and XPS experiments are carried out on the main chamber manipulator.

2.3. Substrates

2.3.1. Ag/Si(111)-($\sqrt{3} \times \sqrt{3}$)R30°

Silver deposited on the Si(111)-(7 × 7) surface forms a ($\sqrt{3} \times \sqrt{3}$)R30° reconstruction upon thermal annealing.⁹ The resulting Ag/Si(111)-($\sqrt{3} \times \sqrt{3}$)R30° surface is well described by the so-called honeycomb-chain-trimer (HCT) model.¹⁰ Here, the Ag adatoms are proposed

to form “chained” trimers around the underlying Si trimers of the second layer, as illustrated in Figure 2.6(a). The Ag/Si(111)-($\sqrt{3} \times \sqrt{3}$)R30° lattice is described by a hexagonal unit cell with a lattice constant of $\sim 6.8 \text{ \AA}$; the intratrimer Ag-Ag distance is $\sim 5.1 \text{ \AA}$. An occupied state STM image of the Ag/Si(111)- ($\sqrt{3} \times \sqrt{3}$)R30° surface obtained at monolayer coverage is shown in Figure 2.6(b). In the context of the HCT model, each honeycomb protrusion corresponds to an Ag trimer, whereby the interstitial depressions coincide with the position of an underlying Si-trimer.

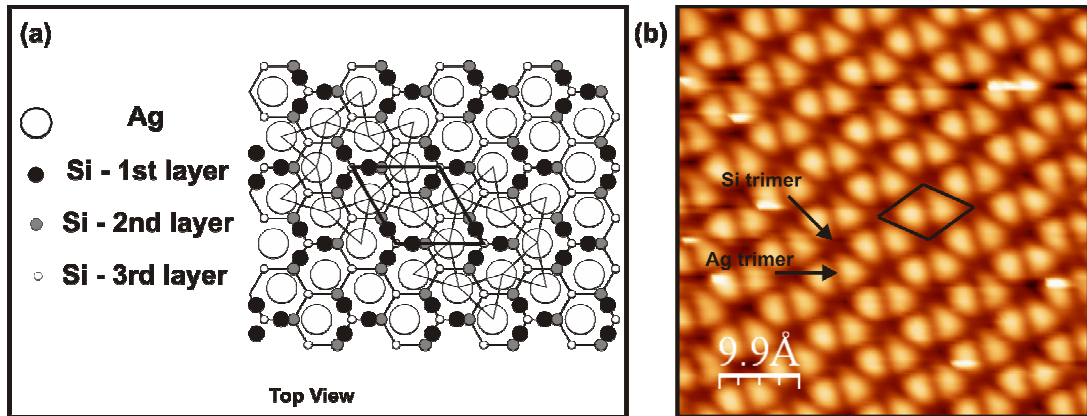


Figure 2.6. The Ag/Si(111)- ($\sqrt{3} \times \sqrt{3}$)R30° surface. (a) Diagram of the HCT model. (b) High resolution occupied state STM image; $V_{\text{sample}} = -0.54 \text{ V}$, $I_t = 1.0 \text{ nA}$, size $5 \text{ nm} \times 5 \text{ nm}$.

2.3.2. Ag(111)

Monocrystalline silver has a face centred cubic (fcc) lattice structure. The formation of the Ag(111) surface, as illustrated in Figure 2.7(a), follows from the closed-packed fcc stacking of the bulk. The Ag(111) surface lattice is described by a hexagonal unit cell, with a lattice constant of 2.88 \AA .¹¹ Figure 2.7(b) shows an occupied state STM image of the clean Ag(111) surface. Obtained with atomic resolution, the image reveals surface protrusions which reflect the individual Ag atoms.

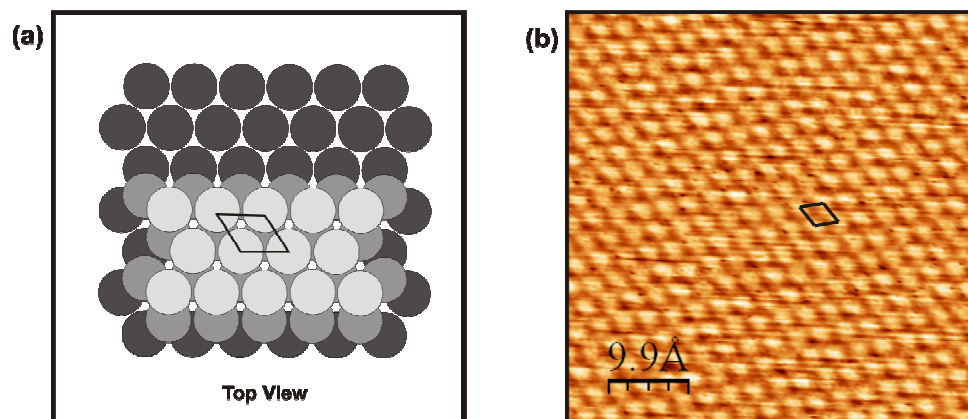


Figure 2.7. The Ag(111) surface. (a) Sketch of the fcc(111) stacking. (b) High resolution unoccupied state STM image; $V_{\text{sample}} = 0.30 \text{ V}$, $I_t = 1.0 \text{ nA}$, size $5 \text{ nm} \times 5 \text{ nm}$.

2.2.3. Au(111)- $(22 \times \sqrt{3})$

Though monocrystalline gold has an fcc lattice structure, the close-packed (111) surface exhibits a $(22 \times \sqrt{3})$ reconstruction.¹² The structure of the Au(111)- $(22 \times \sqrt{3})$ surface is characterised by a contraction and lateral displacement of the topmost Au atoms along and normal to the closed-packed directions, respectively. An illustration of the reconstruction is given in Figure 2.8(a). The nearly uniform (4.55 %) contraction of the Au surface atoms leads to a rectangular unit cell, with side lengths of 63 and 4.7 \AA - given by the $(22 \times \sqrt{3})$ arrangement of the topmost and bulk-like second layer. Arising from the lateral oscillatory displacement ($\sim 0.9 \text{ \AA}$), a periodic transition from fcc to hcp stacking of the topmost Au atoms occurs.¹³ Figure 2.8(b) shows an exemplary occupied state STM image of the clean Au(111)- $(22 \times \sqrt{3})$ surface. The reconstruction pattern is marked by a pair-wise arrangement of parallel lines, which lie perpendicular to the closed-packed contraction directions. A distinct ($\sim 0.2 \text{ \AA}$) vertical corrugation marks the transition region between fcc and hcp stacking regions, the former of which appear markedly wider. The overall tendency for an isotropic surface contraction is revealed by a periodic bending of the parallel corrugation lines by 120° , resulting in the so-called herringbone reconstruction pattern.

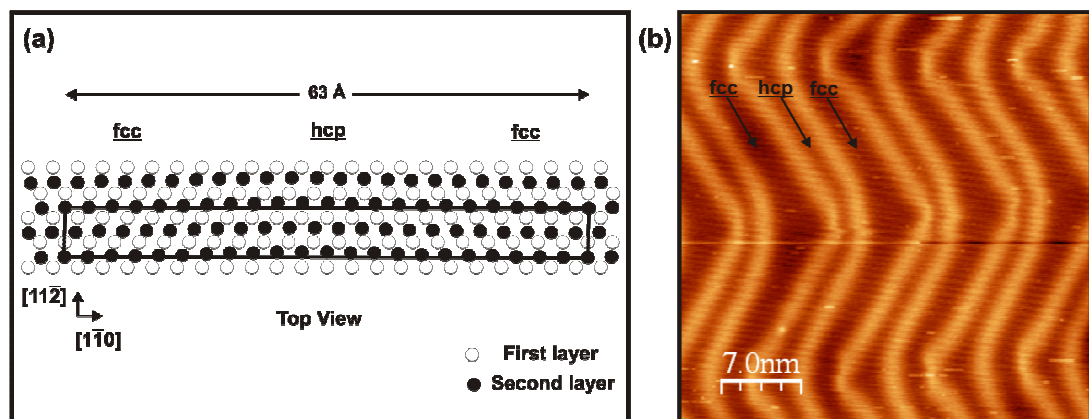


Figure 2.8. The Au(111)-(22 × √3) surface. (a) Schematic of the (22 × √3) reconstruction. (b) Large scale occupied state STM image; $V_{\text{sample}} = -1.25$ V, $I_t = 0.20$ nA, size 35 nm × 35 nm.

2.4. References

- (1) Chen, C. Julian. (1993) *Introduction to scanning tunneling microscopy*, Vol. 227. New York: Oxford University Press.
- (2) Binnig, G.; Rohrer, H. Scanning tunnelling microscopy. *Surf. Sci.* **1983**, 126, 236-244.
- (3) Binnig, G.; Rohrer, H.; Gerber Ch.; Weibel E. 7 x 7 Reconstruction on Si(111) resolved in real space. *Phys. Rev. Lett.* **1982**, 50, 2, 120.
- (4) Seah, M.P.; Dench, W.A. Quantitative electron spectroscopy of surfaces: a standard data base for electron inelastic mean free paths in solids. *Surf. Interface Analy.* **1979**, 1: 2–11.
- (5) Gilmore, I. S; Vickerman, J. C. (Ed.). (1997) *Surface analysis: the principal techniques..* Chichester/New York: John Wiley.
- (6) Cardona, M.; Ley, L. (1978) *Photoemission in solids, Vol. 1: general principles (topics in applied physics, Vol. 26)*. Springer-Verlag.
- (7) Feuerbacher, B.; Fitton, B; Willis, R.F. (Eds.) (1978) *Photoemission and the electronic properties of surface*. New York: Wiley.
- (8) Varykhalov, A. *Quantum-size effects in the electronic structure of novel self-organized systems with reduced dimensionality*. Diss. Universitätsbibliothek, **2005**.

- (9) Wilson, R. J.; Chiang, S. Registration and nucleation of the Ag/Si(111) ($\sqrt{3} \times \sqrt{3}$)R30° structure by scanning tunneling microscopy. *Phys. Rev. Lett.* **1987**, *59*, 20, 2329.
- (10) Takahashi, T.; Shinichiro, N.; Naoko Okamoto Study on the Si(111) $\sqrt{3} \times \sqrt{3}$ -Ag surface structure by x-ray diffraction. *Jpn. J. Appl. Phys.* **1988** *5*, 753-755.
- (11) Orisaka, S.; Minobe, T.; Uchihashi, T.; Sugawara, Y.; Morita, S. The atomic resolution imaging of metallic Ag(111) surface by noncontact atomic force microscope. *Appl. Surf. Sci.* **1999**, *140*, 243-246.
- (12) Barth, J. V.; Brune, H.; Ertl, G.; Behm, R. J. Scanning tunneling microscopy observations on the reconstructed Au(111) Surface - atomic-structure, long-range superstructure, rotational domains, and surface-defects. *Phys. Rev. B* **1990**, *42*, 9307-9318.
- (13) Wang, Y.; Hush, N. S.; Reimers, J. R. Simulation of the Au(111)-(22 × $\sqrt{3}$) surface reconstruction. *Phys. Rev. B* **2007**, *75*, 233416.

Surface-templated assembly of nickel(II) porphine molecules

3.1. Introduction

As the parent compound of the porphyrin family, porphine holds particular interest for its structural simplicity. By virtue of its open β -pyrrole and meso-carbon sites, porphine represents a versatile precursor in the synthesis of more complex porphyrin derivatives.¹ This versatility arises from the intrinsic reactivity of the porphine macrocycle towards electrophilic substitution and strong nucleophiles. In this manner, porphine allows for the sequential introduction of substituents, yielding symmetric and less symmetric systems, which are difficult to achieve by other synthetic routes.² Accordingly, the surface templated assembly of porphine offers a promising strategy for controlled porphyrin functionalisation.

The metal chelates of porphine are the simplest metalloporphyrins. Introduction of a divalent metal produces a more electronegative porphyrin ligand (MgP>ZnP>CuP>NiP>PdP), activating substitution at the meso-carbon positions.³ In this respect, the nickel chelate of porphine occupies a unique position for its reactivity toward Vilsmeier formylation, which leads exclusively to the meso-substituted derivative (Appendix A, Figure 6). Concerning the surface confinement and subsequent functionalisation of nickel porphine, a fundamental knowledge of the molecule-substrate interface is required. The literature on the subject of surface supported (nickel) porphine, however, remains far less developed than that of the more synthetically accessible meso-tetrasubstituted or β -octasubstituted porphyrins. The self-assembly of nickel(II) tetraphenylporphyrin on the Au(111) surface,⁴ and nickel(II) octaethylporphyrin (NiOEP) (App. A, Fig. 6) on both Au(111)^{4, 5} and highly ordered pyrolytic graphite (HOPG)⁶ have previously been reported.

More recently, the thermally-controlled formation of covalently bonded nickel porphyrin networks was demonstrated.⁷

In the present work, vapour deposited (porphyrinato)nickel(II) (NiP) molecules (Figure 3.1) on the Ag/Si(111)-($\sqrt{3} \times \sqrt{3}$)R30° (Ag/Si(111)- $\sqrt{3}$) and Ag(111) surfaces are examined for the first time using scanning tunnelling microscopy (STM) and low energy electron diffraction (LEED). STM is used in order to determine the conformational behaviour of NiP molecules in monolayer to bilayer regimes. Combining this technique with LEED, the registry of the molecular overlayer with the substrate is revealed.

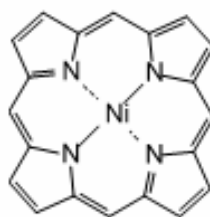


Figure 3.1. Structural formula of the NiP molecule.

3.2. Experimental methods

The STM and LEED experiments were conducted in ultra-high-vacuum, using a commercial system (Omicron Nanotechnology GmbH) consisting of an analysis chamber and a preparation chamber, with a base pressure below 1×10^{-10} mbar; as described in Chapter 2.

STM imaging was performed at room-temperature, using an Omicron VT STM. Electrochemically etched polycrystalline W tips (Omicron) were used as tunnelling probes. The STM images were recorded in constant-current mode, with the given voltages (V_{sample}) corresponding to the sample-bias with respect to the W tip. The STM data were processed using the WSxM software package.⁸

The LEED diffraction patterns were obtained using an Omicron four grid Spectraled system, fitted with rear-view optics and LaB₆ filament. Analysis of the diffraction patterns was performed using the LEEDpat 2.1 pattern simulator.⁹

The Ag/Si(111)- $\sqrt{3}$ substrate was prepared from a p-type (boron-doped) Si(111) wafer. Atomically clean Si(111)-(7 × 7) surfaces were prepared by *in situ* direct current heating to 1520 K, subsequent to being outgassed at 870 K for 12 hours. The Ag/Si(111)- $\sqrt{3}$ reconstruction was prepared by depositing silver (Goodfellow Metals, 5 N) by e-beam evaporation from a molybdenum crucible onto the Si substrate, which was maintained at 770 K during the deposition. The Ag(111) crystal (Surface Preparation Laboratory) was cleaned *in situ* by repeated cycles of argon ion sputtering ($U = 1$ kV) and annealing at 850 K. The cleanliness of the substrates was verified by STM and LEED before deposition of the NiP. The NiP was synthesized according to a published procedure.¹⁰ Prior to deposition, the NiP powder was outgassed below its evaporation temperature. The NiP was subsequently evaporated in a preparation chamber, isolated from the analysis chamber, at a rate of 0.1 - 0.2 ML (monolayer) per minute from a tantalum crucible in a homemade deposition cell operated at a temperature of approximately 600 K. The NiP surface coverage is defined as the number of adsorbed molecules divided by the number in a filled monolayer

3.3. Results and discussion

3.3.1. NiP on the Ag/Si(111)-($\sqrt{3} \times \sqrt{3}$)R30° surface

Deposited at low coverage on the Ag/Si(111)- $\sqrt{3}$ surface, the NiP molecules behave as a two-dimensional gas, displaying high mobility in STM images. As monolayer coverage is approached, however, the NiP molecules self-assemble forming a well defined hexagonal closed-packed array. Figure 3.2(a) shows a typical occupied state STM image obtained at monolayer coverage; the inset shows an enlarged view, in which an individual molecule is highlighted. The hexagonal unit cell of the NiP lattice contains one molecule; the lengths of the primitive lattice vectors (b_1 and b_2) are equal to 1.2 ± 0.1 nm, while the subtended angle

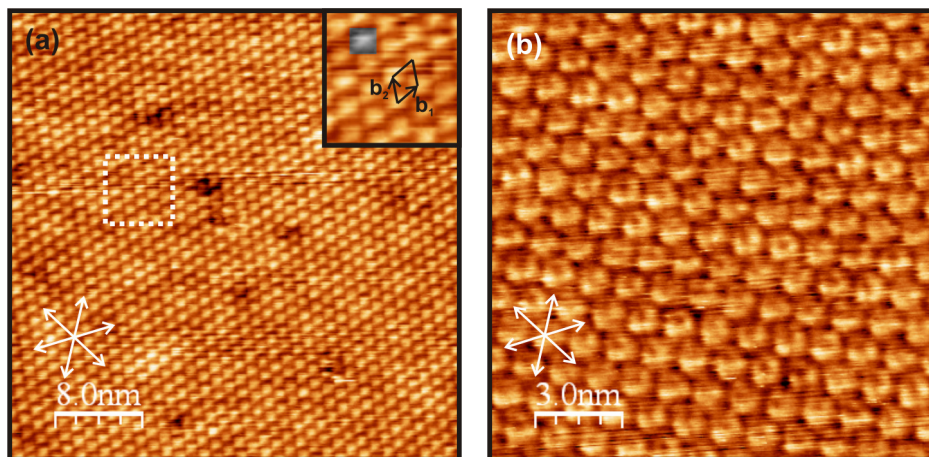


Figure 3.2. STM images obtained from the NiP monolayer on the Ag/Si(111)- $\sqrt{3}$ surface. The close-packed directions of the Ag/Si(111)- $\sqrt{3}$ surface are indicated by white arrows. (a) Large-scale occupied state STM image; $V_{\text{sample}} = -1.0$ V, $I_t = 0.025$ nA, size 40 nm \times 40 nm. The inset shows an enlarged view of the region highlighted by the white dotted box; an individual NiP molecule is indicated in greyscale; the unit cell and primitive lattice vectors (b_1 , b_2) are shown in black. (b) High resolution occupied state STM image; $V_{\text{sample}} = -1.5$ V, $I_t = 0.05$ nA, size 15 nm \times 15 nm.

is $60 \pm 2^\circ$. The apparent size of an individual NiP molecule is ~ 1.1 nm. From the molecular dimensions, it follows that the average plane of the porphyrin macrocycle lies parallel to that of the Ag/Si(111)- $\sqrt{3}$ surface. This is in close agreement with the lattice structure, and apparent molecular size, reported for CoP molecules on the Au(111) surface (imaged in HClO_4).¹¹

At high resolution, the individual NiP molecules display a depression in the apparent height at the porphyrin core, as demonstrated in the occupied state STM image of Figure 3.2(b). In like manner, the analogous NiOEP⁶ and NiTPP⁴ molecules are also reported to show a characteristic core depression. It is well established that the apparent core height of metallotetrapyrroles (in tunnelling images) is uniquely related to the central metal atom.^{12, 13} In the case of the closely related metallophthalocyanines (M-Pc) (Appendix A, Figure 7), the apparent core height has been shown to be strongly influenced by the d-orbital contribution near the Fermi level.^{12, 13} Where the d-orbital contribution of the central metal atom is expected to be either small (Ni, Cu) or large (Fe, Co), a core depression and protrusion respectively, are observed. These findings are supported by

tunnelling images of the corresponding (Fe,¹⁴ Co,¹⁴ Cu¹⁵) metallo-TPPs; perhaps most notably in the case of NiTPP⁴. Notwithstanding the evident electronic nature of the apparent core heights, a small displacement (~ 8 pm) of the central Ni metal atom from average plane of the porphyrin macrocycle is noted from the crystal structure of NiP¹⁶. Therefore, in the present case, the observed core depression may be expected to reflect a combination of both electronic and topological contributions to the apparent height.

Depending on the STM tip state and applied bias voltage, the imaged molecular overlayer reveals distinctive features of the underlying Ag/Si(111)- $\sqrt{3}$ surface. The energy onset of the highest occupied state of the Ag/Si(111)- $\sqrt{3}$ surface is located ~ 0.2 eV below the Fermi level,¹⁷ and thus lies within the energy gap of the highest occupied (HOMO) and lowest unoccupied molecular orbitals (LUMO) of the NiP molecules^{18, 19}. It follows that in the energy range of the HOMO-LUMO gap the overlayer molecules may become electronically transparent. Yet it is found that the W tunnelling tip must undergo a reconstruction in order for the apparent bias dependency to come in to effect. A similar effect has been reported in a recent study of the surface structure of Ag/Si(111)- $\sqrt{3}$; wherein the Si trimers beneath the Ag monolayer were directly observed under a special tip condition.^{20, 21} On the Ag/Si(111)- $\sqrt{3}$ surface, the Ag atoms which remain after the formation of the ($\sqrt{3} \times \sqrt{3}$) reconstruction exist a diffuse gas phase.¹⁷ In the present case, therefore, the modification of the tip apex by a Ag atom is considered plausible. By means of the so-called “dual scan mode STM” surface topography can be obtained in both the forward and backward scan directions. Accordingly, under appropriate bias conditions, it was possible to image both the overlayer and the substrate together. Examples of such dual scan mode STM images obtained from the NiP overlayer on the Ag/Si(111)- $\sqrt{3}$ surface are shown in Figure 3.3. Here, the sample bias in the forward scan direction (-1.4V) lies outside HOMO-LUMO gap of the NiP molecules, whilst that applied in the backward direction (-0.2V) lies within the energy gap. In the forward scan direction the typical closed-packed structure of the NiP overlayer is observed (Fig. 3.2 (a) and (c)). However, in the backward direction, the Ag/Si(111)- $\sqrt{3}$ substrate is imaged through molecular overlayer (Fig. 3.2 (b) and (d)). This apparent transparency of the molecular overlayer has been reported previously for Co- and Cu-Pc on the Ag/Si- $\sqrt{3}$ ²² and Si(111)²³ surfaces respectively; in the latter case the observation of substrate features beneath the molecular

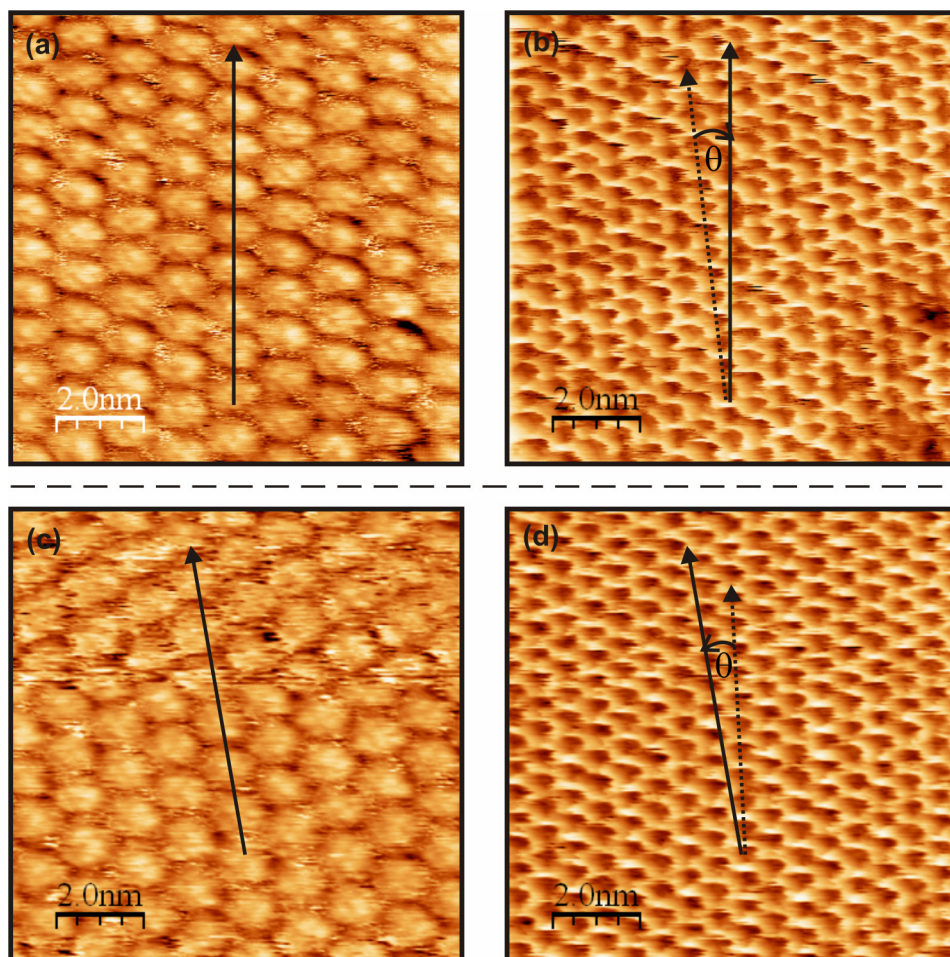


Figure 3.3. STM dual scan mode images obtained from the NiP monolayer on the Ag/Si(111)- $\sqrt{3}$ surface. NiP overlayer shown in forward scan direction (a) and (c); $V_{\text{sample}} = -1.40$ V, $I_t = 0.25$ nA, size 10 nm \times 10 nm. Ag/Si(111)- $\sqrt{3}$ surface shown in backward scan direction (b) and (d); $V_{\text{sample}} = -0.20$ V, $I_t = 0.25$ nA, size 10 nm \times 10 nm. Images (a) and (c) reflect the clockwise and counter-clockwise rotated mirror domains, respectively. The close-packed directions of the overlayer and substrate are indicated by solid and dotted lines, respectively.

layer was attributed to tunnelling from surface states within the CuPc HOMO-LUMO gap. By this means, a comparison of NiP overlayer and Ag/Si(111)- $\sqrt{3}$ substrate lattices reveals their relative orientation. For a single domain, it is found that the principal lattice vector (b_1) of the molecular overlayer shows an azimuthal rotation of $7 \pm 1^\circ$ relative to the that of the Ag/Si(111)- $\sqrt{3}$ substrate. Two such domains are observed, described by either a clockwise or counter-clockwise rotation, as demonstrated by the upper and lower images of

Figure 3, respectively. Thus the NiP overlayer lattice is seen to form two mirror domains, the plane of which follows the $\langle \bar{1} \bar{1} 2 \rangle$ crystallographic directions of the Ag/Si(111)- $\sqrt{3}$ surface. The formation of such mirror molecular domains azimuthally rotated about substrate high symmetry directions has also been reported for tetrakis(3,5-di-tert-butylphenyl)porphyrin (App. A, Fig. 4) adsorbed on the Cu(100) surface.²⁴

Figure 3.4(a) shows the LEED pattern obtained from approximately 1ML of the NiP molecules on the Ag/Si(111)- $\sqrt{3}$ surface. Twelve first order diffraction spots are observed, forming two equivalent hexagonal patterns centred about the zero order spot. Each hexagon is interpreted as being that of a superposition of three rotationally equivalent domains of a hexagonal lattice; hence, the pattern reflects two mirror domains. The angle between the mirror domains is equal to $14 \pm 2^\circ$, in excellent agreement with that determined by means of the STM. The individual hexagonal patterns are highlighted (Figure 3.4(a)), with the reciprocal lattice vectors of one domain given as b^*_1 and b^*_2 , with the subtended angle β^* equal to $60 \pm 2^\circ$. Accordingly, the lattice vectors of the molecular overlayer may be expressed in terms of those of the substrate through the following transformation:

$$\begin{pmatrix} b_1 \\ b_2 \end{pmatrix} = \begin{pmatrix} 2.0 & 1.2 \\ -1.2 & 0.80 \end{pmatrix} \begin{pmatrix} a_1 \\ a_2 \end{pmatrix}$$

where the length of the Ag/Si(111)- $\sqrt{3}$ primitive lattice vector is 0.68nm. A corresponding model for the NiP overlayer lattice (in the case of the clockwise rotated domain) superimposed on that of the Ag/Si(111)- $\sqrt{3}$ surface, is shown in Figure 3.4(b). While the primitive unit cell dimensions of the molecular overlayer lattice preclude a commensurate registry to that of the substrate, the corresponding (3 \times 3) super-cell is seen to approach a coincident configuration. In this arrangement some of the overlayer lattice points are found coincide with substrate lattice lines. As such, it is tentatively proposed that the super-cell represents the coincident nature of the molecule-substrate interface.

A Moiré pattern, with a periodicity larger than that of the primitive unit cell, is exhibited in STM images of the NiP overlayer. Figure 3.5(a) shows a long-range intensity modulation, a hexagonal Moiré pattern, superimposed on the closed-packed structure of the

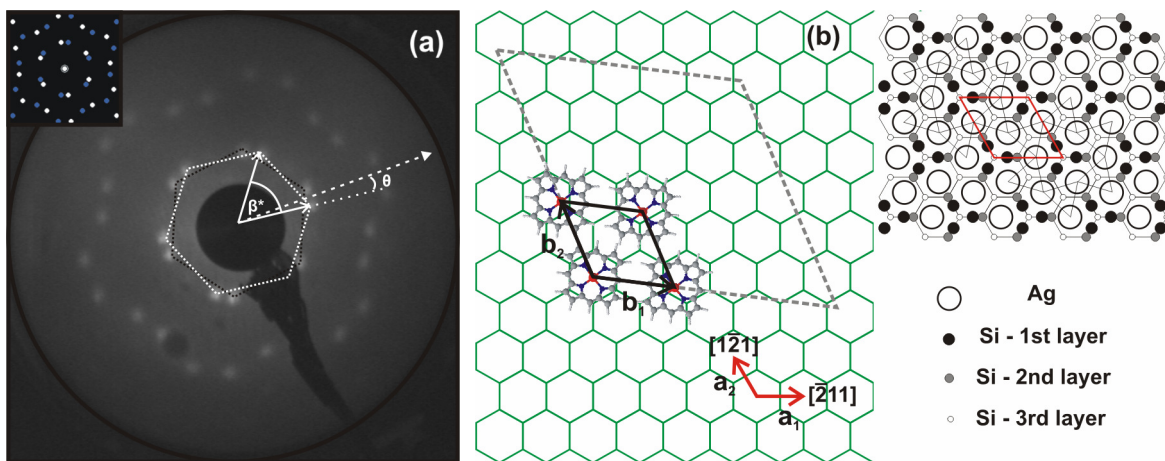


Figure 3.4. (a) LEED pattern from 1ML of the NiP molecules on the Ag/Si(111)- $\sqrt{3}$ surface acquired at a primary beam energy of 18.0 eV. The inset shows a simulated LEED pattern of the NiP overlayer created using the observed lattice parameters. The mirror domains of the NiP overlayer are indicated by the black and white hexagons. The dotted line shows the close packed direction of the Ag(111) reciprocal lattice; whereby, the angle θ indicates the azimuthal rotation of the molecular overlayer. (b) Schematic representation of the azimuthal orientation of the NiP overlayer (clockwise rotated domain) on the Ag/Si(111)- $\sqrt{3}$ surface. The honeycomb lattice represents the Ag/Si(111)- $\sqrt{3}$ surface: a Ag and Si trimer at the vertex and centre of each hexagon – as illustrated by the inset model. The lattice vectors of the Ag(111) surface and NiP overlayer are labelled a_1 , a_2 and b_1 , b_2 , respectively; the dashed lines (grey) outline the coincident overlayer super-cell.

NiP molecules; the corresponding autocorrelation pattern (of the region enclosed by the dotted box) is shown inset. The distance between the centres of the bright (or dark) regions, as discerned from the autocorrelation pattern, is equal to ~ 3.7 nm. Here, the periodicity of the Moiré pattern can be expected to be characteristic of the lattice mismatch of the overlayer and substrate.²⁵ In this respect, the proposed coincidence of the molecular overlayer and substrate lattices (for the (3×3) super-cell) is consistent, within the uncertainty, with the periodicity of the observed moiré pattern. Similarly, for the principal layer of copper hexadecachlorophthalocyanine (CuPcCl_{16}) (App. A, Fig. 7) on HOPG, the observation of a periodic intensity modulation consistent with a Moiré pattern is attributed to a coincidence structure.²⁶

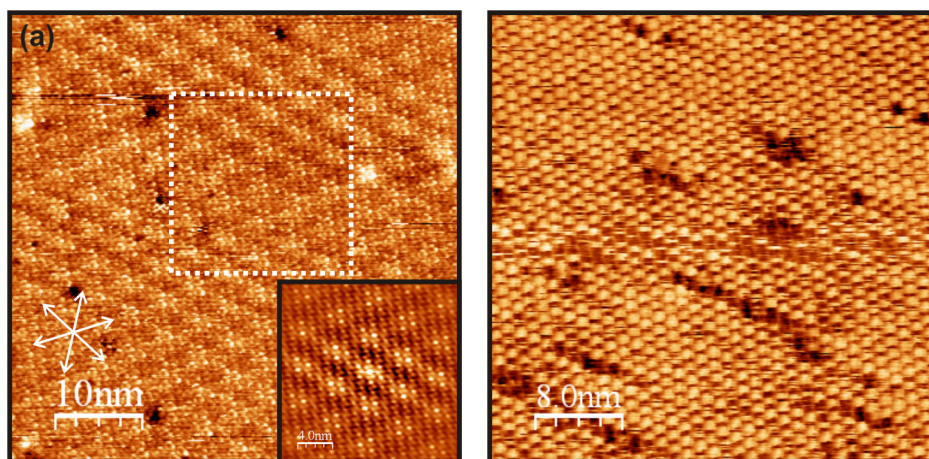


Figure 3.5. STM images obtained from the NiP overlayer on the Ag/Si(111)- $\sqrt{3}$ surface. (a) Large-scale occupied state STM image of the NiP monolayer in which a moiré pattern is present; $V_{\text{sample}} = -1.4$ V, $I_t = 0.5$ nA, size 50 nm \times 50 nm. The close-packed directions of the Ag/Si(111)- $\sqrt{3}$ surface are indicated by white arrows. (b) STM image obtained at a NiP coverage of ~ 2 ML; $V_{\text{sample}} = -1.75$, $I_t = 0.75$ nA, size 40 nm \times 40 nm.

Figure 3.5(b) shows a typical occupied state STM image of the NiP overlayer at a coverage approaching 2ML. The ordering of the second NiP layer is seen to preserve the same planarity and hexagonal ordering as the first molecular layer. It should be noted that this differs from the native bulk layer structure, for which a lateral shift (~ 1.5 Å) between the porphyrin planes is observed.¹⁶ In the apparent absence of a structural transition from the first molecular overlayer, it is concluded that multilayer growth is influenced by the underlying Ag/Si(111)- $\sqrt{3}$ surface.

3.3.2. NiP on the Ag(111) surface

The NiP molecules self-assemble when deposited on the Ag(111) surface, forming a hexagonal closed packed structure at monolayer coverage. Figure 3.6(a) shows a typical occupied state STM image of the highly ordered NiP monolayer; an enlarged view, highlighting an individual molecule, is shown inset. The lattice parameters of the NiP monolayer, with the exception of the azimuthal orientation relative to the Ag(111) substrate (discussed below), are the same as those found on Ag/Si(111)- $\sqrt{3}$ surface. Similarly, the

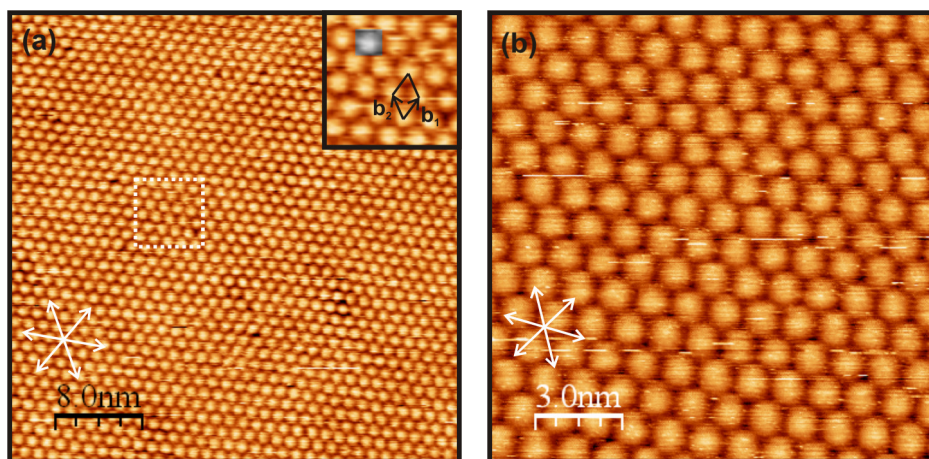


Figure 3.6. STM images obtained from the NiP monolayer on the Ag(111) surface. The close-packed directions of the underlying Ag(111) surface are indicated by white arrows. (a) Large-scale occupied state STM image; $V_{\text{sample}} = -1.2$ V, $I_t = 0.25$ nA, size 40 nm \times 40 nm. The inset shows an enlarged view of the region highlighted by the white dotted box; an individual NiP molecule is indicated in greyscale; the unit cell and primitive lattice vectors (b_1 , b_2) are shown in black. (b) High resolution occupied state STM image; $V_{\text{sample}} = -1.25$ V, $I_t = 0.2$ nA, size 15 nm \times 15 nm.

unit cell dimensions indicate a flat lying configuration of the NiP molecules on the Ag(111) surface. Hence, the observed ordering may be considered typical of that found on low reactivity surfaces, whereby self-assembly is governed by van der Waals interactions involving the outer pyrrolic hydrogen atoms of the NiP molecules. Figure 3.6(b) shows a higher resolution occupied state STM image of the NiP monolayer on the Ag(111) surface. Though of higher pixel resolution, the core height remains unresolved, thus precluding a comparison with that observed in the case of the Ag/Si(111)- $\sqrt{3}$ surface.

The LEED pattern obtained from approximately 1ML of the NiP molecules on the Ag(111) surface is shown in Figure 3.7(a). The pattern is found to resemble that observed from the molecular overlayer on the Ag/Si(111)- $\sqrt{3}$ substrate: twelve first order diffraction spots forming two equivalent hexagons. Similarly, the hexagonal patterns form mirror images of each other, with the mirror plane aligned along the substrate close-packed directions. The angle between the mirror domains is equal to $12 \pm 2^\circ$, representing a clockwise and counter-clockwise rotation of $\pm 6^\circ$. The mirror domains (hexagons) are highlighted, with the reciprocal lattice vectors of one domain given as b^*_1 and b^*_2 , with the

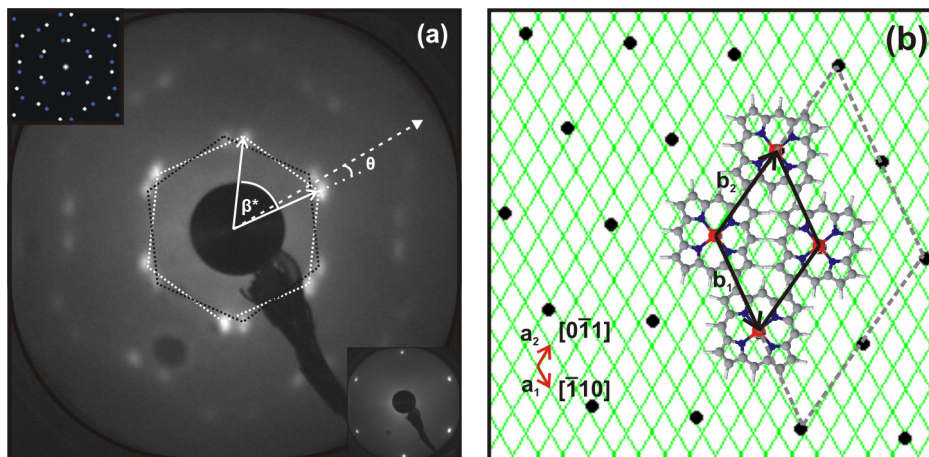


Figure 3.7. (a) LEED pattern from 1ML of the NiP molecules on the Ag(111) surface acquired at a primary beam energy of 14.0 eV. The insets show the LEED pattern of the Ag(111) surface acquired separately at the higher beam energy of 112.0 eV (lower) and a simulated LEED pattern of the NiP overlayer created using the observed lattice parameters (upper). The mirror domains of the NiP overlayer are indicated by the black and white hexagons. The dotted line shows the close packed direction of the Ag(111) reciprocal lattice; whereby, the angle θ indicates the azimuthal rotation of the molecular overlayer. (b) Schematic representation of the azimuthal orientation of the NiP overlayer (clockwise rotated domain) on the Ag(111) surface. The black dots represent the NiP molecules with the points of intersection of the green mesh that of the Ag atoms. The lattice vectors of the Ag(111) surface and NiP overlayer are labelled a_1 , a_2 and b_1 , b_2 , respectively; the dashed lines (grey) outlines the coincident overlayer super-cell.

angle between them β^* equal to $60 \pm 2^\circ$. It follows from this preferred orientation that the NiP overlayer grows epitaxially on the Ag(111) surface. The lattice vectors of the molecular overlayer may be expressed in terms of those of the substrate through the following transformation:

$$\begin{pmatrix} b_1 \\ b_2 \end{pmatrix} = \begin{pmatrix} 4.4 & 0.50 \\ -0.50 & 3.9 \end{pmatrix} \begin{pmatrix} a_1 \\ a_2 \end{pmatrix}$$

where the Ag(111) nearest-neighbour distance is 0.289nm. A model of the corresponding NiP overlayer lattice (in the case of the clockwise rotated domain) superimposed on that of

the Ag(111) surface is shown in Figure 3.7(b). As seen from the graphic, a commensurate registry to the substrate lattice is prevented by the primitive unit cell dimensions of the molecular overlayer. However, it is clearly seen that the corresponding (2×2) super-cell approaches a coincident configuration. Furthermore, every overlayer lattice point is found to coincide with one of the substrate lattice lines. Therefore, the nature of the overlayer-substrate interface is consistent with that previously described as point-on-line coincidence.²⁵ Here it is noted that the apparent absence of a distinct Moiré pattern in STM images of the NiP on the Ag(111) surface, may reflect the observed coherence of the overlayer and substrate lattices at the reduced super-cell size.

A structural transition occurs at the growth of the second layer, leading to the formation of extended molecular rows. Figure 3.8 (a), (c) and (d) show occupied state STM images of the NiP overlayer in which individual molecules of the first and the second layers appear as dark and bright protrusions, respectively. The molecules of the second layer are found to self-assemble along the direction of one of the primitive lattice vectors of the first layer, forming parallel “nanolines”, with lengths reaching the extents of the terrace width. The intermolecular distance along a row is found to be the same as that of the first layer. It is seen that the molecular rows occur singly (Fig. 3.8(a)) or as pairs (Fig 3.8(c)), so-called “nanoribbons”, separated by a missing row structure; as evidenced by the line profile of Figure 3.8(b). In accordance with the three fold symmetry of the underlying monolayer lattice, rotational domains of the molecular rows subtended by an angle of $\sim 120^\circ$ with respect to each other are observed (Fig. 3.8(d)). In the case of CuPcF₁₆ (App. A, Fig. 7) on HPOG, the reported multilayer growth shows similar features, whereby, molecules of the second layer are observed to form parallel molecular-dot-chains along the row direction of the underlying first layer molecules.²⁷

From close inspection of the multilayer STM images (Fig. 3.8), it is clearly seen that molecules of the second layer sit approximately on top of those from the first layer, in a flat lying configuration - as indicated from the molecular packing dimensions. In this arrangement the molecules can be expected interact strongly between the overlayers via π - π interactions. The growth of the NiP second layer on the Ag(111) surface departs considerably from that found on the Ag/Si(111)- $\sqrt{3}$ substrate (see above), where no transition from the first layer structure is observed. It follows that on the Ag(111) surface

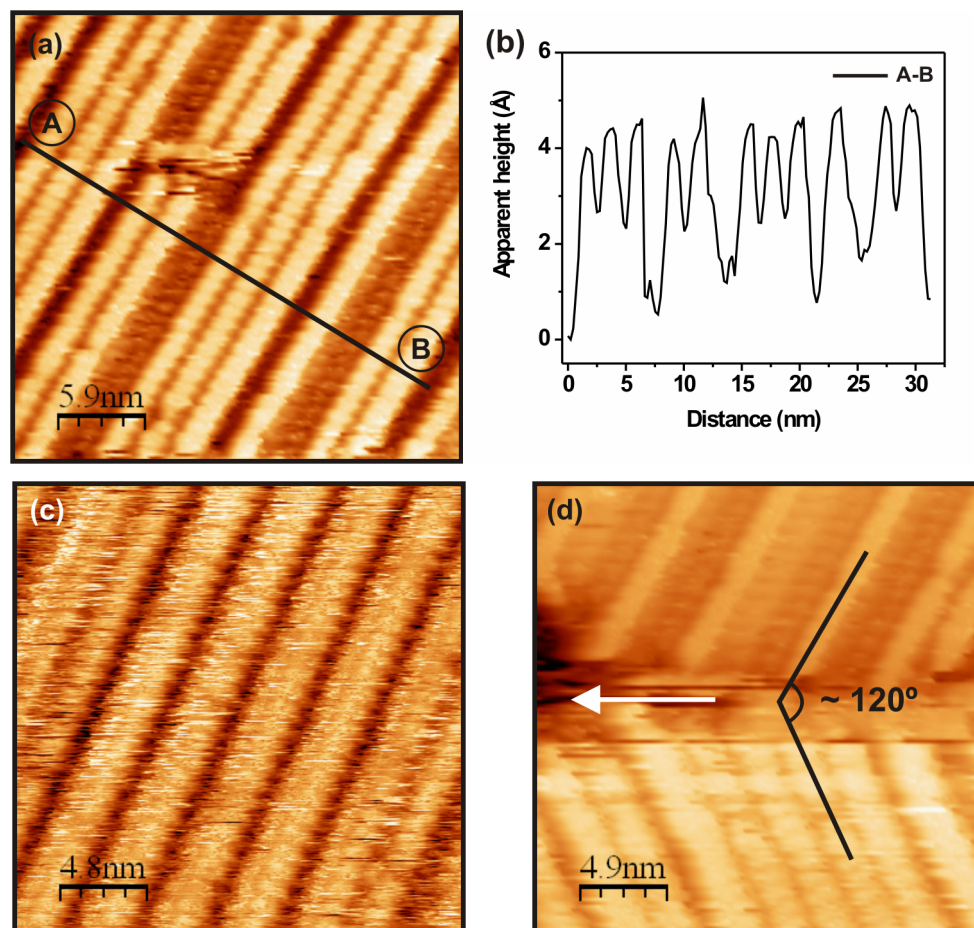


Figure 3.8. (a) Unoccupied state STM image of molecular rows occurring as single “nanolines”; $V_{\text{sample}} = +1.4$ V, $I_t = 0.20$ nA, size 30 nm \times 30 nm. (b) Height profile taken along the line AB. (c) Molecular rows occurring in “nanoribbon” pairs; $V_{\text{sample}} = +1.50$ V, $I_t = 0.30$ nA, size 20 nm \times 20 nm. (d) Two rotational domains of the molecular rows observed on adjacent terraces; $V_{\text{sample}} = +1.4$ V, $I_t = 0.20$ nA, size 24 nm \times 24 nm. The white arrow indicates the direction of the step edge.

the NiP intralayer interactions are stronger than those between the overlayers and substrate. In the native bulk layer structure of NiP a lateral shift of ~ 1.5 Å is observed.¹⁶ Such an arrangement in the present case might be expected to reduce the effective overlap of the molecular π systems. It is therefore speculated that the formation of molecular rows at the growth of the second layer, reflects a transition to the native bulk layer structure of the NiP.

3.4. Summary

The growth and ordering of NiP molecules on the Ag/Si(111)- $\sqrt{3}$ and Ag(111) surfaces have been investigated using STM and LEED. The NiP molecules are found to self-assemble on both substrates at room-temperature, forming well defined hexagonal closed-packed structures at monolayer coverage. The average plane of the porphyrin macrocycle is found to lie parallel to that of the substrate. In accordance with the three-fold symmetry of the substrates, three rotationally equivalent domains of the molecular overlayer are observed. The principal lattice vectors of the NiP overlayer show an azimuthal rotation relative to those of the Ag/Si(111)- $\sqrt{3}$ and Ag(111) surfaces of $\pm 7 \pm 2^\circ$ and $\pm 6 \pm 2^\circ$, respectively. Consequently, two mirror domains of the NiP overlayer are formed, with the mirror planes lying respectively along the $\langle \bar{1}10 \rangle$ and $\langle \bar{2}11 \rangle$ crystallographic directions of the Ag(111) and Ag/Si(111)- $\sqrt{3}$ surfaces. The NiP molecules forming the second layer on the Ag/Si- $\sqrt{3}$ surface preserve the same planarity and hexagonal ordering as the first molecular layer. On the Ag(111) surface, the second layer NiP molecules self-assemble along the direction of one of the primitive lattice vectors of the first layer, forming parallel molecular rows which are separated by a uniform “missing row” structure.

3.5. References

- (1) Dogutan, D. K.; Ptaszek, M.; Lindsey, J. S. Direct synthesis of magnesium porphine via 1-formyldipyrrromethane. *J. Org. Chem.* **2007**, *72*, 5008-5011.
- (2) Senge, M. O. Stirring the porphyrin alphabet soup - functionalization reactions for porphyrins. *Chem. Commun.* **2011**, *47*, 1943-1960.
- (3) Milgrom, L. R. (1997) *The colours of life: an introduction to the chemistry of porphyrins and related compounds*. Oxford University Press: Oxford.
- (4) Teugels, L. G.; Avila-Bront, L. G.; Sibener, S. J. Chiral domains achieved by surface adsorption of achiral nickel tetraphenyl- or octaethylporphyrin on smooth and locally kinked Au(111). *J. Phys. Chem. C* **2011**, *115*, 2826-2834.

- (5) Resta, A.; Felici, R.; Kumar, M.; Pedio, M. Ni and Cu octaethyl porphyrins ordered monolayer on Au(111) surfaces. *J. Non Cryst. Solids* **2010**, *356*, 1951-1954.
- (6) Ogunrinde, A.; Hipps, K.; Scudiero, L. A scanning tunneling microscopy study of self-assembled nickel(II) octaethylporphyrin deposited from solutions on HOPG. *Langmuir* **2006**, *22*, 5697-5701.
- (7) Krasnikov, S. A.; Doyle, C. M.; Sergeeva, N. N.; Preobrajenski, A. B.; Vinogradov, N. A.; Sergeeva, Y. N.; Zakharov, A. A.; Senge, M. O.; Cafolla, A. A. Formation of extended covalently bonded Ni porphyrin networks on the Au(111) surface. *Nano Res.* **2011**, *4*, 376-384.
- (8) Horcas, I.; Fernandez, R.; Gomez-Rodriguez, J. M.; Colchero, J.; Gomez-Herrero, J.; Baro, A. M. WSXM: A software for scanning probe microscopy and a tool for nanotechnology. *Rev. Sci. Instrum.* **2007**, *78*, 013705.
- (9) Hermann, K.; Van Hove, M. A. LEED pattern simulator LEEDpat Version 2.1 (2006). <http://www.fhi-berlin.mpg.de/KHsoftware/LEEDpat/index.html>.
- (10) Unger, E.; Bobinger, U.; Dreybrodt, W.; Schweitzerstenner, R. Vibronic coupling in Ni(ii) porphine derived from resonant raman excitation profiles. *J. Phys. Chem.* **1993**, *97*, 9956-9968.
- (11) Yoshimoto, S.; Inukai, J.; Tada, A.; Abe, T.; Morimoto, T.; Osuka, A.; Furuta, H.; Itaya, K. Adlayer structure of and electrochemical O₂ reduction on cobalt porphine-modified and cobalt octaethylporphyrin-modified Au(111) in HClO₄. *J. Phys. Chem. B* **2004**, *108*, 1948-1954.
- (12) Lu, X.; Hipps, K. Scanning tunneling microscopy of metal phthalocyanines: d(6) and d(8) cases. *J. Phys. Chem. B* **1997**, *101*, 5391-5396.
- (13) Lu, X.; Hipps, K.; Wang, X.; Mazur, U. Scanning tunneling microscopy of metal phthalocyanines: d(7) and d(9) cases. *J. Am. Chem. Soc.* **1996**, *118*, 7197-7202.
- (14) Buchner, F.; Kellner, I.; Hieringer, W.; Goerling, A.; Steinrueck, H.; Marbach, H. Ordering aspects and intramolecular conformation of tetraphenylporphyrins on Ag(111). *Phys. Chem. Chem. Phys* **2010**, *12*, 13082-13090.

- (15) Brede, J.; Linares, M.; Kuck, S.; Schwoebel, J.; Scarfato, A.; Chang, S.; Hoffmann, G.; Wiesendanger, R.; Lensen, R.; Kouwer, P. H. J.; Hoogboom, J.; Rowan, A. E.; Broering, M.; Funk, M.; Stafstrom, S.; Zerbetto, F.; Lazzaroni, R. Dynamics of molecular self-ordering in tetraphenyl porphyrin monolayers on metallic substrates. *Nanotechnology* **2009**, *20*, 275602.
- (16) Jentzen, W.; Turowska-Tyrk, I.; Scheidt, W.; Shelnutt, J. Planar solid-state and solution structures of (porphinato)nickel(II) as determined by x-ray diffraction and resonance Raman spectroscopy. *Inorg. Chem.* **1996**, *35*, 3559-3567.
- (17) Sato, N.; Nagao, T.; Hasegawa, S. Si(111)-($\sqrt{3} \times \sqrt{3}$)-Ag surface at low temperatures: symmetry breaking and surface twin boundaries. *Surf. Sci.* **1999**, *442*, 65-73.
- (18) Rosa, A.; Ricciardi, G.; Baerends, E.; van Gisbergen, S. The optical spectra of NiP, NiPz, NiTBP, and NiPc: Electronic effects of meso-tetraaza substitution and tetrabenzo annulation. *J. Phys. Chem. A* **2001**, *105*, 3311-3327.
- (19) Liao, M.; Scheiner, S. Electronic structure and bonding in metal porphyrins, metal = Fe, Co, Ni, Cu, Zn. *J. Chem. Phys.* **2002**, *117*, 205-219.
- (20) Zhang, H. M.; Gustafsson, J. B.; Johansson, L. S. O. The tip role on STM images of Ag/Si(111)- $\sqrt{3} \times \sqrt{3}$. *JPCS* **2007**, *61*, 1336-1340.
- (21) Zhang, H. M.; Gustafsson, J. B.; Johansson, L. S. O. Surface atomic structure of Ag/Si(111)- $\sqrt{3} \times \sqrt{3}$. *Phys. Rev. B* **2006**, *74*, 201304.
- (22) Upward, M.; Beton, P.; Moriarty, P. Adsorption of cobalt phthalocyanine on Ag terminated Si(111). *Surf. Sci.* **1999**, *441*, 21-25.
- (23) Kanai, M.; Kawai, T.; Motai, K.; Wang, X. D.; Hashizume, T.; Sakura, T. Scanning-tunneling-microscopy observation of copper-phthalocyanine molecules on Si(100) and Si(111) surfaces. *Surf. Sci.* **1995**, *329*, L619-L623.
- (24) Sekiguchi, T.; Wakayama, Y.; Yokoyama, S.; Kamikado, T.; Mashiko, S. Adsorption-induced conformational changes of porphyrin derivatives and formation of twin superstructures on a copper surface. *Thin Solid Films* **2004**, *464-465*, 393-397.
- (25) Hooks, D. E.; Fritz, T.; Ward, M. D. Epitaxy and molecular organization on solid substrates. *Adv. Mater.* **2001**, *13*, 227-241.

(26) Irie, S.; Hoshino, A.; Kuwamoto, K.; Isoda, S.; Miles, M.; Kobayashi, T. Point-on-line coincidence in epitaxial growth of CuPcCl₁₆ on graphite. *Appl. Surf. Sci.* **1997**, *113*, 310-315.

(27) Huang, H.; Chen, W.; Wee, A. T. S. Low-temperature scanning tunneling microscopy investigation of epitaxial growth of F₁₆CuPc thin films on Ag(111). *J. Phys. Chem. C* **2008**, *112*, 14913-14918.

On-surface synthesis of covalently coupled zinc(II) porphyrins

4.1. Introduction

On-surface covalent coupling represents a versatile synthetic route to obtaining metalloporphyrin assemblies of high stability.¹⁻⁷ Coupling reactions catalysed by coinage (Cu, Ag, Au) metal surfaces hold significant promise in on-surface synthesis. The surface-catalysed coupling of labile aryl-halide substituents on coinage metals is found to be highly effective in the formation of covalently interlinked metalloporphyrins.⁴ The general reaction pathway involves the thermally induced elimination of the halide moiety, and the subsequent covalent coupling of activated fragments.⁸ Depending on the affinity of the labile aryl-halide for the coordinating metal surface, the aryl-aryl coupling mechanism is found to follow two distinct activation steps. For metal surfaces of low reactivity, activation and coupling proceeds directly at the dissociation of the halide moiety.^{1, 2, 4} However, on more reactive surfaces, coordination of activated fragments to surface metal atoms leads to the formation of stable intermediate complexes.³ Consequently, the surface dependant pathways of such aryl-halide coupling reactions are decisive in the covalent linkage of (aryl-halide) substituted metalloporphyrins. In controlling this synthetic route, therefore, the surface dependant nature of the coupling mechanism is of particular interest.

The bifunctional aryl-halide, 2-bromothiophene, contains thiophenic sulphide (S) and labile bromide (Br) ligands (Appendix A, Figure 8), which may uniquely coordinate on coinage metal surfaces. The intrinsic dipole moment of 2-halothiophenes⁹ in turn facilitates distinct self-assembly through noncovalent interactions. Taken together, the balance of intermolecular and molecule-substrate interaction can be expected to mediate a variable affinity for coordinating metal surfaces. Through the lability of the terminal Br moiety,

covalent coupling can result in the formation of bithiophene linkage (App. A, Fig. 8), demonstrating electronic conjugation with corresponding mechanical strength. Accordingly, incorporating meso-bromothieryl substituents, the (5,10,15,20-tetrabromothien-2-ylporphyrinato)zinc(II) (ZnTBrThP) molecule is particularly well suited to examine coupling reactions which exhibit surface dependant pathways.

When self-assembled on metal surfaces, metalloporphyrins commonly adopt lateral arrangements suitable for covalent coupling of peripheral substituents; this is uniquely so when coupling fragments are coordinated by a common metal centre. As such, the extent to which self-assembly is substrate mediated provides an important insight into the activation step of on-surface covalent coupling. To clarify the coupling mechanism of the ZnTBrThP molecules, therefore, a fundamental knowledge of the molecule-substrate interface is required. In like manner, the determination of the elementary coupling motifs is decisive in understanding the formation of covalently interlinked ZnTBrThP molecules.

Here, vapour deposited ZnTBrThP molecules (Figure 4.1) on the Ag(111) and Au(111)-(22 × √3) surfaces are examined by using scanning tunnelling microscopy (STM), low energy electron diffraction (LEED) and x-ray photoelectron spectroscopy (XPS). The surface conformation and lateral arrangements of individual molecules are probed using STM. A combination of STM and LEED is used in order to reveal the structure and registry of the molecular overlayer with the substrate. XPS is used determine the molecule-substrate interaction, as reflected by site-specific molecular adsorption. The thermally induced elimination of the labile halide group is likewise confirmed. The resultant covalent coupling motifs are visualized directly by means of STM.

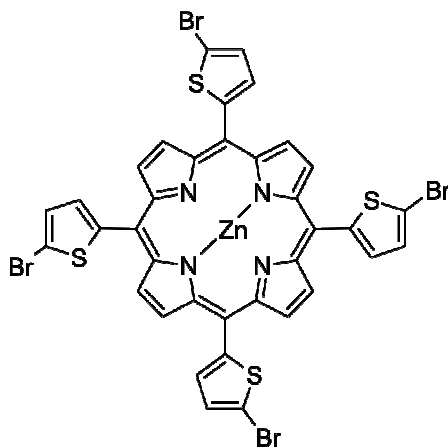


Figure 4.1. Structural formula of the ZnTBrThP molecule.

4.2. Experimental methods

The STM, LEED and XPS experiments were conducted in ultra-high-vacuum, (with a base pressure below 1×10^{-10} mbar), as described in Chapter 2. STM imaging was performed as described in Chapter 3. The STM data were processed using the WSxM software package.¹⁰ The LEED diffraction patterns were obtained as described in Chapter 3.

XPS measurements were carried out using an Omicron ESCA+ spectrometer. The core-level spectra were collected with a hemispherical energy analyzer (EA125 U5), employing an Al K_{α} x-ray source (DAR 400). The spectrometer was operated using a single analyzer pass energy, with an overall energy resolution of 1.4 eV. The core-level binding energies were referenced to the Ag 3d $_{5/2}$ line (368.2 eV) of the clean Ag surface. The XPS spectra were analyzed using the FITT 1.2 (GTK) software package (Photoelectron Spectroscopy Lab, Seoul National University).

Single-crystal Ag(111) and Au(111) surfaces (Surface Preparation Laboratory) were used as the substrates. The Ag(111) and Au(111) crystals were cleaned in situ by repeated cycles of argon ion sputtering followed by annealing as described for Ag(111) in Chapter 3. The ZnTBrThP was synthesized according to a published procedure.¹¹ The ZnTBrThP was evaporated at a rate of about 0.05 ML (monolayer) per minute, at a temperature of approximately 600 K. Experimental aspects of molecular deposition follow those described in Chapter 3.

4.3. Results and discussion

4.3.1. Assembly on the Ag(111) surface: metal-directed polymerisation

At low coverages, the deposited ZnTBrThP molecules exhibit a binding affinity for step edge and defect sites of the Ag(111) surface. Figure 4.2(a) shows a typical occupied state STM image of the ZnTBrThP molecules at a coverage of ~ 0.1 ML; an individual molecule is highlighted in the enlarged view shown inset. Whilst displaying apparent mobility on the terraces of the Ag(111) surface, the ZnTBrThP molecules are found to uniformly adsorb at

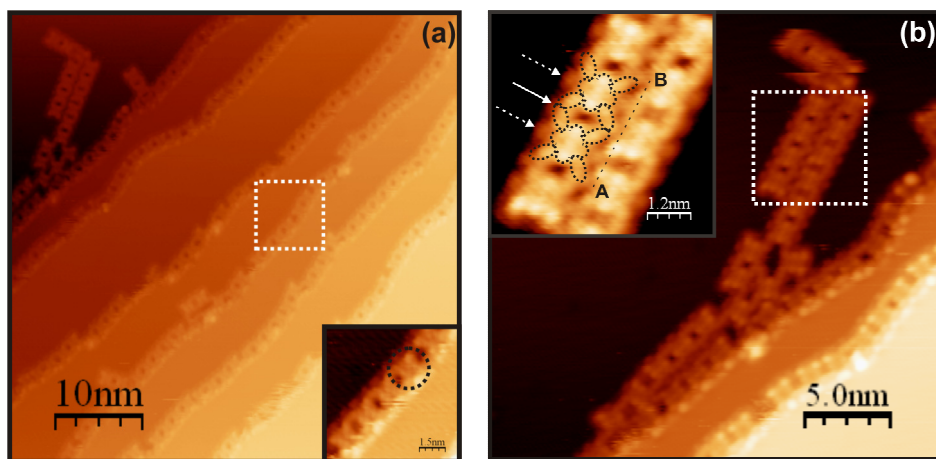
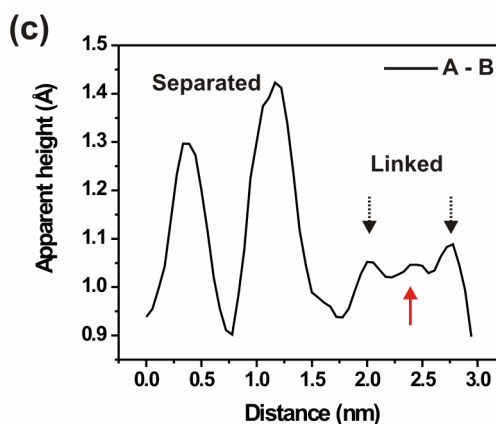


Figure 4.2. (a) and (b) STM images obtained from the ZnTBrThP molecules at a coverage of ~ 0.1 ML on the Ag(111) surface. (a) Large-scale occupied state STM image; $V_{\text{sample}} = -1.25$ V, $I_t = 0.20$ nA, size $50 \text{ nm} \times 50 \text{ nm}$. The inset shows an enlarged view of the region highlighted by the white dotted box; an individual ZnTBrThP molecule is circled. (b) High

resolution occupied state STM image; $V_{\text{sample}} = -1.25$ V, $I_t = 0.20$ nA, size $15 \text{ nm} \times 15 \text{ nm}$. The inset shows an enlarged view of the molecular chains highlighted by the white dotted box; individual molecules are outlined. The solid and dotted arrows indicate surface protrusions between bromothienyl groups and on the adjacent terrace, respectively. (c) Height profile taken along the (dotted) line (A – B) shown in the inset of (b).



the lower step edges. The change of surface atom coordination at a step, can give rise to a smoothing of the local electron density referred to as the Smoluchowski effect, whereby charge is shifted from the upper to lower step edges.¹² For benzene (Appendix A, Figure 9) on the Cu-¹³ and Au-¹⁴ (111) surfaces, an attraction to the decreased electron density of the upper step edges has been reported, reflective of its weak nucleophilic character. In the present case, it is proposed that the ZnTBrThP molecules act in electrophilic manner toward the increased electron density of the lower Ag(111) step edges.

Upon adsorption, the ZnTBrThP molecules appear to “link” together, thereby extending onto the terraces of the Ag(111) surface. Figure 4.2(b) shows a high resolution occupied state STM image taken at the above coverage, in which the initial growth of the molecular overlayer from the step edge is observed. The individual ZnTBrThP molecules are seen to display four terminal protrusions, with pair distances of ~ 1.0 and 1.6 \AA , consistent with the dimensions of the meso-bromothienyl groups. A corresponding set is observed for the central pyrrole groups of the macrocycle, with a single protrusion located at porphyrin core. It is found that each ZnTBrThP molecule links to its nearest neighbours end-on through at least two bromothienyl groups. On close inspection (Fig 4.2(b) inset), the Ag(111) surface displays small protrusions (dotted arrow) dotted periodically about the adsorbed ZnTBrThP molecules; notably, similar features (solid arrow) are observed between the connecting bromothienyl groups.

Notwithstanding several recent reports on the spontaneous dissociative adsorption of halo-aromatic molecules on metal surfaces,¹⁵⁻²⁰ it is noted that above observations may be rationalized in terms of adsorption of the undissociated ZnTBrThP molecules. In the case of 1,2- and 1,3-diiodobenzene (App. A, Fig. 9) on the Cu-(111)¹⁶ and (110)¹⁷ surfaces, cleavage of the carbon-iodine bonds is reported to occur at room temperature. The cleaved iodine atoms, observed as pairs of immobile protrusions in tunneling images, chemisorb near to the site of dissociation; while the resultant phenylene radicals possessing apparent mobility, adsorb at surface defects. In a similar manner, dissociative adsorption is also reported for 1,3,5-tris(4-bromophenyl)benzene (App. A Fig. 9) on the Cu(111) and Ag(110) surfaces.^{19, 20} Given the apparent mobility of the ZnTBrThP molecules, the presence of chemisorbed bromine atoms arising from a spontaneous dissociative step are ostensibly absent from the imaged terraces which might be expected to be decorated to a large extent. Therefore, it is considered more plausible that the substrate protrusions observed at the molecular periphery arise from the interaction of the initially intact molecules. This conclusion is supported, as discussed below, by the apparent abstraction and subsequent incorporation of substrate atoms between the assembled ZnTBrThP molecules.

Linked together end-on through adjacent bromothienyl groups, the ZnTBrThP molecules form molecular chains, which are stable under the given imaging conditions. Close examination of the chains presented in Fig. 4.2(b), reveals a molecular pair (in the

sequence A-B) for which the apparent linkage occurs through only two bromothienyl groups. This is evidenced in Figure 4.2(c), which shows a corresponding height profile of three molecules in sequence, taken along the line of the separated and linked bromothienyl groups. Between the linked pair (dotted arrows), a surface protrusion of approximately ~ 2 Å in width is observed, whilst no such feature is found amid the separated groups. It is noted that the apparent height of the separated bromothienyl groups is much larger than those linked by the surface protrusion, indicating that the substrate strongly influences the latter. Therefore, by the apparent incorporation of the Ag(111) substrate atoms, the ZnTBrThP molecules link together. Accordingly, the molecular chain formation is tentatively attributed to metal-directed polymerisation, whereby, the ZnTBrThP molecules coordinate to Ag atoms of the substrate through the bromothienyl groups. Here it is noted that the XPS spectra obtained from the deposited ZnTBrThP overlayer (see below), reveal a charge transfer between the Ag(111) surface and bromothienyl groups consistent with covalent bonding. Similar metal-directed assembly of coordination polymers has previously been reported for pyridine-substituted porphyrins (Appendix A, Figure 10) on both the Ag- and Cu- (111) surfaces whereby coordination to intrinsic and coevaporated (Cu) adatoms takes place via the pyridine end-groups.²¹ For ZnTBrThP molecules adsorbed at the step edge, the principal molecular axis (here defined along the line of the upward bent pyrrole groups) is found to be aligned parallel to the step direction. In this configuration, oligomer chains that extend the length of the substrate step are formed, reaching tens of nanometres in length.

A large scale occupied state STM image of the ZnTBrThP molecules at a coverage of ~ 0.7 ML on the Ag(111) surface is shown in Figure 4.3(a). On the terraces single-strand chains (solid arrow) typically reach several molecules in extent; at points of intersection branched chains are formed. Displaying an apparently random distribution, enclosed oligomer loops several nanometres in size are observed. Characteristic of these loops (dashed arrow) is a uniform reduction in the apparent height of both the constituent molecules and the enclosed surface. This is evidenced in Figure 4.3(b) which shows a height profile taken across a molecule of the indicated loop. It is found that the depth of the enclosed surface (~ 2.3 Å) is equivalent to the mono-atomic step height of the Ag(111) surface.²² The molecular decoration of the lower boundary edges ostensibly gives rise to the

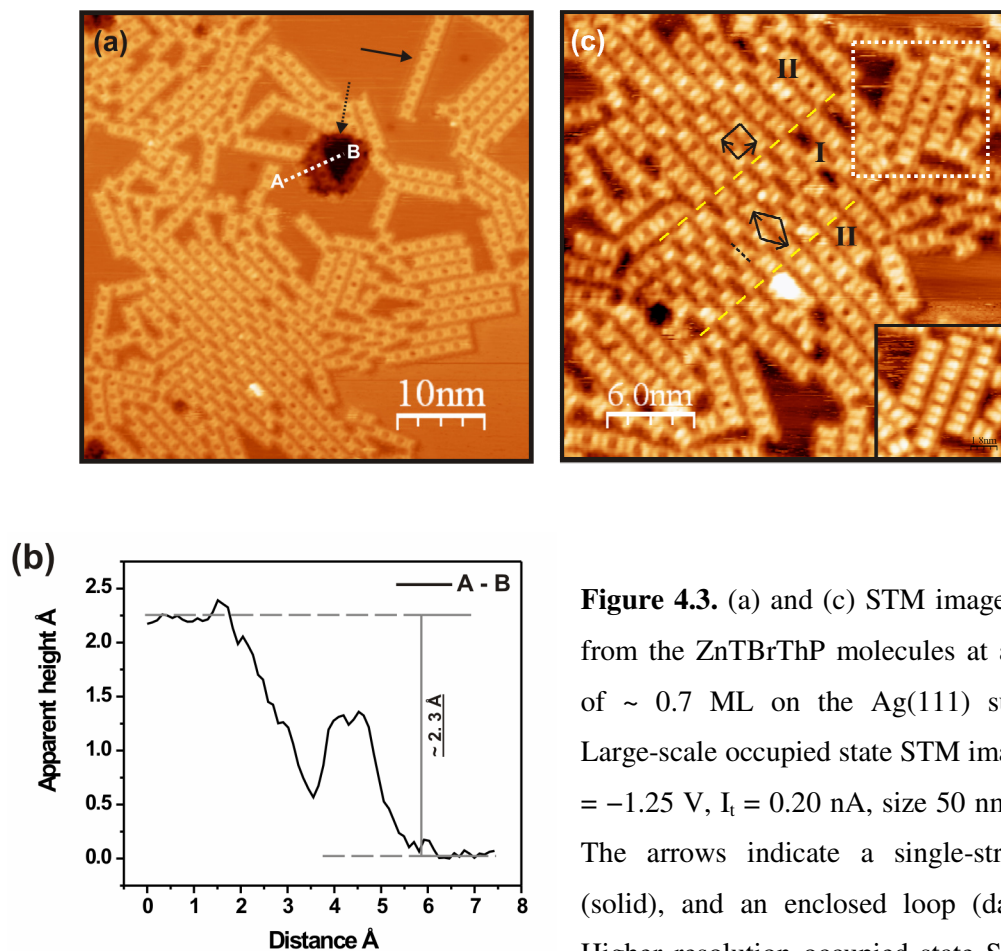


Figure 4.3. (a) and (c) STM images obtained from the ZnTBrThP molecules at a coverage of ~ 0.7 ML on the Ag(111) surface. (a) Large-scale occupied state STM image; $V_{\text{sample}} = -1.25$ V, $I_t = 0.20$ nA, size 50 nm \times 50 nm. The arrows indicate a single-strand chain (solid), and an enclosed loop (dashed). (c) Higher resolution occupied state STM image

(lower surface region shown in (a)); $V_{\text{sample}} = -1.25$ V, $I_t = 0.20$ nA, size 15 nm \times 15 nm. The dashed yellow lines mark domain boundaries. The indicated domains show the hexagonal (I) and square (II) phases; the unit cell and primitive lattice vectors are shown in black; the principal molecular axis is indicated by the dotted line. The inset shows the corresponding unoccupied state STM image of the region highlighted by the white dotted box; $V_{\text{sample}} = 1.25$ V, $I_t = 0.20$ nA, size 4.5 nm \times 4.5 nm. (b) Height profile (dotted line A – B) taken across a molecule adsorbed at the lower edge of the substrate vacancy island shown in (a).

formation of the oligomer loop. It then follows that the enclosed surface represents a substrate vacancy island. Such vacancy islands have previously been reported for the first layer of thiophene on the Au(111) surface,²³ and similarly for alkanethiol (App. A, Fig. 8) monolayers on Ag(111)²⁴. In the latter case, the formation of vacancy islands was attributed to a coordination of the substrate atoms by the sulphur moiety of the thiol end- groups. A recent study of the adsorption of Cu-porphyrin on the Cu(110) reported the capture of

substrate adatoms between assembled molecules.⁷ Significantly, the distribution of these captured adatoms holds a striking similarity to the substrate protrusions observed at the periphery of the ZnTBrThP molecules. Accordingly, it is tentatively proposed that Ag(111) substrate atoms are abstracted by the adsorbed ZnTBrThP molecules, thereby mediating the growth of the molecular assembly.

Although the ZnTBrThP molecules possess four potential coordination sites in the form of the bromothieryl substituents, they behave ditopically in the formation of single-strand chains. Figure 4.3(c) presents at higher resolution occupied (main) and unoccupied (inset) state STM images of the lower surface region displayed in Fig. 4.3(a). Here the individual tetratopic ZnTBrThP molecules display crosslinking which produces a hexagonal array of short range order (domain I); the lengths of the primitive lattice vectors (b_1 and b_2) are equal to 1.9 ± 0.1 nm, while the subtended angle is $120 \pm 2^\circ$. Within a single domain, the principal molecular axis of the individual molecules show parallel alignment, with an azimuthal rotation of $\pm 30 \pm 2^\circ$ relative to the primitive lattice vectors of the overlayer unit cell. A parallel alignment of single-strand chains is also observed, which gives rise to an ordered phase described by a square unit cell (domain II) with side lengths of 1.7 ± 0.1 nm, and subtended angle of $90 \pm 2^\circ$.

In both the occupied and unoccupied state STM images of the ZnTBrThP molecules (Fig. 4.3(c)), the apparent height of the porphyrin macrocycle exhibits a pronounced two-fold rotational symmetry. This is consistent with a saddle distortion of the porphyrin macrocycle, where two opposite pyrrole groups tilt upwards and two downwards with respect to the surface plane.²⁵ By contrast, the crystallographic structure of Cu-²⁶ and Zn-²⁷ tetrathierylporphyrin reveal a planar macrocycle conformation, whereas a wave-like configuration is found for the free-base derivative²⁸. These essentially flat conformations permit dihedral angles between the thienyl and porphyrin planes of $60 - 78^\circ$, without inducing a significant macrocycle distortion.²⁸ However, the steric hindrance of a more coplanar arrangement could be expected to induce a saddled conformation. In the present case, the rectangular profile of the bromothieryl groups indicates a rotation of the thienyl groups, while the apparent saddle distortion of the porphyrin macrocycle implies a more coplanar arrangement; thus, pointing to a conformational adaptation of the ZnTBrThP molecules upon adsorption. A similar conformation, attributed to an adsorption induced

effect, is also reported for the closely related [5,10,15,20-tetrakis(4-bromophenyl) porphyrinato] (TBrPP) (App. A, Fig. 5) adsorbed on the Cu(111) surface.³

Figure 4.4(a) shows the LEED pattern obtained from approximately 0.7ML of the ZnTBrThP molecules on the Ag(111) surface. Twelve first order diffraction spots are observed which form two equivalent hexagonal patterns. Each pattern is interpreted as being that of a superposition three rotationally equivalent domains of a hexagonal lattice, which together form two mirror domains. The individual mirror domains are highlighted (Fig. 4.4(a)), with the reciprocal lattice vectors of one, given as b^*_1 and b^*_2 , with the subtended angle β^* equal to $60 \pm 3^\circ$. A comparison of the substrate LEED pattern (shown inset), with that of the overlayer, reveals their relative orientation. In this manner, the mirror plane is seen to follow the closed-packed directions of the substrate, whereby each mirror domain represents either a clockwise or counter-clockwise rotation θ of $19 \pm 3^\circ$. In turn, the overlayer lattice vectors (b^*_1, b^*_2) are found to be aligned with the $\langle \bar{3}21 \rangle$ crystallographic directions of the substrate.

The broad spot widths of the hexagonal overlayer pattern imply diffraction from ordered domains of small size. Though the predominant molecular arrangement observed in STM images (Fig. 4.3), is that of the square phase (domain II), the symmetry and implied domain size of the overlayer LEED pattern is consistent with the hexagonal phase (domain I) of short range order. Accordingly, the lattice vectors of the overlayer pattern may be expressed in terms of those of the substrate through the following transformation:

$$\begin{pmatrix} b_1 \\ b_2 \end{pmatrix} = \begin{pmatrix} 7.45 & 2.47 \\ -2.47 & 4.98 \end{pmatrix} \begin{pmatrix} a_1 \\ a_2 \end{pmatrix}$$

where the Ag(111) nearest-neighbour distance is 0.289nm. Although a commensurate registry with the substrate lattice is prevented by primitive unit cell dimensions of the overlayer, a coincident configuration is approached for the corresponding (2x2) super-cell.

A schematic representation of the corresponding hexagonal phase (in the case of the clockwise rotated domain) superimposed on the Ag(111) surface, is shown in Figure 4.4(b). The molecular motif is depicted by structural models, whereby, the principal molecular axis of individual ZnTBrThP molecules shows the observed $30 \pm 2^\circ$ azimuthal rotation relative

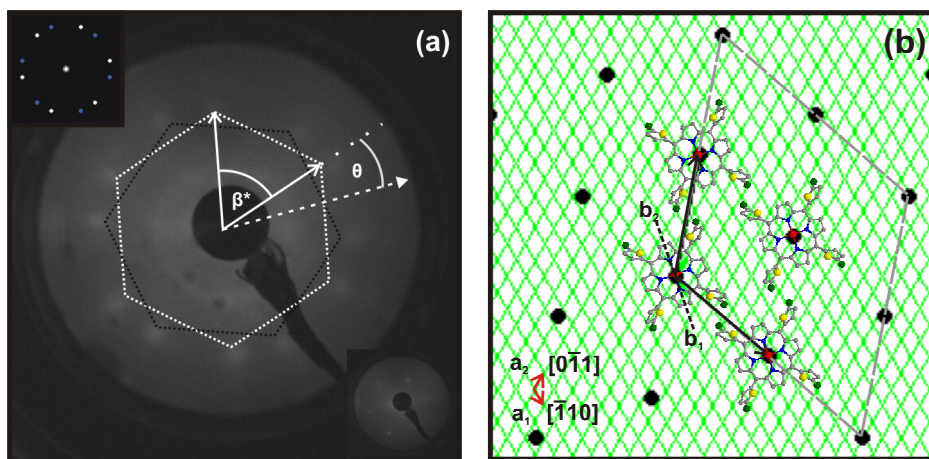


Figure 4.4. (a) LEED pattern from 0.7 ML of the ZnTBrThP molecules on the Ag(111) surface, acquired at a primary beam energy of 14.0 eV. The insets show the LEED pattern of the Ag(111) surface acquired at the higher beam energy of 112.0 eV (lower) and a simulated LEED pattern of the ZnTBrThP overlayer created using the observed lattice parameters (upper). The mirror domains of the ZnTBrThP overlayer are indicated by the black and white hexagons. The dotted line shows the close packed direction of the Ag(111) reciprocal lattice; whereby, the angle θ indicates the azimuthal rotation of the molecular overlayer. (b) Schematic representation of the azimuthal orientation of the ZnTBrThP overlayer (clockwise rotated domain) on the Ag(111) surface. The black dots represent the ZnTBrThP molecules with the points of intersection of the green mesh that of the Ag atoms. The lattice vectors of the Ag(111) surface and ZnTBrThP overlayer are labelled a_1 , a_2 and b_1 , b_2 , respectively; the dashed lines (grey) outlines the coincident overlayer super-cell.

to the primitive lattice vectors of the overlayer. Within this framework, the principal molecular axis is found to be aligned along the $\langle \bar{5} \bar{1} 4 \rangle$ crystallographic directions of the substrate, with a symmetry equivalent configuration obtained for the mirror azimuthal orientation.

As mentioned above, the metal-directed polymerisation of the ZnTBrThP molecules is found to occur through a linkage of the bromothienyl groups (Fig. 4.2(c)). It follows that the Br or S moieties (of the bromothienyl groups) will act as the functional linkers. For the surface-confined molecules, therefore, the charge state of the Br and S moieties can be expected to reflect the chemical nature of the molecular linkage. Figure 4.5 (lower) shows the Br 3p and S 2p XPS spectra obtained from ~ 1.2 ML of the ZnTBrThP molecules as

deposited on the Ag(111) surface. The Br 3p spectrum displays two principal components, with less intense shoulders apparent at higher binding energy. Taken together, the four components are assigned to a pair of Br 3p spin-orbit doublets, the fit of which yield a binding energy of 181.4 eV (principal) and 183.9 eV (minor) for the 3p_{3/2} lines, with a common spin-orbit splitting of 6.6 eV. The principal Br 3p_{3/2} line, exhibiting a binding energy comparable to that reported for AgBr (182.1 eV),²⁹ is attributed to an Ag—Br species. Shifted to higher binding energy (2.5 eV), the minor Br 3p_{3/2} line is ascribed to Br of the pristine ZnTBrThP molecule. In a similar manner, the S 2p lineshape shows an asymmetric broadening of the peak base at higher binding energy, attributed to a pair of closely spaced S 2p doublets. The resulting fit gives a binding energy of 163.0 eV (principal) and 163.7 eV (minor) for the 2p_{3/2} lines, with a shared spin-orbit splitting of 1.2 eV. Being of higher binding energy than that reported for Ag₂S (161.7 eV),³⁰ the principal S 2p_{3/2} line is attributed to an Ag—S species. Similarly, the minor S 2p_{3/2} line at still higher binding energy (0.7 eV), is assigned to S of the pristine ZnTBrThP molecule. For both the Br 3p and S 2p XPS spectra, the areas of the principal to minor components are in a ratio of ~ 1 : 0.3; hence, within the uncertainty, equivalent to the ratio of mono- to multilayers for the given (1.2 ML) surface coverage. Accordingly, the component pairs of lower and higher binding energy arise from the ZnTBrThP molecules of the surface-confined monolayer and subsequent multilayer, respectively. This conclusion is supported by the corresponding spectra acquired at a surface coverage of ~ 3.1 ML shown in Figure 5.4 (upper). Here an increase in the intensity of the higher binding energy components is observed, commensurate with the increased coverage.

The chemical shift of the Br and S core levels to lower binding energy indicates a net transfer of electron density from the Ag(111) surface to the surface-confined ZnTBrThP molecules. This agrees well with the electrophilic attraction to the lower step edges, observed at low coverage in STM images (Fig. 4.2). From the determined binding energies, both the Br and S moieties appear to form an Ag – species, consistent with the oxidative addition to substrate atoms. It is not apparent, however, whether both act independently or in concert in the linkage of the ZnTBrThP molecules.

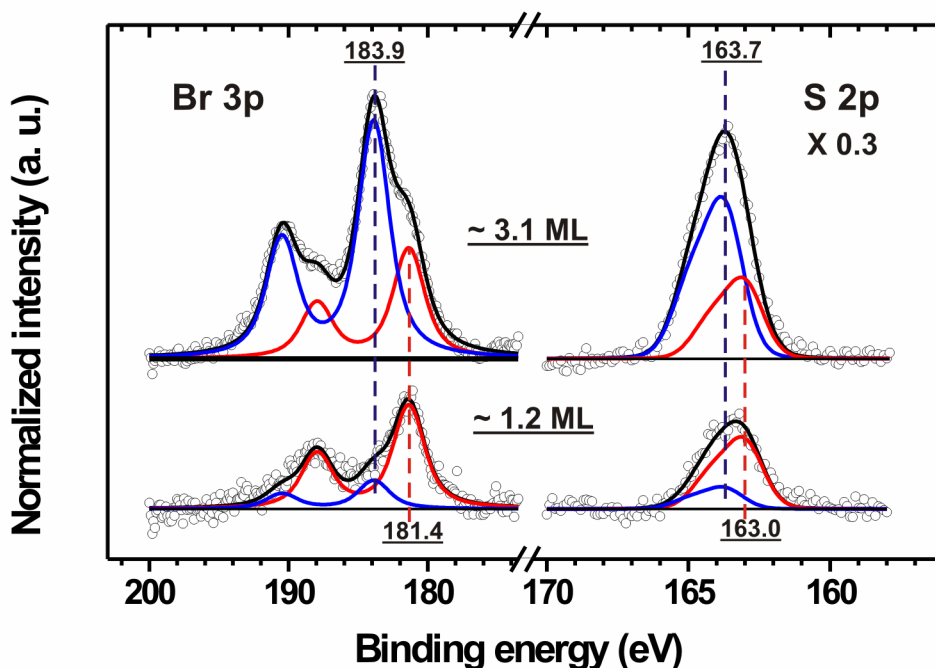


Figure 4.5. Br 3p (left) and S 2p (right) XPS spectra obtained from the ZnTBrThP overlayer on the Ag(111) surface at a coverage of 1.2 ML (lower), and 3.1 ML (upper). The circles represent the spectral data. The best fit to the spectral data is shown in black, the component peaks in colour.

4.3.2. Thermally assisted assembly: polymerisation through radical addition

The linkage between the ZnTBrThP molecules, as reflected in the core level spectra of the Br and S moieties, is found to fundamentally change upon annealing to ~ 473 K. At this temperature, a slow fragmentation of the bromothienyl groups occurs, principally resulting in the elimination of the Br atoms. From the pre-anneal spectra (Fig. 4.5), a Br/S atomic ratio of $\sim 1 : 0.9$ is obtained, consistent, within the uncertainty, with the expected stoichiometry of $1 : 1$. Figure 4.6 shows the Br 3p and S 2p XPS spectra acquired from ~ 1.2 ML of the ZnTBrThP molecules on the Ag(111) surface after annealing at 523 K for ~ 2 hrs. While the S 2p signal shows no reduction, the corresponding Br 3p signal is reduced below the noise level, reflecting the loss of the labile Br atoms from the sample surface.

Although the overall intensity of the S 2p signal shows no reduction, a marked change is observed in its lineshape. The S 2p spectrum displays two clearly resolved

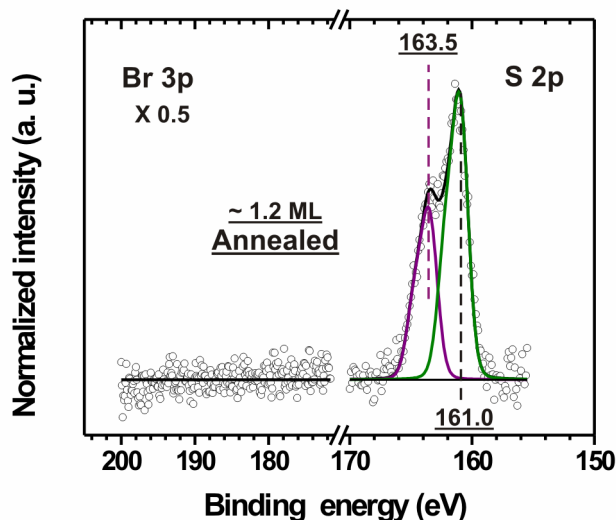


Figure 4.6. Br 3p (left) and S 2p (right) XPS spectra obtained from ~ 1.2 ML of the ZnTBrThP molecules on the Ag(111) surface, after annealing to 523 K. The circles represent the spectral data. The best fit to the spectral data is shown in black, the component peaks in colour.

doublets with relative intensities in a ratio of $\sim 2 : 3$, the larger of which lies at lower binding energy. The resulting fit yields a binding energy of 161.0 eV (principal) and 163.5 eV (minor) for the $2p_{3/2}$ lines, with a common spin-orbit splitting of 1.2 eV. The minor S $2p_{3/2}$ line is found to display a binding energy comparable to that attributed to S in the surface-decoupled multilayer. However, based on the pre-anneal surface coverage the observed S 2p signal clearly arises (at least in part) from the surface-confined monolayer. For an upward orientation of the S moiety relative to the Ag(111) surface a chemical environment similar to that of a second layer molecule might be expected.³¹ Therefore it is plausible that the minor line reflects a species with an upward orientation of the S moiety. The principal S $2p_{3/2}$ line, displaying a binding energy comparable to that reported for Ag_2S (161.7),³⁰ is thus attributed to an $\text{Ag}_2\text{—S}$ species.

Due to the fragmentation of the bromothieryl groups, the ZnThBrThP molecules are found to cleave from the lower step edges. Figure 4.7(a) shows an occupied state STM image of the ZnTBrThP molecules at a coverage of ~ 0.1 ML on the Ag(111) surface, after annealing at 523 K for 2 hrs. Although molecular clusters form on the adjacent terrace, the lower step edges remain decorated by periodic protrusions. The individual protrusions are seen to occur in pairs (as shown inset), displaying an intra- and inter-pair distance of ~ 5 and 9 \AA , respectively. A corresponding height profile of the step edge (line A-B), is shown in Figure 4.7(b). This structure closely resembles that reported for thiophene on the Au(111) surface,²³ where molecules are observed in paired rows, with an intra- and inter-

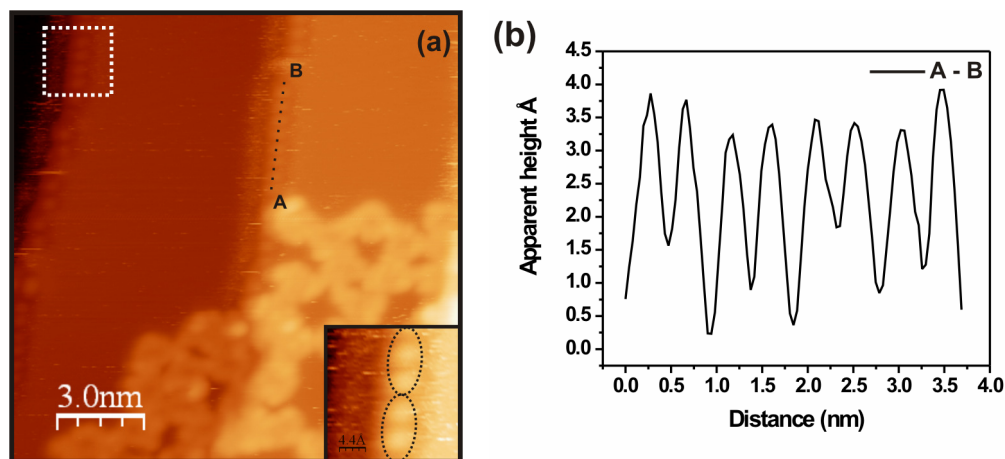


Figure 4.7. (a) Occupied STM image obtained from the ZnTBrThP molecules at a coverage of ~ 0.1 ML on the Ag(111) surface, subsequent to annealing at 573 K for 2hrs; $V_{\text{sample}} = -1.25$ V, $I_t = 0.20$ nA, size 15 nm \times 15 nm. The inset shows an enlarged view of the step edge highlighted by the white dotted box; pairs of protrusions are outlined. (b) Height profile of the step edge taken along the (dotted) line A – B.

pair distance of 4.4 and 8.8 Å, respectively. In the absence of the terminal Br atoms (Fig. 4.6), it follows that the protrusions at the lower step edges are thienyl residues (thiophene radicals), arising from the fragmentation of the bromothienyl groups. These step-bound thienyl residues, therefore, can be associated with the Ag_2S species observed in the S 2p XPS spectra (Fig. 4.6), and hence, with the higher intensity of the corresponding photoemission line.

The fragmentation pattern of the ZnTBrThP molecules produces an array of distinct radical species which covalently couple on the terrace surface. The divergent linkage which results, leads to the formation of an irregular polymer network. This is illustrated in Figure 4.8, which shows an occupied state STM image of the ZnTBrThP molecules at a coverage of ~ 0.7 ML subsequent to the above annealing conditions; the inserts (unoccupied state images) show enlarged views of the elementary structural motifs. While the dissociation of the four terminal Br atoms yields the tetra-(thienyl)porphyrin derivative, the loss of the meso-thienyl groups gives rise to yet further network elements. From the fragmentation pattern observed in STM images (Fig. 4.8), the di- and tetra- (thienyl)porphyrin derivatives (inserts 1 and 2, respectively) are found to predominate. It is noted that the apparent core

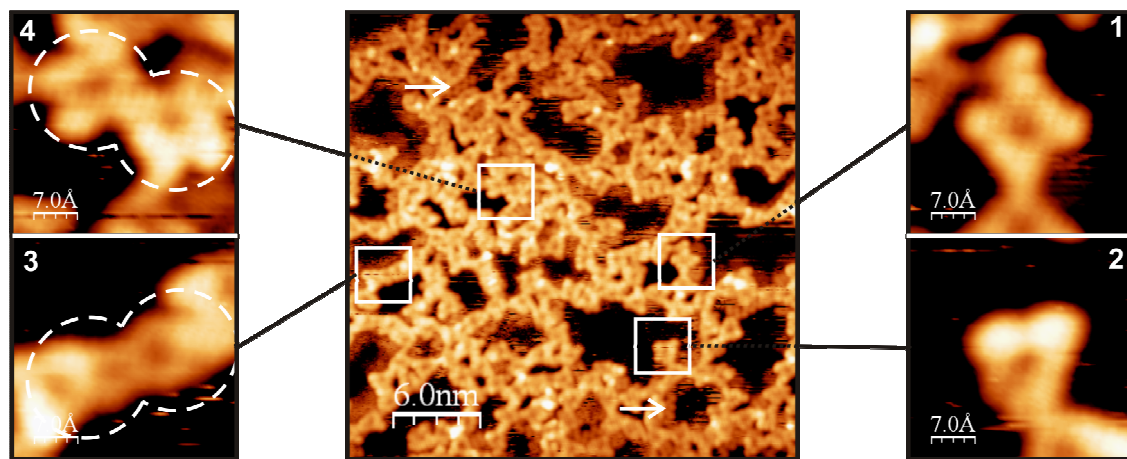


Figure 4.8. STM images obtained from the ZnTBrThP molecules at a coverage of ~ 0.7 ML on the Ag(111) surface, subsequent to annealing at 573 K for 2hrs. (main) Occupied state STM image; $V_{\text{sample}} = -1.25$ V, $I_t = 0.20$ nA, size 30 nm \times 30 nm. (inserts) Unoccupied state STM images; $V_{\text{sample}} = 1.20$ V, $I_t = 0.25$ nA, size 2.5 nm \times 2.5 nm.

depression does not reflect demetallation of the porphyrin complex, but rather a feature of the applied tunnelling bias-voltage. The different derivatives form distinct tetratopic linkers that can couple in various combinations. Despite the multiplicity of structural motifs, the principal linkages can be attributed to covalent coupling at either the meso-bridge carbons (insert 3), or α carbons of the meso-thienyl groups (insert 4).

As a consequence of the observed irregular linkage, cavities are formed within the polymer network. Along the edges of these cavities are found “strings” of protrusions, which are tentatively ascribed to thienyl residues; examples of which are indicated (arrows) in Fig. 4.8. It follows that the cleavage of the meso-thienyl groups is not limited to the step-bound ZnTBrThP molecules, but can occur also on the terrace of the Ag(111) surface. Accordingly, the network reflects a two-dimensional polymer matrix, comprising of chemisorbed thienyl residues and covalently coupled (thienyl)porphyrins.

4.3.3. Self-assembly on the Au(111)-(22 × √3) surface: reconstruction dependant adsorption

At low coverages, the deposited ZnTBrThP molecules preferentially adsorb over the fcc regions of the Au(111)-(22 × √3) surface. Figure 4.9(a) shows a typical occupied state STM image of the ZnTBrThP molecules at a coverage of ~ 0.3 ML; an individual molecule is highlighted in the enlarged view shown inset. On the uncovered areas of the substrate, the corrugation lines separating the different stacking regions of surface reconstruction are just faintly visible. Within the wider fcc regions the ZnTBrThP molecules are observed to self-assemble, while the narrower hcp regions remain bare; individual molecules are not observed in isolation. A preferential adsorption over the fcc regions of the reconstructed Au(111) surface has frequently been reported for various aromatic molecules.³²⁻³⁵ A notable example is that of azobenzene,³⁶ since, for the closely related 3,3,5,5-tetra-*tert*-butylazobenzene (*meta*-TBA) molecules (Appendix A, Figure 11) no such affinity for the different stacking regions is reported³⁷. The distinct difference between the molecule-substrate interactions of azobenzene and its *tert*-butyl derivative is that in the latter case the *tert*-butyl-groups are found to inhibit the mixing of the azobenzene's π orbitals with the Au(111) substrate.³⁷ Hence, it is *speculated* that a coupling of the molecular π system to the substrate, specifically over the fcc regions of the reconstruction, stabilizes the self-assembly of the ZnTBrThP molecules at low coverage.

On the Ag(111) substrate, the ZnTBrThP molecules are found to uniformly adsorb at the lower step edges (Sec. 4.3.1). In like manner, a distinct affinity for the lower step edges of the Au(111)-(22 × √3) surface is observed. However, as on terraces, adsorption at the step edges occurs almost exclusively at fcc sites. Figure 4.9(b) shows an occupied state STM image of the ZnTBrThP molecules (taken at the above coverage), in which step-edge adsorption is observed; here, the surface reconstruction adjacent to the lower step edges takes on two distinct forms. For the fcc domain aligned parallel to the lower step (left), adsorption along the entire length of the lower edge is observed. However, where the reconstruction passes across the surface step (right), the adjoining fcc sites (white arrows) are found to be occupied, whereas those of the hcp (black arrows) are not. Away from the step edges on the terraces of the Au(111)-(22 × √3) surface, it is the transition regions,

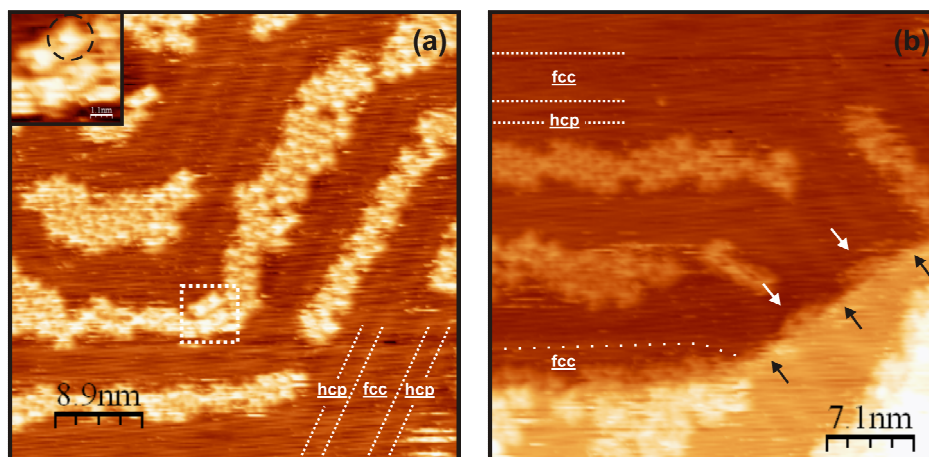


Figure 4.9. STM images obtained from the ZnTBrThP molecules at a coverage of ~ 0.3 ML on the Au(111)- $(22 \times \sqrt{3})$ surface. (a) Occupied state STM image; $V_{\text{sample}} = -1.0$ V, $I_t = 0.20$ nA, size 45 nm \times 45 nm. The inset shows an enlarged view of the region highlighted by the white dotted box; an individual ZnTBrThP molecule is circled. (b) Occupied state STM image; $V_{\text{sample}} = -1.0$ V, $I_t = 0.20$ nA, size 30 nm \times 30 nm. The white and black arrows indicate regions of the lower step edge that are decorated (fcc) and bare (hcp) of the ZnTBrThP molecules, respectively.

marked by the corrugation lines, which are found with increasing coverage (see below) to be last occupied. Therefore, the apparent lower affinity for the step edge hcp sites may be representative of the transition region that exists between the (hcp) stacking of the topmost Au atoms of the lower terrace, and the bulk-like (fcc) second layer of the upper terrace.³⁸

The self-assembly of the ZnTBrThP molecules over the fcc regions of the Au(111)- $(22 \times \sqrt{3})$ surface is followed at higher coverage by the hcp and transition regions. Figure 4.10(a) shows typical occupied (main) and unoccupied (inset) state STM images of the highly ordered structure formed at monolayer coverage; an individual molecule is highlighted in the enlarged view shown inset. The self-assembled ZnTBrThP lattice is described by a rectangular unit cell; the lengths of the primitive lattice vectors b_1 and b_2 are equal to 1.58 and 1.59 ± 0.05 nm, respectively, while the subtended angle is $90 \pm 2^\circ$. A very similar lattice structure is also reported for the closely related Ni-TBrPP molecules (see App. A, Fig. 5) on the reconstructed Au(111) surface,² while for the tetraphenylporphyrin derivative,³⁹ a quadrilateral arrangement with a reduced lattice constant (~ 2 Å) reflective of the absence of the terminal Br moieties is found. Although the variation in the aryl-

bromo groups does not significantly influence the respective unit cell dimensions, a pronounced effect on the associate aryl-aryl geometries is observed. For a single domain, the principal molecular axes of the individual ZnTBrThP molecules are found to be in parallel alignment, and together show an azimuthal rotation of $\pm 30 \pm 2^\circ$ relative to the primitive lattice vectors of the overlayer unit cell. In this configuration, the bromothieryl groups of adjacent molecules align face-to-face, in the so-called parallel stacked geometry known for benzene dimers.⁴⁰ As mentioned above, this is markedly different to the edge-to-face “T-shaped” geometry apparent in the reported *STM images* of Ni-TBrPP on the reconstructed Au(111) surface.² The edge-to-face geometry of benzene dimers is known to be largely determined by electrostatic quadrupole interactions.⁴⁰ It follows that the edge-to-face configuration of the bromophenyl groups (of adjacent Ni-TBrPP molecules) is similarly determined. While a face-to-face alignment of benzene dimers yields a geometry unfavorable to quadrupole interactions, a stabilization can be achieved where one face is electron rich, and the other deficient.⁴⁰ 2-halothiophenes are known to possess a dipole moment where the negative and positive ends of the dipole are localized at the sulphur and halogen moieties, respectively.⁹ In the present case, therefore, it is proposed that the face-to-face alignment of the bromothieryl groups is stabilized by attractive dipole-dipole interactions between S and Br moieties of adjacent ZnTBrThP molecules.

The bright and faint protrusions associated with the bromothieryl groups (Fig. 4.10(a): arrows 3 and 4 respectively) are attributed to the thienyl and Br moieties, respectively. From the positions of the Br moieties, pair distances of ~ 1.2 and 1.5 \AA are obtained. This suggests a less co-planar configuration of the bromothieryl and porphyrin planes, when compared to the conformation adopted by the ZnTBrThP molecules on the Ag(111) surface. Notably, in the unoccupied state *STM image* (inset), the apparent height of the pyrrole groups (arrow 2) shows a clear four-fold rotational symmetry. In turn, this may be associated with a more planar conformation of the porphyrin macrocycle, reflective of a reduced steric hindrance of the bromothieryl groups. Between the occupied (main) and unoccupied (inset) state *STM images*, a pronounced difference in the apparent height at the porphyrin core is observed; namely, a protrusion is displayed in the former, a depression in the latter (arrow 1). It is noted that a similar bias-voltage dependence is visible in the *STM images* of the ZnTBrThP molecules on the Ag(111) surface (Fig. 4.3(c)), despite being less

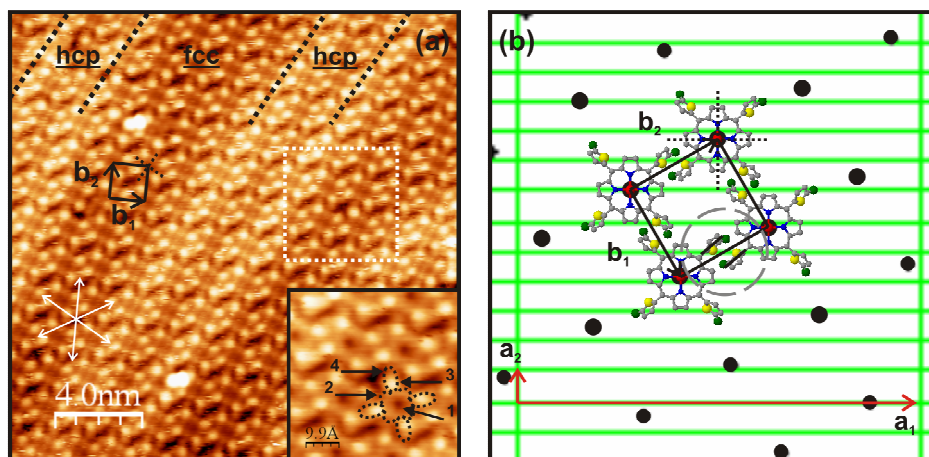


Figure 4.10. (a) STM images obtained from the ZnTBrThP molecules at a coverage of ~ 1.0 ML on the Au(111)- $(22 \times \sqrt{3})$ surface. The close-packed directions of the Au(111)- $(22 \times \sqrt{3})$ surface are indicated by white arrows. The unit cell and primitive lattice vectors (b_1 , b_2) of the molecular overlayer are shown in black; the principal molecular axes are indicated by the dotted lines. (main) Occupied state STM image; $V_{\text{sample}} = -1.25$ V, $I_t = 0.20$ nA, size 20 nm \times 20 nm. (inset) Corresponding unoccupied state STM image (enlarged view) of the region highlighted by the white dotted box; $V_{\text{sample}} = 1.25$ V, $I_t = 0.20$ nA, size 5 nm \times 5 nm. The porphyrin core, macrocycle, thienyl and Br moieties are number 1 to 4, respectively. (b) Schematic representation of the azimuthal orientation of the ZnTBrThP overlayer (clockwise rotated domain) on the Au(111)- $(22 \times \sqrt{3})$ surface. The black dots represent the ZnTBrThP overlayer lattice with the points of intersection of the green mesh that of the Au substrate. The lattice vectors of the Au(111)- $(22 \times \sqrt{3})$ surface and ZnTBrThP overlayer are labelled a_1 , a_2 and b_1 , b_2 , respectively. The “parallel stacked” configuration of a pair adjacent bromothieryl groups is indicated by the dashed circled.

well resolved. Several previous studies of metallotetrapyrroles have proposed that the d-orbital contribution (of the central metal atom) near the Fermi level strongly influences the apparent core height in tunnelling images.⁴¹⁻⁴⁴ For the presented STM images, it follows that the d-orbital contribution (of the central Zn atom) to the tunnelling current is larger (1.25 eV) below the Fermi level, than above.

In the STM images of the molecular overlayer (Fig. 4.10(a)), the vertical corrugation of the underlying Au(111)- $(22 \times \sqrt{3})$ surface reconstruction is observed. The superimposed reconstruction pattern is marked by a pair-wise arrangement of parallel lines, which lie perpendicular to the contraction direction of the topmost Au atoms. Since these

parallel corrugation lines are known follow the $\langle 1\bar{2}1 \rangle$ crystallographic directions of the substrate,³⁸ the orientation of the molecular overlayer relative Au(111)-(22 × √3) surface may be determined. To this end, it is found that the principal lattice vector (b_1) of the overlayer is azimuthally rotated by $61 \pm 2^\circ$ relative to the direction of the parallel corrugation lines. Thus, the overlayer lattice vectors b_1 and b_2 are aligned respectively along the $\langle \bar{1}12 \rangle$ and $\langle \bar{1}10 \rangle$ crystallographic directions of the substrate. Accordingly, the primitive lattice vectors of the molecular overlayer may be expressed in terms of those of the substrate through the following transformation:

$$\begin{pmatrix} b_1 \\ b_2 \end{pmatrix} = \begin{pmatrix} 0.125 & -2.91 \\ 0.219 & 1.69 \end{pmatrix} \begin{pmatrix} a_1 \\ a_2 \end{pmatrix}$$

where a_1 and a_2 subtend an angle of 90° , and have magnitudes of 6.3 and 0.47 nm respectively.³⁸ Despite the apparent epitaxial relationship, the determined transform indicates an incommensurate registry of the molecular overlayer and substrate lattices.

In a similar manner, the azimuthal orientation of the individual molecules may be determined. Figure 4.10(b) shows a schematic representation (for a single rotational domain) of the molecular overlayer superimposed on the Au(111)-(22 × √3) surface; here, the molecular motif is depicted by structural models. The principal molecular axes of the individual molecules show the observed $30 \pm 2^\circ$ azimuthal rotation relative to the primitive lattice vectors of the overlayer. In this arrangement, one of the molecular axes is aligned with the $\langle \bar{1}01 \rangle$ close-packed directions of the substrate, the other follows the $\langle 1\bar{2}1 \rangle$ crystallographic directions. Here it is noted that a clear LEED pattern from the molecular overlayer could not be obtained, precluding a corresponding analysis as carried out for the ZnTBrThP molecules on the Ag(111) surface.

For the surface-confined monolayer distinct charge states of the Br moiety are found, consistent with a variation of chemical reactivity across the reconstructed Au(111) surface. Figure 4.11 (lower) shows the Br 3p and S 2p XPS spectra obtained from ~ 1.0 ML of the ZnTBrThP molecules as deposited on the Au(111)-(22 × √3) surface. The Br 3p spectrum displays a pair of Br 3p spin-orbit doublets; the principal and minor doublets, at

higher and lower binding energy, correspond to $\sim 74\%$ and 26% of the total envelope (peak) area, respectively. The resulting fit yields a binding energy of 183.4 eV (principal) and 181.0 eV (minor) for the $3p_{3/2}$ lines, with a common spin-orbit splitting of 6.6 eV. As such, the Br 3p spectrum reveals two distinct chemical environments of the terminal Br atoms. The corresponding STM images (Fig. 4.10(a)), however, show no change in the appearance of the bromothienyl groups across the surface - aside from the superimposed vertical corrugation. The inference, therefore, is that the chemical environment of the Br moiety varies with the different stacking regions of the underlying surface reconstruction. Accordingly, the relative areas of the Br 3p doublets should reflect those of the individual stacking regions or a combination thereof. As previously determined from STM images,⁴⁵ the fcc, transition and hcp stacking regions, respectively, are found to occupy 34 %, 44 % and 22 % of the reconstructed surface area. It follows that the minor Br 3p doublet, within the uncertainty, represents ZnTBrThP molecules adsorbed over the hcp regions. In turn, the principal Br 3p doublet may be attributed to a common molecular adsorption over the fcc and transition regions. The S 2p spectrum, shown by way of comparison, displays a single peak, assigned to an S 2p spin-orbit doublet. The resulting fit gives a binding energy of 163.3 eV for the $2p_{3/2}$ line, and a spin-orbit splitting of 1.2 eV. It then follows that the sulphur mediated component of the molecule-substrate interaction is similar for the different stacking regions of the surface reconstruction.

As evidenced by the Br 3p XPS spectra (Fig. 4.11), a Au—Br species is likely formed at the bromothienyl groups of ZnTBrThP molecules adsorbed over the hcp stacking regions. The associated binding energy of the Br $3p_{3/2}$ line (181.0 eV), is comparable to that of the Ag—Br species (181.4 eV) formed by the ZnTBrThP molecules on the Ag(111) surface, and so reflects a similar charge state of the Br moiety. For molecules adsorbed over the adjacent fcc (and transition) regions, the binding energy of the corresponding Br $3p_{3/2}$ line (183.4 eV) indicates a less reduced charge state. It has been previously shown that the surface-state electrons of the reconstructed Au(111) surface experience a weakly attractive potential (~ 25 meV) in the hcp regions of the reconstruction.⁴⁶ This was revealed by a greater affinity for low energy electrons (0.48 eV) to localize in the hcp regions compared to the fcc and transition regions.⁴⁶ Therefore, the formation of an apparent Au—Br species exclusively at hcp regions, may be attributed to the differences in the local density of states

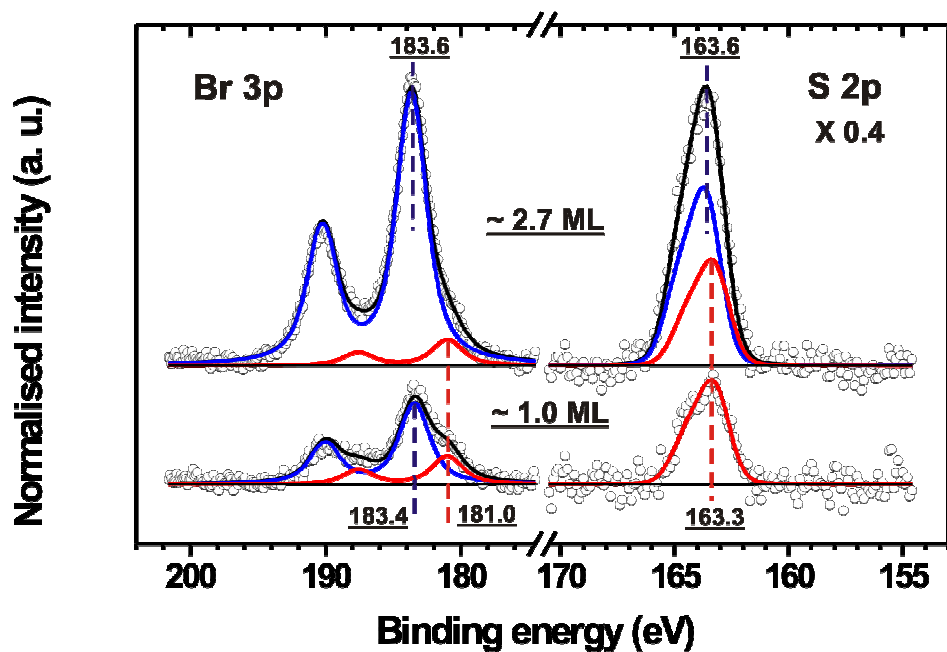


Figure 4.11. Br 3p (left) and S 2p (right) XPS spectra obtained from the ZnTBrThP overlayer on the Au(111)-(22 × $\sqrt{3}$) surface at a coverage of ~ 1.0 ML (lower), and ~ 2.7 ML (upper). The circles represent the spectral data. The best fit to the spectral data is shown in black, the component peaks in colour.

across the reconstructed Au(111) surface.

The corresponding Br 3p and S 2p XPS spectra acquired at a surface coverage of ~ 2.7 ML are shown Figure 4.11 (upper). Relative to the S 2p_{3/2} and principal Br 3p_{3/2} lines, the fit of the corresponding multilayer doublet yields a shift to higher binding energy of 0.3 ± 0.2 and 0.2 ± 0.1 eV, respectively. This apparent change of chemical environment of the surface-decoupled multilayer implies that the molecule-substrate interaction, across the reconstructed Au(111) surface, is mediated by both the Br and S moieties of the bromothieryl groups.

4.3.4. Thermally assisted assembly: radical-radical addition

Adsorbed on the Au(111)-(22 × √3) surface, the ZnTBrThP molecules display a thermal lability that results in the dissociation of the terminal Br atoms. The onset of Br loss, as reflected in the Br 3p photoemission intensity, is found to occur at ~ 473 K. This is approximately the same temperature at which fragmentation of the bromothieryl groups takes place on the Ag(111) surface. The thermal lability of the ZnTBrThP molecules on the Au(111)-(22 × √3) surface, however, is markedly different. Figure 4.12(a) shows the Br 3p and S 2p XPS spectra acquired from ~ 1.0 ML of the ZnTBrThP molecules on the Au(111)-(22 × √3) surface after annealing at 523 K for ~ 2 hrs. Here, as on the Ag(111) surface, the Br signal is found to be reduced below the noise level, while the overall intensity of the corresponding S 2p signal remains unchanged. The S 2p lineshape, however, does not change, in direct contrast to that found on the Ag(111) surface. It follows that the thienyl groups arising from the dissociation of the terminal Br atoms, remain bound at the meso-position of the porphyrin macrocycle.

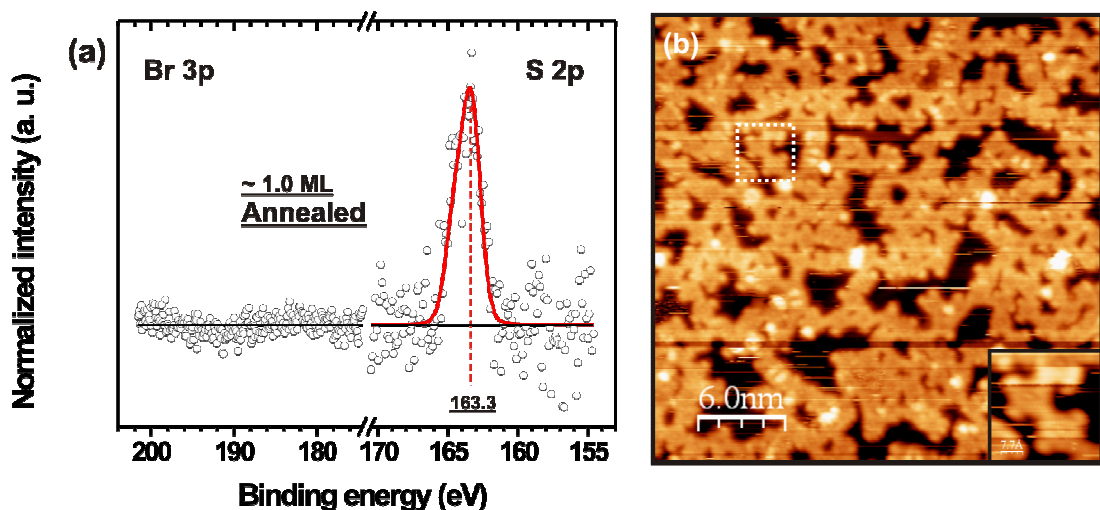


Figure 4.12. (a) Br 3p (left) and S 2p (right) XPS spectra obtained from ~ 1.0 ML of the ZnTBrThP molecules on the Au(111)-(22 × √3) surface, after annealing to 523 K. The circles represent the spectral data. The best fit to the spectral data is shown in black, the component peaks in colour. (b) STM images obtained from the ZnTBrThP molecules at a coverage of ~ 1.0 ML on the Au(111)-(22 × √3) surface, subsequent to annealing at 573 K for 2hrs; $V_{\text{sample}} = -1.20$ V, $I_t = 0.25$ nA, size 30 nm × 30 nm. The inset shows an enlarged view region highlighted by the white dotted box.

At the loss of the terminal Br atoms, the resulting tetra-(thienyl)porphyrin derivatives covalently couple on the terrace surface. These molecular radical species follow a divergent linkage pattern which leads to the formation of an irregular polymer network. Figure 4.12(b) shows an occupied state STM image of the ZnTBrThP molecules at a coverage of ~ 1.0 ML, subsequent to the above annealing conditions; an enlarged view of the elementary structural motif is shown inset. The individual network elements display four terminal protrusions which, in the absence of the Br atoms, may be assigned to the meso-thienyl groups; thus, confirming the above interpretation of the S 2p lineshape. Although the individual network elements do not link in a regular pattern, the principal structural motif (shown inset) may be attributed to covalent coupling at the α carbons of the meso-thienyl groups. On the Au(111)-($22 \times \sqrt{3}$) surface, therefore, the positions of covalent linkage are determined by the substitution pattern of the Br atoms. Several recent studies of aryl-halide substituted porphyrins (adsorbed on the reconstructed Au(111) surface) have reported radical-radical addition which is similarly predetermined by the halogen substitution pattern.^{1, 2, 4}

4.4. Summary

The organisation and thermal lability of ZnTBrThP molecules on the Ag(111) and Au(111)-($22 \times \sqrt{3}$) surfaces have been investigated using STM, LEED and XPS. The ZnTBrThP molecules are found to self-assemble at room temperature on both surfaces, whereby, the average plane of the porphyrin macrocycle lies parallel to that of the substrate. On the Ag(111) surface, the ZnTBrThP molecules are found to link together end-on through adjacent bromothienyl groups, forming single strand chains and crosslinked coordination networks; the coordination of Ag-substrate atoms is manifest in the emergence of periodic surface protrusions between and surrounding individual molecules. On the Au(111)-($22 \times \sqrt{3}$) surface, a highly ordered lattice is formed in which adjacent bromothienyl groups of the ZnTBrThP molecules assume a distinct parallel face-to-face alignment. When adsorbed on both surfaces, the ZnTBrThP molecules display a latent thermal lability, resulting in the fragmentation of the bromothienyl groups at ~ 423 K. The

di- and tetra- (thienyl)porphyrin derivatives are found to predominate on the Ag(111) surface, while the latter is exclusively observed on Au(111)-(22 × √3). At the thermally induced fragmentation of the bromothienyl groups, the resultant (thienyl)-porphyrin derivatives covalently couple, leading to the formation of irregular polymer networks.

4.5. References

- (1) Grill, L.; Dyer, M.; Lafferentz, L.; Persson, M.; Peters, M. V.; Hecht, S. Nano-architectures by covalent assembly of molecular building blocks. *Nat. Nanotechnol.* **2007**, *2*, 687-691.
- (2) Krasnikov, S. A.; Doyle, C. M.; Sergeeva, N. N.; Preobrajenski, A. B.; Vinogradov, N. A.; Sergeeva, Y. N.; Zakharov, A. A.; Senge, M. O.; Cafolla, A. A. Formation of extended covalently bonded Ni porphyrin networks on the Au(111) surface. *Nano Res.* **2011**, *4*, 376-384.
- (3) Doyle, C. M.; Krasnikov, S. A.; Sergeeva, N. N.; Preobrajenski, A. B.; Vinogradov, N. A.; Sergeeva, Y. N.; Senge, M. O.; Cafolla, A. A. Evidence for the formation of an intermediate complex in the direct metalation of tetra(4-bromophenyl)-porphyrin on the Cu(111) surface. *Chem. Commun.* **2011**, *47*, 12134-12136.
- (4) Lafferentz, L.; Eberhardt, V.; Dri, C.; Africh, C.; Comelli, G.; Esch, F.; Hecht, S.; Grill, L. Controlling on-surface polymerization by hierarchical and substrate-directed growth. *Nature Chem.* **2012**, *4*, 215-220.
- (5) Veld, M. I.; Iavicoli, P.; Haq, S.; Amabilino, D. B.; Raval, R. Unique intermolecular reaction of simple porphyrins at a metal surface gives covalent nanostructures. *Chem. Commun.* **2008**, 1536-1538.
- (6) Hanke, F.; Haq, S.; Raval, R.; Persson, M. Heat-to-connect: surface commensurability directs organometallic one-dimensional self-assembly. *ACS Nano* **2011**, *5*, 9093-9103.
- (7) Haq, S.; Hanke, F.; Dyer, M. S.; Persson, M.; Iavicoli, P.; Amabilino, D. B.; Raval, R. Clean coupling of unfunctionalized porphyrins at surfaces to give highly oriented organometallic oligomers. *J. Am. Chem. Soc.* **2011**, *133*, 12031-12039.

- (8) Lackinger, M.; Heckl, W. M. A STM perspective on covalent intermolecular coupling reactions on surfaces. *J. Phys. D: Appl. Phys.* **2011**, *44*, 464011.
- (9) Lien, E. J.; Kumler, W. D. Dipole moment and structure of thiophene derivatives and benzene analogs. *J. Pharm. Sci.* **1970**, *59*, 1685-1688.
- (10) Horcas, I.; Fernandez, R.; Gomez-Rodriguez, J. M.; Colchero, J.; Gomez-Herrero, J.; Baro, A. M. WSXM: A software for scanning probe microscopy and a tool for nanotechnology. *Rev. Sci. Instrum.* **2007**, *78*, 013705.
- (11) Adler, A. D.; Longo, F. R.; Kampas, F.; Kim, J. On preparation of metalloporphyrins. *J. Inorg. Nucl. Chem.* **1970**, *32*, 2443-2445.
- (12) Smoluchowski, R. Anisotropy of the electronic work function of metals. *Phys. Rev.* **1941**, *60*, 661-674.
- (13) Sykes, E.; Han, P.; Kandel, S.; Kelly, K.; McCarty, G.; Weiss, P. Substrate-mediated interactions and intermolecular forces between molecules adsorbed on surfaces. *Acc. Chem. Res.* **2003**, *36*, 945-953.
- (14) Han, P.; Mantooth, B.; Sykes, E.; Donhauser, Z.; Weiss, P. Benzene on Au(111) at 4 K: monolayer growth and tip-induced molecular cascades. *J. Am. Chem. Soc.* **2004**, *126*, 10787-10793.
- (15) McCarty, G.; Weiss, P. Footprints of a surface chemical reaction: Dissociative chemisorption of p-diiodobenzene on Cu(111). *J Phys Chem B* **2002**, *106*, 8005-8008.
- (16) McCarty, G.; Weiss, P. Formation and manipulation of protopolymer chains. *J. Am. Chem. Soc.* **2004**, *126*, 16772-16776.
- (17) Lipton-Duffin, J. A.; Ivasenko, O.; Perepichka, D. F.; Rosei, F. Synthesis of polyphenylene molecular wires by surface-confined polymerization. *Small* **2009**, *5*, 592-597.
- (18) Lipton-Duffin, J. A.; Miwa, J. A.; Kondratenko, M.; Cicoira, F.; Sumpter, B. G.; Meunier, V.; Perepichka, D. F.; Rosei, F. Step-by-step growth of epitaxially aligned polythiophene by surface-confined reaction. *Proc. Natl. Acad. Sci. U. S. A.* **2010**, *107*, 11200-11204.
- (19) Gutzler, R.; Walch, H.; Eder, G.; Kloft, S.; Heckl, W. M.; Lackinger, M. Surface mediated synthesis of 2D covalent organic frameworks: 1,3,5-tris(4-bromophenyl)benzene on graphite(001), Cu(111), and Ag(110). *Chem. Commun.* **2009**, 4456-4458.

- (20) Walch, H.; Gutzler, R.; Sirtl, T.; Eder, G.; Lackinger, M. Material- and orientation-dependent reactivity for heterogeneously catalyzed carbon-bromine bond homolysis. *J. Phys. Chem. C* **2010**, *114*, 12604-12609.
- (21) Heim, D.; Ecija, D.; Seutert, K.; Auwaerter, W.; Aurisicchio, C.; Fabbro, C.; Bonifazi, D.; Barth, J. V. Self-assembly of flexible one-dimensional coordination polymers on metal surfaces. *J. Am. Chem. Soc.* **2010**, *132*, 6783-6790.
- (22) Orisaka, S.; Minobe, T.; Uchihashi, T.; Sugawara, Y.; Morita, S. The atomic resolution imaging of metallic Ag(111) surface by noncontact atomic force microscope. *Appl. Surf. Sci.* **1999**, *140*, 243-246.
- (23) Noh, J.; Ito, E.; Nakajima, K.; Kim, J.; Lee, H.; Hara, M. High-resolution STM and XPS studies of thiophene self-assembled monolayers on Au(111). *J. Phys. Chem. B* **2002**, *106*, 7139-7141.
- (24) Bucher, J. P.; Santesson, L.; Kern, K. Thermal healing of self-assembled organic monolayers - hexadecanethiol and octadecanethiol on Au(111) and Ag(111). *Langmuir* **1994**, *10*, 979-983.
- (25) Rosa, A.; Ricciardi, G.; Baerends, E. J. Synergism of porphyrin-core saddling and twisting of meso-aryl substituents. *J. Phys. Chem. A* **2006**, *110*, 5180-5190.
- (26) Diskin-Posner, Y.; Balasubramanian, S.; Patra, G.; Goldberg, I. [5,10,15,20-meso-tetrakis(2-thienyl)porphyrin-ato-kappa(4) N]copper(II). *Acta Crystallogr. Sect. E. -Struct. Rep. Online* **2001**, *57*, M346-M348.
- (27) Purushothaman, B.; Varghese, B.; Bhyrappa, P. [5,10,15,20-tetrakis(2-thienyl)porphyrinato]zinc(II). *Acta Cryst.* **2001**, *57*, 252-253.
- (28) Bellizzi, M.; Foss, P.; Pelto, R.; Crundwell, G.; Bruckner, C.; Updegraff, J.; Zeller, M.; Hunter, A. Crystal structure of 5,10,15,20-tetrakis(5-methylthien-2-yl)porphyrin, C₄₀H₃₀N₄S₄. *Z. Krist. -New Cryst. Struct.* **2004**, *219*, 129-131.
- (29) Kawasaki, M.; Ishii, H. Preparation and surface characterization of Ag(111) film covered with halide monolayer. *Langmuir* **1995**, *11*, 832-841.
- (30) Wei, H.; Scudiero, L.; Eilers, H. Infrared and photoelectron spectroscopy study of vapor phase deposited poly (3-hexylthiophene). *Appl. Surf. Sci.* **2009**, *255*, 8593-8597.

- (31) Beggan, J. P.; Krasnikov, S. A.; Sergeeva, N. N.; Senge, M. O.; Cafolla, A. A. Control of the axial coordination of a surface-confined manganese(III) porphyrin complex. *Nanotechnology* **2012**, *23*, 235606.
- (32) Bohringer, M.; Morgenstern, K.; Schneider, W.; Berndt, R.; Mauri, F.; De Vita, A.; Car, R. Two-dimensional self-assembly of supramolecular clusters and chains. *Phys. Rev. Lett.* **1999**, *83*, 324-327.
- (33) Kirakosian, A.; Comstock, M.; Cho, J.; Crommie, M. Molecular commensurability with a surface reconstruction: STM study of azobenzene on Au(111). *Phys. Rev. B* **2005**, *71*, 113409.
- (34) Koslowski, B.; Tschetschetkin, A.; Maurer, N.; Mena-Osteritz, E.; Baeuerle, P.; Ziemann, P. Terthiophene on Au(111): A scanning tunneling microscopy and spectroscopy study. *Beilstein J. Nanotechnol.* **2011**, *2*, 561-568.
- (35) Cheng, Z. H.; Gao, L.; Deng, Z. T.; Jiang, N.; Liu, Q.; Shi, D. X.; Du, S. X.; Guo, H. M.; Gao, H. Adsorption behavior of iron phthalocyanine on Au(111) surface at submonolayer coverage. *J. Phys. Chem. C* **2007**, *111*, 9240-9244.
- (36) Fernandez-Torrente, I.; Monturet, S.; Franke, K. J.; Fraxedas, J.; Lorente, N.; Pascual, J. I. Long-range repulsive interaction between molecules on a metal surface induced by charge transfer. *Phys. Rev. Lett.* **2007**, *99*, 176103.
- (37) Alemani, M.; Selvanathan, S.; Ample, F.; Peters, M. V.; Rieder, K.; Moresco, F.; Joachim, C.; Hecht, S.; Grill, L. Adsorption and switching properties of azobenzene derivatives on different noble metal surfaces: Au(111), Cu(111), and Au(100). *J. Phys. Chem. C* **2008**, *112*, 10509-10514.
- (38) Barth, J. V.; Brune, H.; Ertl, G.; Behm, R. J. Scanning tunneling microscopy observations on the reconstructed Au(111) surface - atomic-structure, long-range superstructure, rotational domains, and surface-defects. *Phys. Rev. B* **1990**, *42*, 9307-9318.
- (39) Teugels, L. G.; Avila-Bront, L. G.; Sibener, S. J. Chiral domains achieved by surface adsorption of achiral nickel tetraphenyl- or octaethylporphyrin on smooth and locally kinked Au(111). *J. Phys. Chem. C* **2011**, *115*, 2826-2834.
- (40) Jennings, W. B.; Farrell, B. M.; Malone, J. F. Attractive intramolecular edge-to-face aromatic interactions in flexible organic molecules. *Acc. Chem. Res.* **2001**, *34*, 885-894.

- (41) Lu, X.; Hipps, K. W.; Wang, X. D.; Mazur, U. Scanning tunneling microscopy of metal phthalocyanines: d(7) and d(9) cases. *J. Am. Chem. Soc.* **1996**, *118*, 7197-7202.
- (42) Lu, X.; Hipps, K. Scanning tunneling microscopy of metal phthalocyanines: d(6) and d(8) cases. *J Phys Chem B* **1997**, *101*, 5391-5396.
- (43) Iancu, V.; Deshpande, A.; Hla, S. W. Manipulating Kondo temperature via single molecule switching. *Nano Lett.* **2006**, *6*, 820-823.
- (44) Auwaerter, W.; Seufert, K.; Klappenberger, F.; Reichert, J.; Weber-Bargioni, A.; Verdini, A.; Cvetko, D.; Dell'Angela, M.; Floreano, L.; Cossaro, A.; Bavdek, G.; Morgante, A.; Seitsonen, A. P.; Barth, J. V. Site-specific electronic and geometric interface structure of Co-tetraphenyl-porphyrin layers on Ag(111). *Phys.Rev.B* **2010**, *81*, 245403.
- (45) Wang, Y.; Hush, N. S.; Reimers, J. R. Simulation of the Au(111)-(22 x $\sqrt{3}$) surface reconstruction. *Phys. Rev. B* **2007**, *75*, 233416.
- (46) Chen, W.; Madhavan, V.; Jamneala, T.; Crommie, M. Scanning tunneling microscopy observation of an electronic superlattice at the surface of clean gold. *Phys. Rev. Lett.* **1998**, *80*, 1469-1472.

Control of the axial coordination of a surface-confined manganese(III) porphyrin complex

5.1. Introduction

The ubiquity in nature of heme-containing oxygenases has inspired great interest in their synthetic metalloporphyrin analogues.¹ A myriad of sterically hindered metalloporphyrins have been identified as catalysts in biomimetic oxygenation reactions.² The more synthetically accessible “first generation” analogues, which exhibit structurally unencumbered (porphyrin) ligands, undergo facile oxidative deactivation through μ -oxo dimer formation or irreversible ligand oxidation.³ Since both deactivation pathways are bimolecular in the catalyst, synthetic efforts have focused on sterically isolating the active metal-oxo complex.^{4, 5} On metal surfaces, planar metalloporphyrins commonly adopt a flat lying orientation where one coordination site of the metal ion is confined to the molecule-substrate interface,⁶ intrinsically precluding such oxidative deactivation. Accordingly, surface-confinement offers a promising approach to increasing the catalytic capability of simple metalloporphyrin complexes.

The rich coordination chemistry of manganese porphyrins makes them ideal candidates for a wide range of chemically responsive applications.⁷ Complexes of manganese porphyrins are known to catalyze the hydroxylation⁸ and halogenation^{9, 10} of aliphatic substrates, and have shown high reactivity toward alkene epoxidation^{11, 12} (App. A, Fig. 1). Recently, STM imaging of individual manganese porphyrin catalysts at a liquid-solid interface was reported, wherein, the formation of an oxomanganese porphyrin intermediate was visualized prior to the chemical transformation of alkenes into epoxides.¹³

Concerning the chloro(5,10,15,20-tetraphenylporphyrinato)manganese(III) (Cl-MnTPP) molecule, the metal-bound Cl ligand maintains the central manganese atom in the

stable +3 oxidation state.¹⁴ The manganese(II) porphyrin would otherwise rapidly and irreversibly oxidize under ambient conditions. The resulting axial asymmetry, allows for two distinct surface conformations of the Cl-MnTPP molecule; namely, an upward or downward orientation of the Cl ligand with respect to the substrate. Hence, an understanding of the axial interactions of the Cl-MnTPP molecule at the vacuum interface necessitates a fundamental knowledge of the corresponding substrate interface. In this manner, the decisive factor governing the coordination properties of the central manganese atom is the ability to selectively dissociate the axial Cl ligand.

For its mild oxidative effect the coordination of molecular oxygen by surface-confined metalloporphyrins holds particular interest. The ability of the Cl-MnTPP complex to catalyse versatile oxygenation reactions, with molecular oxygen as oxidant in the absence of a sacrificial co-reductant, is well established.¹⁵⁻¹⁷ In clarifying the mechanism of reversible dioxygen binding, an insight into the coordination geometry and characteristic (reduced) oxidation state of the activated dioxygen is required. In this respect, the absence of a readily oxidizable species on-surface makes possible the isolation of the corresponding dioxygen adduct. The co-adsorption of small molecules (such as O₂) has recently been demonstrated to influence the molecular arrangement of metalloporphyrin monolayers.¹⁸ It is therefore of fundamental interest to reveal the relationships between the on-surface molecular arrangements and the formation of the dioxygen adduct.

In this study, vapour deposited Cl-MnTPP molecules (Figure 5.1) on the Ag(111) surface are examined by using scanning tunnelling microscopy (STM), low energy electron diffraction (LEED) and x-ray photoelectron spectroscopy (XPS). STM and LEED are used in order to determine the structure of the molecular overlayer and its registry with the substrate. Combining these techniques with XPS, the surface conformation of the individual molecules is revealed. Element specific and chemical state information obtained by means of XPS, are used to confirm the thermally induced cleavage of the metal-ligand bond, and the integrity of the resulting manganese complex. Subsequent oxygenation of the coordinatively unsaturated MnTPP complex is probed directly by means of STM.

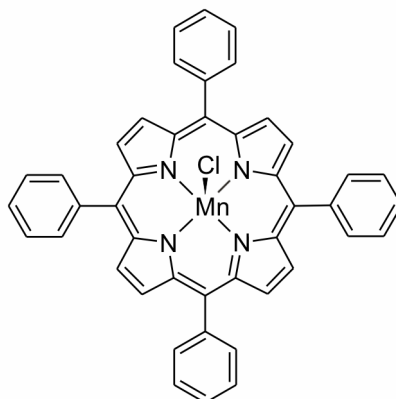


Figure 5.1. Structural formula of the Cl-MnTPP molecule.

5.2. Experimental Methods

The STM, LEED and XPS experiments were conducted in ultra-high-vacuum, (with a base pressure below 1×10^{-10} mbar), as described in Chapter 2. STM imaging was performed as described in Chapter 3. The STM data were processed using the WSxM software package.¹⁹ The LEED diffraction patterns were obtained as described in Chapter 3. XPS measurements were carried out (using an Omicron ESCA+ spectrometer) as described in Chapter 4. The spectrometer was operated with one of two analyzer pass energies, with overall energy resolutions of 1.0 eV and 1.4 eV respectively, the latter in cases where increased sensitivity was required: the Mn 2p core-level spectra; and those of the Cl 2p reported in Figure 5.5. The core-level binding energies were referenced to the Ag 3d $_{5/2}$ line (368.2 eV) of the clean Ag surface.

A single-crystal Ag(111) surface (Surface Preparation Laboratory) was used as the substrate. The Ag(111) crystal was cleaned *in situ* by repeated cycles of argon ion sputtering followed by annealing as described in Chapter 3. The Cl-MnTPP was synthesized according to a published procedure.²⁰ The Cl-MnTPP was evaporated at a rate of about 0.2 ML (monolayer) per minute, at a temperature of approximately 600 K. Experimental aspects of molecular deposition follow those described in Chapter 3.

Molecular oxygen (Sigma Aldrich, 4N) was dosed at a constant (partial oxygen) pressure of 1.5×10^{-6} mbar.

5.3. Results and Discussion

5.3.1. Molecular organization: self-assembly and registry with the Ag(111) surface

Upon deposition, the Cl-MnTPP molecules undergo two-dimensional self-assembly on the Ag(111) surface. Figure 5.2(a) shows a typical occupied state STM image of the highly ordered lattice structure formed at monolayer coverage. The inset shows an enlarged view, in which an individual molecule is highlighted. The Cl-MnTPP lattice is described by a square unit cell (Fig. 5.2(a) inset); the lengths of the primitive lattice vectors (b_1 and b_2) are equal to 1.41 ± 0.05 nm, while the subtended angle is $90 \pm 2^\circ$. This lattice structure has also been reported for the first layer of CoTPP on both the Ag(111)^{21, 22} and Au(111)²³ surfaces, while on the latter, it is found to be adopted by Ni- and Cu-TPP²³. Hence, the ordering of the Cl-MnTPP molecules reflects that typically observed for metallo-TPPs on low reactivity surfaces, with corresponding high mobility and strong lateral intermolecular interaction. Within a single domain, the principal molecular axes of the individual Cl-MnTPP molecules (here defined along the lines of apposing pyrrole groups – see below), are found to be in parallel alignment, and together show an azimuthal rotation of $\pm 15 \pm 2^\circ$ relative to the primitive lattice vectors of the overlayer unit cell. Recent studies of both metallo (Fe-,²⁴ Co-^{21, 24}) and free-base TPP²⁴ on the Ag(111) surface have reported the same alignment of the molecular axis within the overlayer, indicating that the observed azimuthal rotation arises from peripheral interactions. In this arrangement, the phenyl groups of adjacent molecules align edge-to-face, in the so-called T-shape configuration; thus reflecting the attractive interaction known for benzene dimers²⁵. It is well established that this T-shape configuration of the phenyl groups induces attractive intermolecular interactions,²⁶ thus playing a significant role in the self-assembly of both free-base and metallated TPPs²⁴.

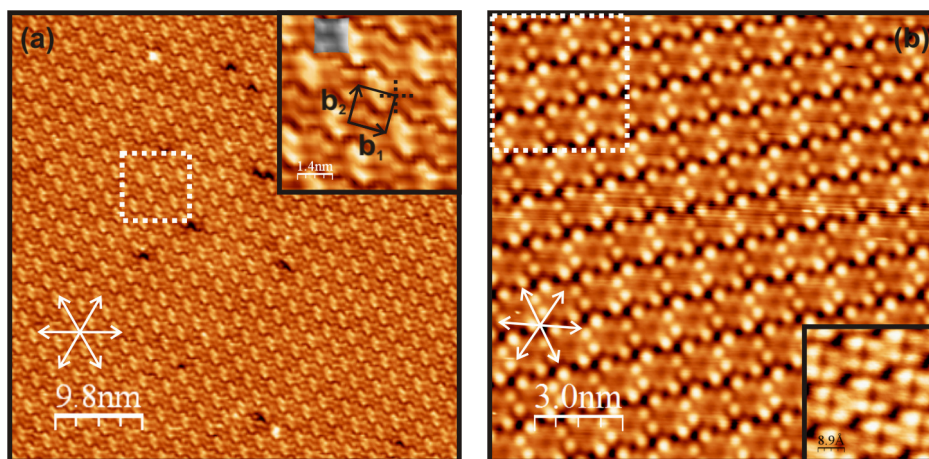


Figure 5.2. STM images obtained from the Cl-MnTPP monolayer on the Ag(111) surface. The close-packed directions of the Ag(111) surface are indicated by white arrows. (a) Large-scale occupied state STM image; $V_{\text{sample}} = -1.20$ V, $I_t = 0.25$ nA, size 50 nm \times 50 nm. The inset shows an enlarged view of the region highlighted by the white dotted box; an individual Cl-MnTPP molecule is indicated in greyscale. The unit cell and primitive lattice vectors (b_1 , b_2) are shown in black; the principal molecular axes are indicated by the dotted lines. (b) High resolution occupied state STM image; $V_{\text{sample}} = -1.20$ V, $I_t = 0.25$ nA, size 15 nm \times 15 nm. The inset shows the corresponding unoccupied state STM image of the region highlighted by the white dotted box; $V_{\text{sample}} = 1.20$ V, $I_t = 0.25$ nA, size 4.5 nm \times 4.5 nm.

In the occupied state STM image of Figure 5.2(b), the individual molecules show four bright terminal protrusions, between which are found a further set of lesser intensity. Based on the molecular dimensions, the terminal protrusions are attributed to the phenyl groups. In turn, the pyrrole groups of the porphyrin macrocycle, which are located between adjacent phenyl groups, are tentatively assigned to the four core protrusions. Thus, the Cl-MnTPP molecules are seen to adopt an orientation where the average plane of the porphyrin macrocycle lies parallel to that of the Ag(111) surface. In contrast, the unoccupied state STM image shown in the inset reveals a striking difference in the observed intermolecular features. Here the molecular profile is found to be dominated by four lobes localized over the meso-bridge carbons and phenyl groups. This assignment is based on the profile observed in the occupied state image. The observed contrast may be attributed to a difference in the local density of states associated with the occupied and

unoccupied molecular orbitals, probed by the applied bias-voltage. A feature common to both molecular profiles, however, is that of a central depression at the porphyrin core. This is especially noteworthy, given the axial asymmetry of the Cl-MnTPP molecule which arises due to the Cl ligand, and is discussed below.

Consistent with a planar conformation of the porphyrin macrocycle, the pyrrole groups are found to express approximately the same apparent height. This finding is seemingly at odds with the crystallographic structure of the Cl-MnTPP molecule, in which the conformational geometry of the porphyrin macrocycle shows quasi four-fold improper-rotation symmetry²⁷. It is plausible that adsorption of the Cl-MnTPP molecule on to the Ag(111) surface enhances the repulsion between the axial Cl ligand and the porphyrin macrocycle, inducing a slight “doming” of the latter. Such an adsorption induced conformation of the porphyrin macrocycle would also present pyrrole groups of the same apparent height. It is noted that the crystallographic structure of the closely related chloro(tetraphenylporphyrinato)manganese(II) (Cl-Mn(II)TPP) anion reveals a substantially domed porphyrin ligand,²⁸ presumably reflecting a greater repulsion between the axial and equatorial ligands. Although a slight non-planar configuration cannot be ruled out, the apparent planarity of the porphyrin macrocycle may point to a surface induced conformation. In a recent study of [tetra(4-bromophenyl)porphyrinato]cobalt(II) (CoTBrPP) (App. A, Fig. 5) on the Cu(111) surface,²⁹ it was found that the molecular conformation played a decisive role in the observed highest occupied molecular orbital (HOMO). When the molecule presented a planar conformation a HOMO related to the d_z^2 orbital of the central Co atom was found. However, in a saddle conformation, with a larger Co-surface distance, no such relation was observed. Although in the present case, the porphyrin macrocycle exhibits an ostensibly planar conformation, the axial asymmetry of the Mn atom can be expected to strongly influence the tunnelling states localized at the centre of Cl-MnTPP molecule. Here it is noted that XPS spectra obtained from the Cl-MnTPP molecules at monolayer coverage (see below), reveal a chemical environment of the Cl ligand consistent with an upward orientation relative to the Ag(111) surface. In both the crystallographic²⁷ and calculated³⁰ structures of the Cl-MnTPP molecule, the Mn atom is found to be displaced from the average plane of the pyrrole nitrogens, towards the Cl ligand. As the Cl ligand of the adsorbed Cl-MnTPP molecule is found to be orientated

away from the Ag(111) surface, the Mn atom can therefore be expected to follow an upward projection. In this context, the depression displayed at the centre of the Cl-MnTPP profile (Fig. 5.2(b)), is not representative of the actual topographic height. It then follows that the distorted coordination environment of the central Mn atom, in a similar manner to CoTBrPP on the Cu(111) surface, may influence the d_z^2 orbital contribution to the tunnelling current; thus, to some degree reflected in the apparent height at the porphyrin core. It is noted, however, that the Mn-complex after the removal of the Cl ligand (see below), also presents a central depression. Therefore, while the participation of the d_z^2 orbital in both the HOMO and lowest unoccupied molecular orbital (LUMO) may affect the observed tunnelling images, the influence of the Mn coordination environment is considered to be relatively small.

Figure 5.3(a) shows the LEED pattern obtained from approximately 1ML of the Cl-MnTPP molecules on the Ag(111) surface. Twelve first order diffraction spots are observed, equally spaced and equidistant from the central zero order spot. Furthermore, the pattern is found to be invariant with respect 120° rotations, in accordance with the three-fold symmetry of the Ag(111) surface. As such, the pattern is interpreted as being that of a superposition of three rotationally equivalent domains of a square lattice. The individual domains are highlighted (Fig. 5.3(a)), with the reciprocal lattice vectors of one, given as b^*_1 and b^*_2 , with the subtended angle β^* equal to $90 \pm 2^\circ$. The structure of the molecular overlayer displayed by LEED is therefore in good agreement with that observed in STM images.

The molecular overlayer lattice as revealed in the LEED data, exhibits a preferred orientation to that of the substrate, thus implying an epitaxial relationship. The LEED pattern of the underlying Ag(111) surface is shown in the inset of Fig. 5.3(a). A comparison of the molecular overlayer and substrate LEED patterns reveals their relative orientation. This is visualized in Fig. 5.3(a), where the close-packed directions of the substrate reciprocal lattice are shown superimposed on that of the molecular overlayer pattern. Within this framework, the principal lattice vector (b^*_1) of the overlayer shows an azimuthal rotation θ of $15 \pm 2^\circ$ relative to that of the substrate (a^*_1). In turn, one diagonal of the molecular overlayer unit cell is found to be aligned with the $\langle \bar{1}01 \rangle$ close-packed

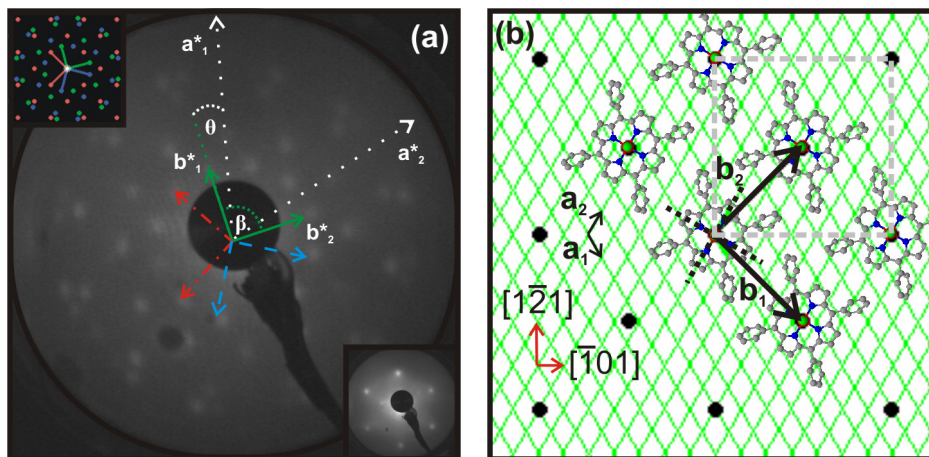


Figure 5.3. (a) LEED pattern from 1ML of the Cl-MnTPP molecules on the Ag(111) surface acquired at a primary beam energy of 13.0 eV. The insets show the LEED pattern of the Ag(111) surface acquired at the higher beam energy of 112.0 eV (lower) and a simulated LEED pattern of the Cl-MnTPP overlayer created using the observed lattice parameters (upper). The individual rotational domains of the Cl-MnTPP overlayer are indicated by the green (solid), blue (dashed) and red (dotted/dashed) lines. b^*_1 and b^*_2 are the reciprocal lattice vectors of the rotational domain indicated in green, with the subtended angle given by β^* . The dotted white lines labelled a^*_1 and a^*_2 show close packed directions of the Ag(111) reciprocal lattice, whereby the angle θ indicates the azimuthal rotation of the molecular overlayer. (b) Schematic representation of the azimuthal orientation of the Cl-MnTPP overlayer on the Ag(111) surface. The black dots represent the Cl-MnTPP molecules with the points of intersection of the green mesh that of the Ag atoms. The lattice vectors of the Ag(111) surface and Cl-MnTPP overlayer are labelled a_1 , a_2 and b_1 , b_2 , respectively. The principal molecular axes are indicated by the dotted lines (black); the dashed box (grey) outlines the coincident overlayer supercell.

directions, while the other follows the $\langle \bar{1}21 \rangle$ crystallographic directions. Accordingly, the lattice vectors of the molecular overlayer may be expressed in terms of those of the substrate through the following transformation:

$$\begin{pmatrix} b_1 \\ b_2 \end{pmatrix} = \begin{pmatrix} 5.44 & 1.46 \\ 1.46 & 5.44 \end{pmatrix} \begin{pmatrix} a_1 \\ a_2 \end{pmatrix}$$

where the Ag(111) nearest-neighbour distance is 0.289nm. A schematic representation of the corresponding Cl-MnTPP overlayer lattice (for a single rotational domain) superimposed on that of the Ag(111) surface, is shown in Figure 5.3(b). The graphic clearly illustrates that the primitive unit cell dimensions preclude a commensurate configuration of the molecular overlayer with the substrate lattice. However, it can be seen that the corresponding $(\sqrt{2} \times \sqrt{2})R45^\circ$ super-cell, approaches a coincident registry with the substrate lattice points. In addition, every overlayer lattice point coincides with one of the primitive substrate lattice lines. Therefore, within the uncertainty of the measurement, the nature of the molecule-substrate interface is consistent with that previously described as point-on-line (POL) coincidence (ref. 31 and references therein).

Through a comparison with the molecular motif observed in STM images (Figure 5.2), the azimuthal orientation of the individual Cl-MnTPP molecules may be directly related to corresponding directions on the Ag(111) surface. This is illustrated in Fig. 5.3(b), whereby the principal molecular axes of individual Cl-MnTPP molecules (depicted by structural models) show the observed $15 \pm 2^\circ$ azimuthal rotation relative to the primitive lattice vectors of the overlayer. In this configuration, while one of the molecular axes is aligned with the $\langle 0\bar{1}1 \rangle$ close-packed directions of the Ag(111) surface, the other follows the $\langle \bar{2}11 \rangle$ crystallographic directions. In turn, a symmetry equivalent configuration is obtained for the mirror azimuthal orientation. Thus, while the primitive lattice vectors of the Cl-MnTPP overlayer show an azimuthal rotation relative to those of the Ag(111) surface, the principal axes of individual molecules are found to be aligned with the substrate high symmetry directions. These findings are supported by a recent study of the interface structure of CoTPP on the Ag(111) surface, where alignment with the same crystallographic directions of the substrate is reported²¹.

The axial asymmetry arising from the Cl ligand allows for two distinct surface conformations of the Cl-MnTPP molecule. Depending on the conformation, the axial Cl ligand may point upwards or downwards with respect to the Ag(111) surface. Since chlorine is known to undergo chemical reaction with the Ag(111) surface³² it can be expected that for molecules of the first layer, the chemical environment of the Cl ligand will depend on the substrate conformation. In turn, for molecules in the second layer, the Cl

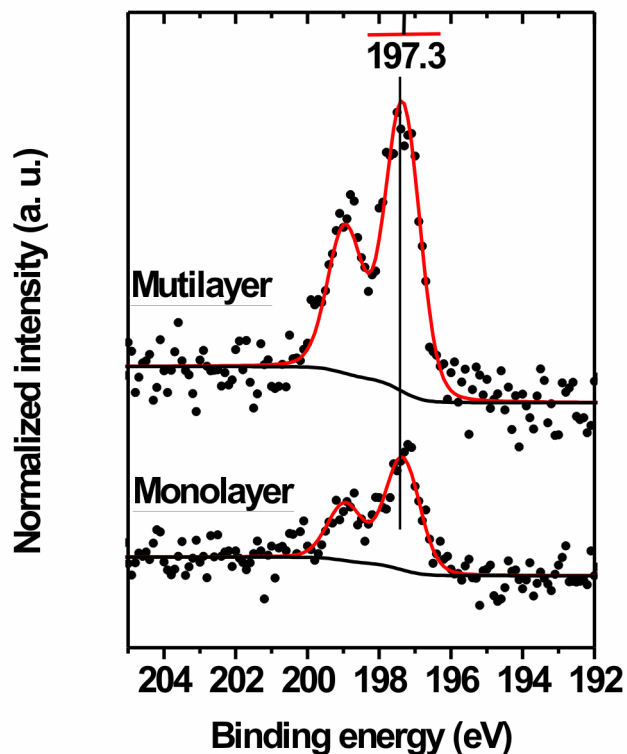


Figure 5.4. Cl 2p XPS spectra obtained from the Cl-MnTPP overlayer on the Ag(111) surface at coverage of ~ 1 ML (lower) and ~ 2.5 ML (upper). The dots represent the spectral data. The red and black lines correspond to the best fit to the spectral data and Shirley backgrounds respectively.

ligand is effectively decoupled from the Ag(111) surface. It follows that the Cl ligand of an upward pointing conformation will have a chemical environment similar to that of a second layer molecule. In this way the molecular conformation on the substrate may be inferred from chemical state of the Cl ligand. The Cl 2p XPS spectrum obtained from a surface coverage of ~ 1 ML is shown in Figure 5.4 (lower). Two photoelectron lines are observed which are assigned to a single Cl 2p spin-orbit doublet, the fit of which yields a binding energy of 197.3 eV for the $2p_{3/2}$ line, with a spin-orbit splitting of 1.6 eV. The corresponding spectrum acquired at a surface coverage of 2-3 ML is shown in Figure 5.4 (upper). The initial Cl 2p doublet shows an increase proportional to that of the increased coverage, however, no additional spectral components are observed. This suggests a single chemical state of the Cl ligand for molecules of the first and second molecular layers. The inference therefore, is that the Cl-MnTPP molecules adsorb on the Ag(111) surface with the

Cl ligand pointing upwards. The steric hindrance of the large axial Cl ligand would thus be alleviated, allowing for an increased coupling of the extended molecular π system to the substrate.

5.3.2. Thermal lability: dissociation of the axial Cl ligand

The thermally evaporated Cl-MnTPP molecules adsorb on the Ag(111) surface with the axial Cl ligand predominantly undissociated. This is evidenced by C 1s and Cl 2p XPS spectra (see below), which yield a C/Cl atomic ratio of 44 : 0.8 (± 0.3), consistent, within the uncertainty, with the expected stoichiometry of 44 : 1. The adsorbed Cl-MnTPP molecules are found, however, to display a latent thermal lability which results in the dissociation of the Cl ligand. The onset of Cl dissociation, as reflected in the Cl 2p photoemission intensity, is observed to occur at ~ 423 K. At this temperature, the rate of dissociation is slow, with Cl loss complete only after several hours. Figure 5.5 shows the C 1s and Cl 2p XPS spectra acquired from ~ 1 ML of the Cl-MnTPP molecules as deposited and, after annealing at 423 K for ~ 15 hrs. The initial Cl 2p doublet of the deposited layer is reduced to within the noise level after annealing. However, in the corresponding C 1s line, a reduction of scarcely 10% is observed. Therefore, the combination of lateral intermolecular and molecule-substrate interactions is strong enough to keep the porphyrin complex adsorbed on the substrate, while the Cl ligand is lost. Recent studies of chloromanganese porphyrins^{33, 34} have reported a similar thermal lability of the axial Cl ligand, although occurring at slightly higher temperature (473 K) and achieved by surface tethering via thiol groups (Appendix A, Figure 12).

The C 1s lineshape, which is observably the same in the XPS spectra of the deposited and annealed layers, is noticeably broadened at the peak base. This finding can be interpreted as being the result of photoemission from chemically distinct carbon species within the porphyrin complex. Guided by the Cl-MnTPP molecular formula, four plausibly different chemical species of carbon atoms can be identified: the meso-bridge carbons (C_m); those of the phenyl groups (C_{ph}); and those at the α and β positions of the pyrrole groups ($C_{N\alpha}$ and $C_{N\beta}$ respectively). The relative number of each species is highlighted by the TPP quadrant shown in the inset of Fig. 5.5; here, chemically equivalent carbons are indicated

by the same colour. Estimation of the relative energy positions of the different spectral contributions follows a recent report by Nardi et al.³⁵ on the C 1s core level spectrum of TPP; noting however, that the chemical state of the pyrrole nitrogens in metalloporphyrins (Fe,³⁶ Co,³⁷ Zn³⁸) tends towards that of the aza (-N=) nitrogens in the free-base TPP analogue. The resulting fit of the C 1s spectra (Fig. 5.5 lower/upper), yields four principal components. The largest (blue) corresponds to ~ 52% of the total envelope area, and hence is assigned primarily to C_{ph} emission. Two components of equal area (~ 17%), but shifted to higher (green) and lower (red) binding energy, are attributed to C_{N α} and C_{N β} emission, respectively. The smallest component (orange) with an area of ~ 8% is thus assigned to C_m emission. A fifth broader component (grey) is included in the fit to accommodate the energy loss structure at higher binding energy³⁵, accounting for the somewhat smaller than expected intensity of the principal components. In a recent study of free-base TPP on the Ag(111) surface,³⁹ a chemical modification of the porphyrin skeleton upon annealing above 525 K was reported; here, a change in the C 1s lineshape was observed. In the present case, the apparent C 1s lineshape may be considered to reflect a quasi-fingerprint of the porphyrin complex, thus implying that the structure remains intact on loss of the Cl ligand.

The dissociation of the Cl ligand occurs without the demetallation of the porphyrin complex, thus giving rise to an Mn centre that is coordinatively unsaturated. Figure 5.6 (a) and (b) show respectively the Mn 2p_{3/2} XPS spectra obtained from the Cl-MnTPP monolayer as deposited, and after annealing to the complete removal of the Cl ligand. Multiplet splitting of the Mn 2p_{3/2} photoelectron lines (Fig. 5.6), gives rise to their noticeable broadness. The splitting arises when, upon photoemission, the unpaired electron of the core level couples with those of the open valence shell, resulting in multiple final states. Consequently, the multiplet structure of the Mn 2p_{3/2} envelope is sensitive to the number of unpaired electrons in the valence shell, which in turn can be related to the Mn oxidation state.

Interpretation of the apparent Mn 2p_{3/2} lineshape in terms of the underlying multiplet structure follows the calculated multiplet splitting of the Mn 2p vacancy levels, performed by Gupta and Sen⁴⁰. In this respect, the calculated XPS spectra for the Mn +2, +3, and +4 ions have been considered, given that the cleavage of the metal-ligand bond may result in a one electron transfer. This approach has been demonstrated previously;⁴¹

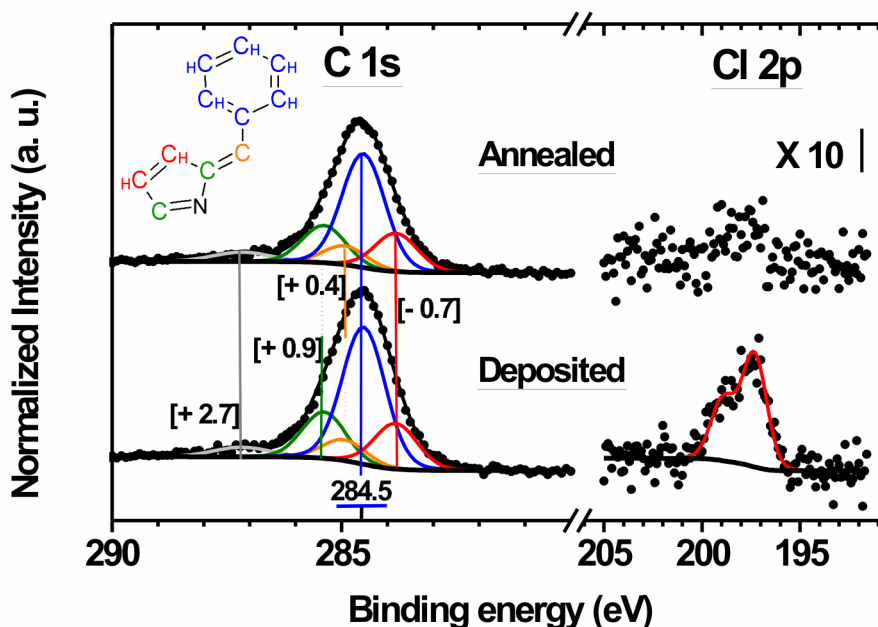


Figure 5.5. C 1s (left) and Cl 2p (right) XPS spectra obtained from the Cl-MnTPP monolayer on the Ag(111) surface as deposited (lower), and after annealing at 423 K (upper). The dots represent the spectral data. Left: The best fit to the spectral data and Shirley background lines are shown in black; the component peaks are colour coded to the non-equivalent carbons shown inset. The bracketed values correspond to shifts in binding energy of component peaks relative to the peak of largest intensity. Right (lower): The red and black lines correspond to the best fit and Shirley background, respectively.

wherein, the essential features of experimentally obtained Mn 2p XPS spectra of Mn +2, +3, and +4 oxides and oxyhydroxides have been reproduced by the calculated multiplet structure. In the present case, however, it should be noted that much of the multiplet structure remains unresolved, due to the weak signal-to-noise ratio of the Mn 2p_{3/2} spectra (Fig. 5.6 (a) and (b)). This is a consequence of the low number density of the Mn atoms in the molecular monolayer. Even so, the underlying multiplet structure can reasonably be expected to affect the observed Mn 2p_{3/2} lineshape and moreover, the binding energy extent of the spectral envelope. Hence, the chemical state of the central Mn atom may be distinguished.

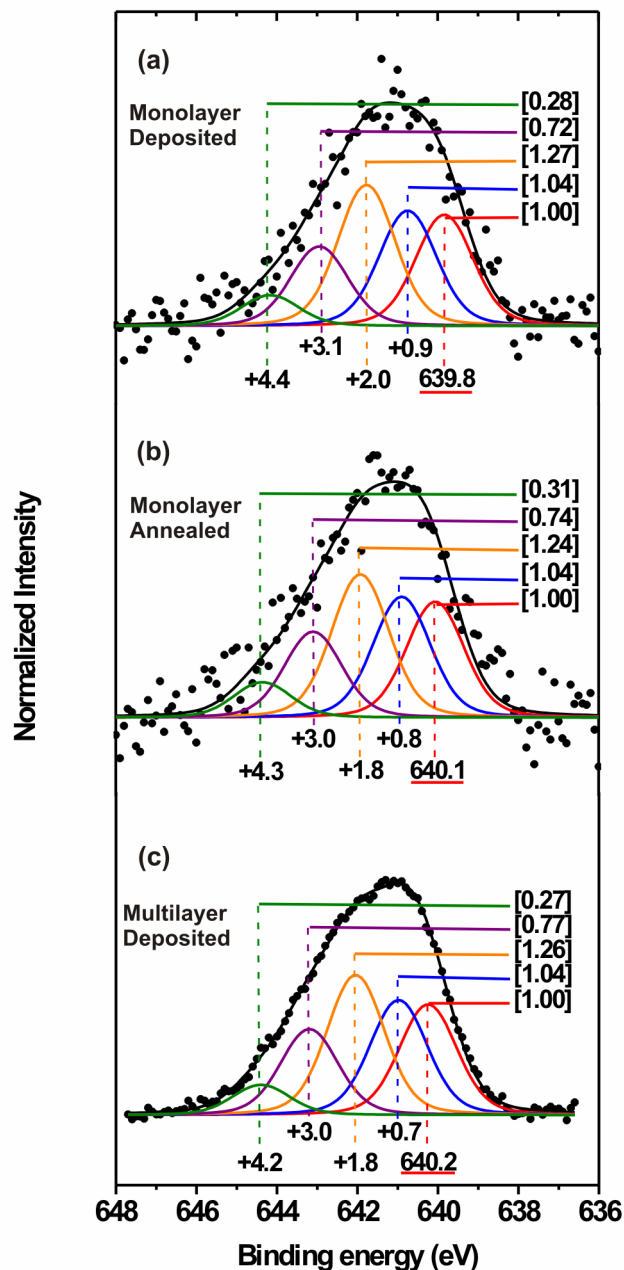


Figure 5.6. Mn 2p_{3/2} XPS spectra obtained from the Cl-MnTPP overlayer on the Ag(111) surface. (a) Spectrum obtained from the deposited monolayer, and (b) after annealing to the complete loss of the Cl ligand. (c) Spectrum obtained from the deposited multilayer (~ 5 ML). The dots represent the spectral data. The best fit to the spectral data is shown in black; the component peaks are indicated in colour. Peak intensities (bracketed values) are relative to that of the lowest binding energy component.

Accordingly, multiplet parameters obtained from the calculated Mn 2p multiplet splitting⁴⁰ have been used as initial constraints in the fit of the present Mn 2p_{3/2} photoelectron lines. The resulting best-fit of the Mn 2p_{3/2} spectrum from the pre-anneal surface (Fig. 5.6(a)), yields multiplets of relative intensities and energy splittings which are similar to those calculated for the Mn(III) ion⁴⁰. As such, the spectrum reflects the chemical state of the Mn atom in Cl-MnTPP molecule, which is expected to exist in the +3 oxidation state. In the case of the Mn(III) ion, the calculated multiplet component of lowest binding energy differs from that of the Mn(II) and Mn(IV) ions by +0.7eV and -1.0 eV, respectively.⁴⁰ It follows that a change in the oxidation state of the Mn atom, on cleavage of the Cl ligand bond, should result in a clear shift in the binding energy onset of the Mn 2p_{3/2} envelope. However, the onset of the Mn 2p_{3/2} envelopes, from the pre- and post-anneal surfaces, occur at approximately the same binding energy. Furthermore, a strikingly similar multiplet structure is obtained in the fit of the Mn 2p_{3/2} spectrum from the post-anneal surface (Fig. 5.6(b)). By way of confirming the proposed multiplet structure, the Mn 2p_{3/2} spectrum obtained from the deposited multilayer, with correspondingly enhanced signal-to-noise, is considered. It is first noted that at the present multilayer coverage (~ 5 ML), the core level binding energies as reflected in the C 1s line, experience a shift to higher binding energy of ~ 0.1 eV. Similar shifts toward higher binding energies at increasing coverage have been reported elsewhere for both metallo -TPPs³⁷ and -phthalocyanines⁴². Here, the observed shift is attributed to greater final-state screening of core-holes created in the molecular layers near the metallic substrate, compared to those at the multilayer surface. Figure 5.6(c) shows the Mn 2p_{3/2} XPS spectrum obtained from the Cl-MnTPP molecules (as deposited) at a coverage of ~ 5 ML. On inspection it is found that the Mn 2p_{3/2} lineshape presented by the molecular multi- and mono-layer surfaces are ostensibly the same. As expected, the fit of Mn 2p_{3/2} spectrum from the multilayer surface yields multiplet structure very similar to that determined for the pre- and post-anneal monolayer surfaces; thus implying that little interaction takes place between the central Mn atom and the Ag(111) surface. The implication therefore, is that the thermally induced dissociation of the Cl ligand from the Cl-MnTPP molecules adsorbed on the Ag(111) surface, occurs through a heterolytic cleavage of the metal-ligand bond. As such, the substrate may be expected to compensate for the net charge of the porphyrin complex. The dissociation of the axial

ligand in this manner, is in keeping with the relative stabilities of Mn(II) and Mn(III) porphyrins, the latter of which being the most stable⁴³.

STM images reveal that the loss of the Mn-bound Cl ligand leaves the porphyrin complex otherwise intact. Accordingly, the indicated Mn(III) complex is confidently assigned to the MnTPP molecule. Figure 5.7(a) shows typical occupied (main) and unoccupied (inset) state STM images of the MnTPP molecules on the Ag(111) surface at \sim 1ML, following the complete removal of Cl from an equivalent coverage of the deposited Cl-MnTPP. Although without the axial Cl ligand, the MnTPP molecule displays a profile which closely resembles that observed from the Cl-MnTPP precursor (Fig. 5.2(b)). In the occupied state STM image of Fig. 5.7(a), features associated with the phenyl substituents and porphyrin macrocycle are clearly discernable. In turn, the intramolecular features appear to follow a related bias-voltage dependence, as evidenced in the unoccupied state STM image shown inset. The most salient feature, however, is that of a depression at the porphyrin core, comparable to that displayed by the Cl-MnTPP molecular profile.

As mentioned above, it is found that the HOMO of CoTBrPP (in a planar conformation on the Cu(111) surface), contains some contribution from the d_z^2 orbital of the central Co atom.²⁹ Conversely, in the case of CuTBrPP, which differs only by the central Cu atom, a corresponding d-orbital contribution to the HOMO is absent.²⁹ Recently reported STM images of the closely related Co- and Cu-TPP molecules,²⁶ reveal distinct differences in the apparent height of the respective porphyrin cores; specifically, in the former a protrusion is observed, while a depression is displayed by the latter. Therefore it follows that the d-orbital participation (of the central metal atom) in the frontier molecular orbitals may influence the apparent height at the porphyrin core. Such a conclusion may be inferred from an earlier report on structurally related metallo-phthalocyanines (App. A, Fig. 7) where it was proposed that the central metal d-orbital character near the Fermi energy influenced the observed tunnelling images⁴⁴. For the Cl-MnTPP molecule, displacement of the Mn atom toward the axial Cl ligand can be expected to diminish the direct coupling of the d_z^2 orbital of the central Mn atom with the Ag(111) surface. It is apparent from the MnTPP molecular profile, however, that the core depression is largely independent of the present Mn-surface distance. It is thus tentatively proposed that the depression in the apparent height of the Mn-complexes reflects a relatively minor contribution of the d_z^2

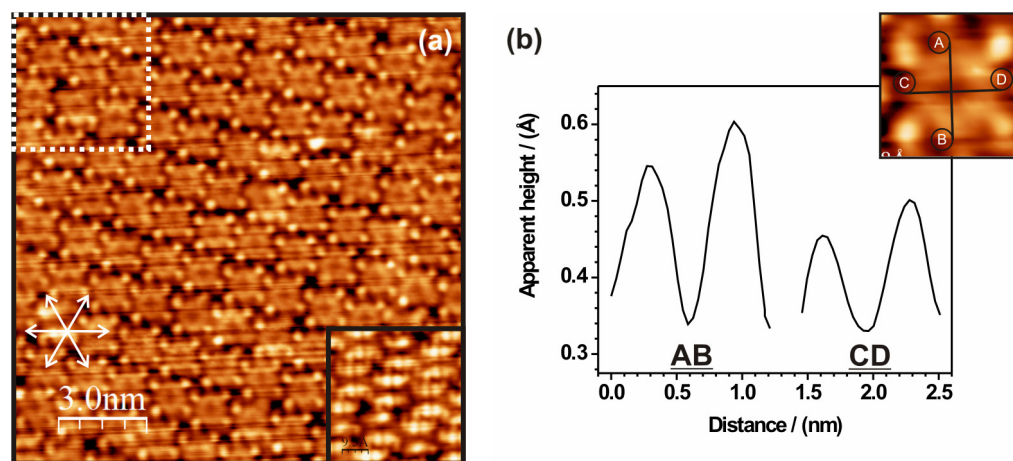


Figure 5.7. STM images obtained from the MnTPP monolayer on the Ag(111) surface. The close-packed directions of the Ag(111) surface are indicated by white arrows. (a) Occupied state STM image of the MnTPP layer; $V_{\text{sample}} = -1.20$ V, $I_t = 0.25$ nA, size 15 nm \times 15 nm. The inset shows the corresponding unoccupied state STM image of the region highlighted by the white dotted box; $V_{\text{sample}} = 1.20$ V, $I_t = 0.25$ nA, size 4.5 nm \times 4.5 nm. (b) Height profiles taken along the lines of opposing pyrrole groups of the MnTPP molecule shown inset.

orbital of the central Mn atom to the frontier molecular orbitals probed by the applied bias-voltage. Here it is noted that while STM images of Co- and Fe-TPP display core protrusions,²⁴ those of Cu-,²⁶ Au-⁴⁵ and Ni-TPP⁴⁶ show characteristic depressions, in this respect little different to the free-base TPP²⁴ analogue.

On close examination of the porphyrin macrocycle (Fig. 5.7(a)), a two-fold rotational symmetry is observed, consistent with a saddle distortion, where two opposite pyrrole groups tilt upwards and two downwards with respect to the surface plane⁴⁷. A corresponding difference in apparent height is shown in Figure 5.7(b), which presents height profiles taken along the lines of opposing pyrrole groups. This represents a change from the approximately equal apparent heights of the pyrroles groups observed in the case of the Cl-MnTPP precursor (Fig. 5.2(b)). Since the saddle distortion of the Cl-MnTPP porphyrin macrocycle (observed in the crystal structure) is proposed to be brought about by the axial coordination of the Cl ligand,²⁷ the MnTPP derivative might be expected to adopt a planar configuration. Recent theoretical predictions⁴⁷ show, however, that a stabilizing π conjugation exists between the saddled macrocyclic ring and the phenyl groups, as the latter

rotate towards the porphyrin plane. Such a conformational distortion of the MnTPP molecule would, presumably, allow for an increased coupling of the molecular π system to the substrate. The observed two-fold symmetry of the porphyrin macrocycle (Fig. 5.7(b)), therefore, points to a conformational adaptation of the MnTPP molecule, upon adsorption on the Ag(111) surface. Such conformational flexibility of meso-aryl-substituted porphyrins upon adsorption is well established.⁴⁸ On the Ag(111) surface, tetrapyridylporphyrin molecules are found to adopt a conformation in which the pyridyl groups are alternately rotated out of the porphyrin plane,⁴⁹ whereas in the case of Fe- and Co-TPP a concerted phenyl rotation and saddling of the macrocycle is observed²⁴.

Aside from a slight change in the apparent heights of the pyrrole groups, the removal of the axial Cl ligand leaves the molecular appearance comparatively unchanged, conspicuously so at the porphyrin core (Fig. 5.7). These observations clearly indicate that the MOs localized at the porphyrin macrocycle, remain largely unmixed with the orbitals originating from the Cl ligand. Hence, affecting the molecular profile observed in STM images. This conclusion, is supported by the calculated MO structure of the closely related Cl-Mn(II)TPP anion;²⁸ the results of which reveal that among the porphyrin π , Mn d, and Cl ligand orbitals little intermixing takes place. It should be noted, however, that a direct comparison between the d^4 Cl-Mn(III)TPP and the d^5 Cl-Mn(II)TPP complexes, may not be fully appropriate. The additional electron of the d^5 Mn complex induces a lengthening of the coordination bonds, further distorting the square pyramidal coordination geometry of the Mn atom.²⁸ One obvious consequence of this is a reduced overlap of the equatorial (porphyrin) and axial ligand orbitals, which likewise affects their mixing. Consequently, lack of intermixing may be expected to be more pronounced in the case of the d^5 Cl-Mn(II)TPP complex.

Lastly, the ordering of the MnTPP overlayer (Fig. 5.7) is described by a square unit cell, with dimensions equal to those displayed by the Cl-MnTPP precursor. The LEED pattern obtained from the MnTPP molecules on the Ag(111) surface at approximately 1ML, is consistent with that of a square lattice, in good agreement with the structure observed in STM images. Furthermore, the registry of the MnTPP overlayer with the Ag(111) surface, as indicated by LEED, is found to be the same as that observed for the Cl-MnTPP layer. It is evident therefore, that the loss of the Cl ligand has little or no effect on the lateral

intermolecular interaction or the specific adsorption site on the Ag(111) surface. Indeed this may be expected given that the Cl ligand is axially bound to the Mn atom, and is found to be orientated away from Ag(111) surface.

5.3.3. Axial coordination: the formation of a dioxygen adduct of the MnTPP molecule

Upon exposure to molecular oxygen, a fraction of the MnTPP molecules appear markedly different. Figure 5.8(a) shows a typical occupied state STM image of the MnTPP molecules on the Ag(111) surface at approximately 1ML, following exposure to 2.1×10^3 L of molecular oxygen. Distinct in appearance from the MnTPP precursor, a number of molecules (circled) separated by several nearest neighbour distances are imaged with an increased apparent height. On further exposure, the fraction of the brighter species is observed to increase (see below); hence, it is concluded that a reaction of the Mn-complex with dioxygen occurs. Figure 5.8(b) shows the plot of the coverage Θ of the brighter species as a function of time (upper panel), at a constant molecular oxygen pressure (1.5×10^{-6} mbar). It is found that the rate of formation of the brighter species decays exponentially with time; consistent with a reaction that is first-order with respect to the surface concentration of the MnTPP molecules. This is evidenced by the plot of $\ln \Theta_t / \Theta_0$ versus time (lower panel), the fit of which yields a straight line. For the reaction of the Mn-complex with dioxygen, the observed first-order kinetics exclude a concerted dissociative step involving neighbouring MnTPP molecules; as expected, given the lengths of the primitive lattice vectors, ~ 1.4 nm. It is well established that molecular oxygen reacts with a series of low valent manganous- porphyrins⁵⁰⁻⁵² and phthalocyanines⁵²⁻⁵⁴ to form dioxygen adducts. In like manner, the observed interaction can be expected to involve the formal oxidation of the Mn-complex with the concomitant reduction of the adsorbed dioxygen. For metal-centred oxidation, the intermediate valence of the Mn(III) ion can be expected to preclude the reductive cleavage of the coordinated dioxygen. As such, the resulting brighter species are tentatively attributed to a dioxygen adduct of the MnTPP molecule, O_2 -MnTPP.

At a given coverage of the O_2 -MnTPP species, it is found that the individual MnTPP molecules which appear oxygenated (brighter) can change. Figure 5.8 (c) to (e) show consecutive STM images of the same surface region, that highlighted by the dotted

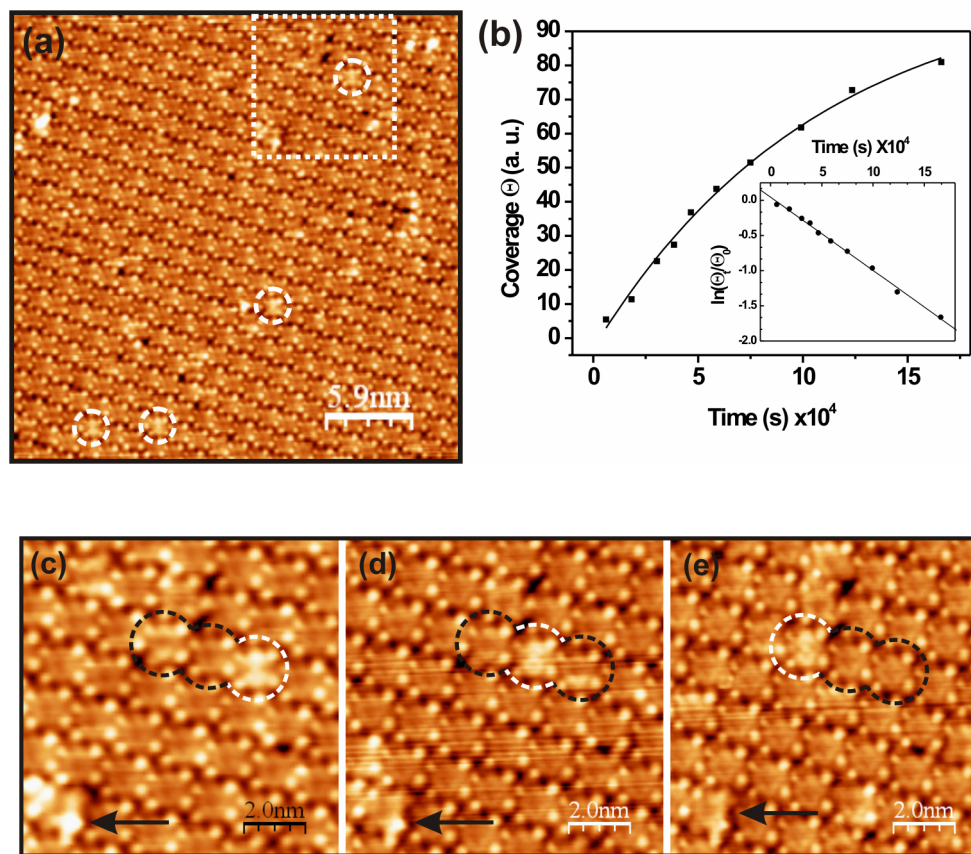


Figure 5.8. STM images obtained from the MnTPP monolayer on the Ag(111) surface following exposure to 2.1×10^3 L of molecular oxygen: (a) Large-scale occupied state STM image; $V_{\text{sample}} = -1.20$ V, $I_t = 0.25$ nA, size $50 \text{ nm} \times 50 \text{ nm}$. The newly formed brighter species are circled. (b) Plot of the coverage Θ of the brighter species as a function of time, at a constant molecular oxygen pressure (1.5×10^{-6} mbar); the line corresponds to the best fit. The inset shows the plot of $\ln \Theta_t / \Theta_0$ versus time. (c) to (e) Sequential STM images of the region highlight by the dotted box; the movement of the brighter species is tracked in white.

box in Fig. 5.8(a), in which a single bright species is observed. A static feature common to the three images is that of a molecular defect site indicated by the arrow. With reference to this feature, MnTPP molecules neighbouring the brighter species in the first image (Fig. 5.8(c)), appear comparably bright in the subsequent images (Fig. 5.8 (d) and (e)); where, the dioxygen has seemingly “hopped” from one to the other. In turn, the resulting deoxygenated species displays the same molecular profile as the MnTPP precursor. Thus, it follows that the observed oxygenation of the MnTPP molecules on the Ag(111) surface is

reversible. In solution, the irreversible oxidation of Mn(II)TPP with exposure to air, proceeds via the formation of a μ -oxo dimer species.⁵⁵ On the Ag(111) surface, however, such a reaction pathway is hindered by the parallel alignment of the porphyrin macrocycle to the substrate; in this way allowing the MnTPP molecules to react reversibly with dioxygen. Though the possible lateral manipulation of the adsorbed dioxygen by the STM tip cannot be excluded, images obtained at a higher O₂-MnTPP coverage (see below) reveal an ordering of the oxygenated species that belies this straightforward interpretation.

Viewed with submolecular resolution, the profile of the O₂-MnTPP molecule reveals distinct protrusions located in a symmetric fashion at the porphyrin core. Figure 5.9(a) shows occupied (main) and unoccupied state (inset) STM images, respectively, of the MnTPP monolayer following exposure to 7.0×10^4 L of molecular oxygen. At this exposure approximately half of the MnTPP molecules appear oxygenated. A MnTPP and neighbouring O₂-MnTPP molecule (circled black and white respectively), are shown enlarged for the occupied state STM image in Figure 5.9 (b) and (c). To demonstrate the salient features, height profiles taken along the lines of opposing pyrrole groups, are shown in Figure 5.9(d). Absent for the profiles of the MnTPP molecule (black), a spike in the apparent height is observed at the centre of the O₂-MnTPP species (red); whence it must be related to an interaction of the dioxygen with the central Mn atom. This central protrusion is not observed in the unoccupied state images of the O₂-MnTPP molecules (Fig. 5.9(b)), indicating that the feature arises due to intrinsic electronic factors, and is not purely of topological origin. For the MnTPP molecule, the saddle conformation is evidenced, with opposite pairs of pyrrole groups expressing a slight difference in apparent height; a feature common to both the occupied and unoccupied state STM images. While the height of the downward-bent pyrrole groups of the O₂-MnTPP species show little difference with those of the MnTPP molecule, along the direction (CD) of the upward-bent pyrrole groups, a large increase is observed. The distance between the lobes of this structure ($\sim 7\text{\AA}$), extends well beyond the sum of the covalent radii of the dioxygen atoms ($\sim 1.49\text{\AA}$),⁵⁶ pointing to a considerable interaction of the upward-bent pyrrole groups with the Mn-dioxygen centre. So localized, this spatially resolved interaction can be expected to reflect the dioxygen coordination geometry.

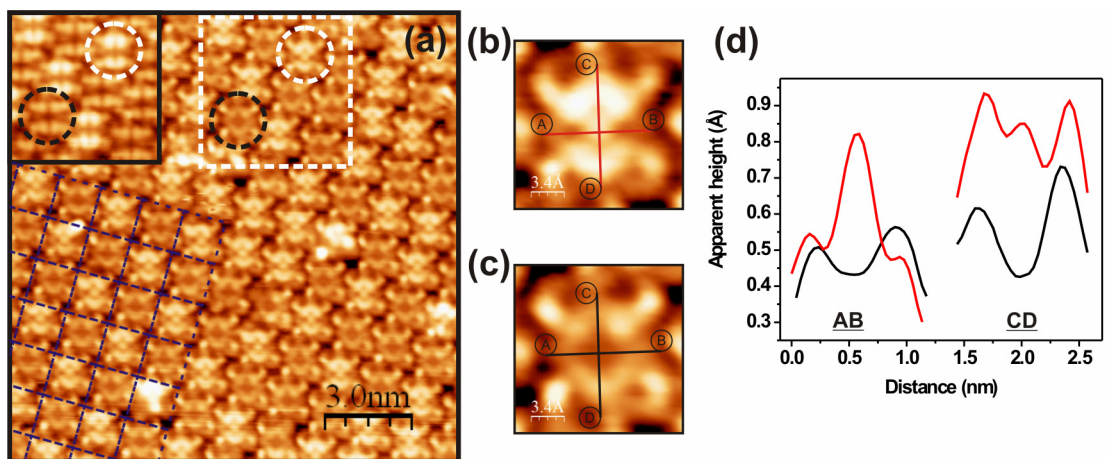
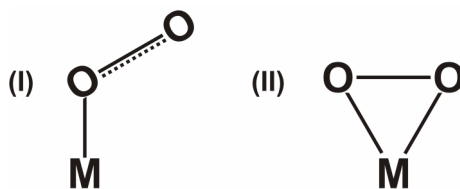


Figure 5.9. STM images obtained from the MnTPP monolayer on the Ag(111) surface following exposure to 7.0×10^4 L of molecular oxygen: (a) High resolution occupied state STM image; $V_{\text{sample}} = -1.20$ V, $I_t = 0.25$ nA, size $15 \text{ nm} \times 15 \text{ nm}$. A MnTPP and neighboring O_2 -MnTPP molecule are circled black and white, respectively. The inset shows the corresponding unoccupied state STM image of the region highlighted by the white dotted box; $V_{\text{sample}} = 1.20$ V, $I_t = 0.25$ nA, size $4.5 \text{ nm} \times 4.5 \text{ nm}$. (b) and (c) enlarged images of the highlighted MnTPP and O_2 -MnTPP molecules. (d) Height profiles taken along the lines of opposing pyrrole groups for the MnTPP (black) and O_2 -MnTPP (red) molecules (d).

Coordinated to a metalloporphyrin, it is found that the dioxygen ligand tends towards the formal valency of a superoxide (O_2^{-1}) or peroxide (O_2^{-2}) ion, exhibiting for each state a characteristic coordination geometry.⁵⁷ For dioxygen adducts of metalloporphyrins, it is typically found that superoxo- and peroxo-ligands are coordinated in the so-called end-on (I) and edge-on (II) geometries, respectively.^{50, 57, 58}



It is long established that manganous-porphyrins form peroxo-like complexes.^{50, 51, 59} In the case of the peroxo(tetraphenylporphyrinato)manganese(III) (Mn(III)TPP-O_2) anion, crystallographic characterization reveals that the peroxo-ligand is coordinated in the

symmetric edge-on geometry, whereby two of the manganese-pyrrole nitrogen bonds are eclipsed.⁶⁰ As mentioned above, the STM images of the O₂-MnTPP molecule (Fig. 5.9(b)) reveal a clear two-fold symmetry along the axis of opposing pyrrole groups; consistent only with the symmetric edge-on geometry. Therefore, it is proposed that the inter-nuclear axis of the dioxygen ligand is aligned parallel to the plane of the porphyrin macrocycle, eclipsing the axis of the upward-bent pyrrole nitrogens (see above). Thus, by analogy with other metal-dioxygen complexes where edge-on geometry is reported, a peroxo-like oxidation state is tentatively assigned to the dioxygen ligand of the present O₂-MnTPP molecule. Here it is mentioned that among the metalloporphyrins that form adducts with dioxygen, those of Fe⁶¹ and Co⁶² are found to bind dioxygen in the end-on geometry, while those of Mo⁵⁶ and Ti⁶³ show edge-on binding; in the latter case, the axis of opposing pyrrole nitrogens is also eclipsed.

In the case of the MnTPP molecules on the Ag(111) surface, the depression in the apparent height at the porphyrin core is found to be largely independent of the applied (± 2 V) bias-voltage. This has been attributed to a relatively minor contribution of the d_z² orbital of the central Mn atom to the frontier molecular orbitals (see Sec. 5.3.2). The apparent height of the O₂-MnTPP molecules, by contrast, displays pronounced bias-voltage dependence at the porphyrin core (Fig. 5.9 (a)). This is evidenced, as noted above, by a protrusion and depression at the porphyrin core when tunnelling from occupied and unoccupied states, respectively. Turning to the calculated MO structure of the closely related peroxo(porphyrinato)manganese (MnP-O₂) molecule, distinct differences are found in the contribution of the Mn d-orbitals to the frontier molecular orbitals.⁶⁴ Among the salient features, the HOMO is found to be predominantly of d_z² character, whereas the LUMO contains no contribution from d_z² orbital. Such a variation in the contribution of the d_z² orbital to the frontier molecular orbitals well describes the observed contrast inversion at the porphyrin core. Accordingly, it is proposed that the HOMO of the O₂-MnTPP molecules possess a larger contribution from the Mn d_z² orbital relative to the LUMO; thus giving rise to observed core protrusion and depression in occupied and unoccupied state STM images, respectively.

While it is found that most transition metal complexes form adducts with dioxygen,⁵⁷ they generally do so only when the central metal ion is present in a low valence

state⁵⁶. Given that the Mn(III) ion of the MnTPP molecule is of intermediate valence, the apparent formation of a peroxo-like complex is perhaps unexpected. However, for the present system, in the absence of solvent effects, the interaction at the molecule-substrate interface must be considered. From the crystallographic structure of closely related the Mn(III)TPP-O₂ anion,⁶⁰ the central Mn atom of the O₂-MnTPP molecule can be expected to be displaced from the average plane of the porphyrin macrocycle, towards the coordinated dioxygen ligand; thus precluding direct coupling of the Mn atom with the Ag(111) surface. On adsorption, however, it is found that both metallated- and free base-porphyrins (with or without meso-phenyl substituents) lower the work function of the Ag(111) surface.⁶⁵ This lowering of the work function has been attributed to the formation of an interface dipole, arising from the effects of Pauli repulsion.⁶⁶ Such a displacement of charge at the interface can be expected to influence the charge distribution of the metal surface and, moreover, the molecular adsorbate. For the MnP-O₂ molecule, the calculated charge distribution reveals that it is the porphine ring, more so than the Mn ion, that compensates for the charge density of the peroxo ligand.⁶⁴ Hence it is *speculated* that the adsorption of the MnTPP molecules on the Ag(111) surface induces, through the formation of an interface dipole, a redistribution of the charge density of the porphyrin ring; the effect of which is an increase in the affinity of the Mn center to undergo oxygenation.

In addition to the apparent “hopping” of the coordinated dioxygen to adjacent MnTPP molecules (Fig. 5.8 (c) to (e)), the distribution of the related dioxygen adducts is found to be distinctly non-random. The probability of observing different sets of configurations of n molecules out of a total N is expressed by the radial distribution function (RDF):

$$g(r) = N\rho^{-1} \sum_{i=1}^N \frac{n_i(r, dr)}{2\pi r dr} \quad (5.1)$$

where $n_i(r, dr)$ is the number of molecules in an annulus of width dr at a radius r from the i th molecule, and ρ is the average number density. In the case of the O₂-MnTPP molecules, however, the allowed configurations are explicitly defined by the MnTPP lattice. The configuration of the nearest-neighbours up to the eight-neighbour position for a molecule

located at the centre of the MnTPP lattice is illustrated in Figure 5.10(a). As a consequence, equation (5.1) may be written as:

$$g(r) = N\Theta^{-1} \sum_{i=1}^N \frac{n_i(j)}{m(j)} \quad (5.2)$$

where $n_i(j)$ is the number of j th-nearest-neighbour molecules surrounding the i th particle, $m(j)$ is the number of j th-neighbour sites and Θ is the surface coverage. It is noted that while equation (5.2) takes the form of a discrete probability function, due to the uncertainty of the measurement (discussed below), the neighbour sites identified from STM images are normally distributed about exact distances.

Calculation of the RDF for the O₂-MnTPP molecules was performed for a surface coverage of ~ 0.25 ML. For this purpose, the positions, as represented by a single pixel at the porphyrin core, of a set of MnTPP and O₂-MnTPP molecules (~ 1600) were identified. By way of explaining the findings of the RDF, the continuous “non-normalized” form, termed n.n-RDF, is first considered; here normalization refers to the division by $m(j)$ and Θ in equation (5.2). When evaluated for the set of overlayer molecules, both oxygenated and unoxxygenated, the n.n-RDF expresses the total number of molecules possessing nearest-neighbours at the j th-neighbour site. Hence, a comparison with the n.n-RDF of the set of O₂-MnTPP molecules reveals the j th-neighbour site occupation. Figure 5.10(b) shows the n.n-RDF of the set of all overlayer molecules and that of the O₂-MnTPP alone. The distribution curve of the overlayer molecules (black) yields eight main peaks, with separations corresponding to the discrete nearest-neighbour distances of the overlayer lattice. The widths of the peaks present in the n.n-RDF reflect the variance of the molecular positions, arising from the widths of the pixel (~ 0.08 nm) and porphyrin cores (~ 0.30 nm) mentioned above, and to a lesser extent on the thermal drift. As a consequence, the peaks of the fifth-, sixth- and seventh-neighbour sites partially overlap; this follows from their close proximity: $3 \times b_1$, $\sqrt{8} \times b_1$ and $\sqrt{10} \times b_1$, respectively (see Fig. 5.10(a)). The resulting best fit, yields areas which are in agreement with the expected ratios of the j th-neighbour sites for the square overlayer lattice; the number of nearest-neighbours at the fourth-, seventh- and eight-neighbour sites are approximately twice that of the remaining five. In like manner,

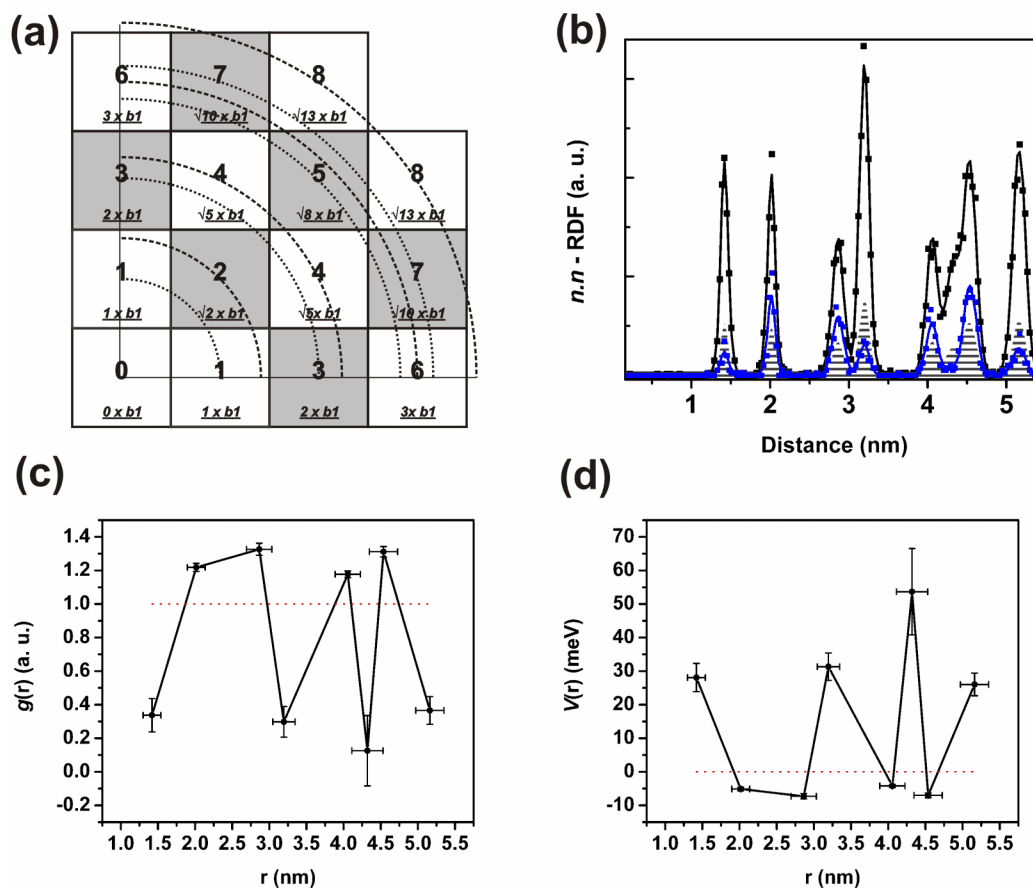


Figure 5.10. (a) Configuration of the j th-nearest-neighbours for a quadrant of a square lattice. The distances from the zero- up to the eight-neighbour position, for a molecule located at the centre of the square MnTPP lattice, are shown underlined. The higher probability neighbour sites are shaded. (b) Radial distribution of the set of all molecules (black), and that of the O₂-MnTPP species (blue) at a coverage of 0.25 ML. The horizontal lines trace the expected (random) distribution of the O₂-MnTPP species. (c) and (d) RDF and PMF, respectively, of the O₂-MnTPP molecules evaluated from the first- to eight-neighbour positions; divergence from the dotted horizontal lines indicates a non-random distribution.

eight peaks are observed in the distribution curve of the O₂-MnTPP molecules (blue), though of smaller areas, commensurate with the lower surface coverage (0.25 ML). Horizontal lines (grey) trace the expected distribution for the overlayer molecules at the lower coverage. From the O₂-MnTPP distribution curve, it is clear that peak areas deviate markedly from that expected. Figure 5.10(c) shows the RDF of the O₂-MnTPP molecules

evaluated from the first- to eight-neighbour positions; here the discrete probability function takes as its input the mean positions of the normally distributed j th-neighbour sites. It is found that the second-, third-, fifth- and seventh-neighbour sites have a greater than average probability of being occupied, whilst that of the first, fourth, sixth and eight have lower probability. This is illustrated in Fig. 5.10(a), where the higher probability neighbour sites are shaded grey; thus producing a clear $(\sqrt{2} \times \sqrt{2})R45^\circ$ pattern. Indeed such a $(\sqrt{2} \times \sqrt{2})R45^\circ$ overlayer structure (highlighted by a dotted grid) can be observed in Fig.5.9(a), where the O_2 -MnTPP molecules are present at a coverage of ~ 0.5 ML. Notably, this is the same structure for which the MnTPP lattice is found to approach a coincident registry with that of the substrate. It follows that the formation of the dioxygen adduct may be more favourable at MnTPP molecules adsorbed on certain substrate sites.

The imaged dioxygen adducts are stable over the period of the (line) scan: on the order of a millisecond. Thus the influence of the STM tip on the apparent movement of the coordinated dioxygen is ostensibly less than the interaction potentials of the j th-neighbour sites. The probabilities expressed by the RDF, are related to the interaction potentials of the j th-neighbour sites by the potential of mean force (PMF):

$$V(r) = -kT \ln g(r) \quad (5.3)$$

where k is the Boltzmann constant, and T is the temperature. Here, the PMF describes the interaction potential of an O_2 -MnTPP molecule, one of n at the j th-neighbour site, with the remaining $n + 1, \dots, N$ molecules, averaged over all configurations of the latter. For the calculation of the PMF of the O_2 -MnTPP molecules, the surface coverage of ~ 0.25 ML was considered. Figure 5.10(d) shows the PMF of the O_2 -MnTPP molecules evaluated from the first- to eight-neighbour positions. It is found that the lower probability neighbour sites display comparable interaction potentials (28 ± 3 meV), save for that of the sixth-neighbour site which, within the margin of the uncertainty, is almost twice as repulsive. The interaction potentials of the higher probability neighbour sites are also close in energy, but by comparison are found to be weakly attractive (-6 ± 2 meV). The interaction energies of the lower probability neighbour sites are on the order of the thermal energy at room temperature ($kT = 25$ meV); whereas, those of the higher probability are approximately a

factor of four weaker. Thus while movement of the coordinated dioxygen, relative to a given dioxygen adduct, may take place at the lower probability neighbour sites, it is more likely to occur at those of higher probability.

As the dioxygen adduct approaches monolayer coverage, a molecular rearrangement occurs. Figure 5.11(a) shows an occupied state STM image of the MnTPP monolayer following exposure to 1.7×10^5 L of molecular oxygen. Along with the square lattice (domain I), previously observed for the MnTPP overlayer, a hitherto unseen molecular arrangement is obtained (domains II and III). It is found that the molecules of this latent phase are laterally rearranged, whereby, along a row, the principal molecular axes of adjacent molecules are aligned at an angle of $\sim 45^\circ$; distinctly different to the parallel alignment of molecules in the square lattice. The inset shows an enlarged view, in which the molecular ordering is highlighted by superimposed TPP models. These molecular rows (indicated by lines *b* and *c*) are found to be orientated at $\sim 120^\circ$ relative to the direction of one of the primitive lattice vectors of the initial square phase (line *a*); hence, they follow symmetrically equivalent substrate directions. This corresponds to an azimuthal rotation of $\sim 15^\circ$ relative to the $\langle \bar{1}10 \rangle$ substrate closed packed directions.

A surface region of the latent phase, obtained at the above molecular oxygen exposure, is shown in Figure 5.11(b). Variation in the stacking sequence of the molecular rows is found to produce two distinct lattices - of short range order - defined by rectangular and oblique primitive unit cells, as shown in the lower and upper parts of Fig. 5.11(b), respectively. By relation to the known registry of the square overlayer lattice with the Ag(111) substrate (see Sec. 5.3.1), that of the coexisting rectangular and oblique lattices may be determined. It is found that the principal lattice vectors of the rectangular (c_1) and oblique (d_1) phases show an azimuthal rotation of $\sim 15^\circ$ relative to substrate closed packed directions. This follows directly from the stated orientation of the molecular rows, along which, the principal lattice vectors are aligned (Fig. 5.11(b)). In like manner, the azimuthal orientation of the individual molecules within the rows, may be directly related to corresponding directions on the Ag(111) surface. The principal molecular axes of adjacent molecules, alternating at $\sim 45^\circ$ to each other, produce two distinct sets of orientations relative to the direction of the molecular row. Of the first set of molecules, one of the molecular axes is aligned parallel to the molecular row, the other at $\sim 90^\circ$, corresponding to

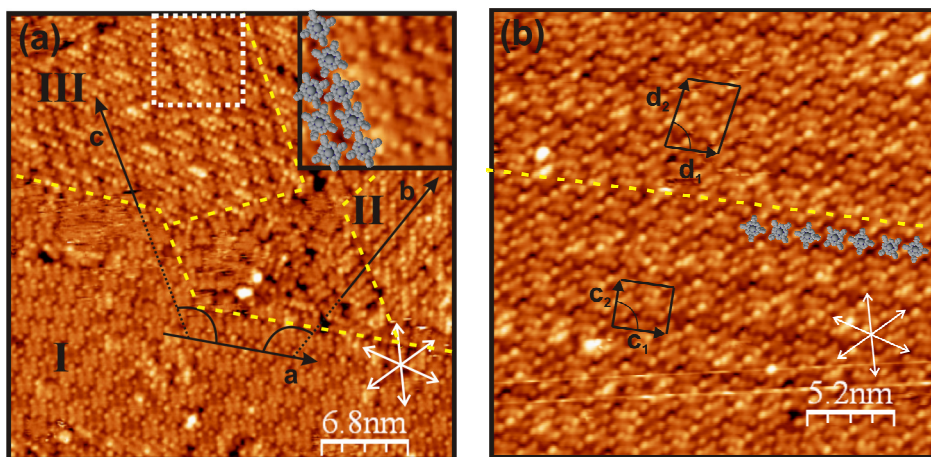


Figure 5.11. STM images obtained from the MnTPP monolayer on the Ag(111) surface following exposure to 1.7×10^5 L of molecular oxygen. The close-packed directions of the Ag(111) surface are indicated by white arrows; dashed yellow lines mark domain boundaries. (a) Large-scale occupied state STM image; $V_{\text{sample}} = -1.25$ V, $I_t = 0.20$ nA, size $35 \text{ nm} \times 35 \text{ nm}$. The indicated domains show the square (I) and latent phases (II, III); the black arrows indicate molecular row directions in the different domains. The inset shows an enlarged view of the region highlighted by the white dotted box; the models highlight the orientations of molecules along a row. (b) Occupied state STM image of the latent phase; $V_{\text{sample}} = -1.25$ V, $I_t = 0.20$ nA, size $25 \text{ nm} \times 25 \text{ nm}$. The primitive lattice vectors of the rectangular (c_1 , c_2) and oblique (d_1 , d_2) unit cells are shown in black.

an alignment with the $\langle 3\bar{4}1 \rangle$ and $\langle 31\bar{4} \rangle$ crystallographic directions, respectively. In turn, the molecular axes of the second set, at $\sim 45^\circ$ to this first, follow the $\langle 0\bar{1}1 \rangle$ and $\langle \bar{2}11 \rangle$ high symmetry directions; notably, the same azimuthal orientation displayed by molecules of the square phase.

From the alternate orientations of the latent phase molecules, different configurations of adjacent phenyl groups arise. Figure 12 (b) to (d) show the molecular arrangements for the observed overlayer lattices. The corresponding configurations of adjacent phenyl groups are illustrated (by the analogous benzene dimers) in Figure 12(a): the so-called parallel stacked (1), the edge-to-face T-shaped (2) and tilted-T (3) structures. For molecules of the square phase, a T-shape configuration is exclusively observed. This is also found to be the case for molecules of the latent phases which are orientated at $\sim 45^\circ$ to the molecular row direction, i.e. the same azimuthal orientation as the square phase. By

contrast, a parallel stacked arrangement is observed for molecules aligned parallel to the molecular row direction. Between molecular rows, the phenyl groups of adjacent molecules of different azimuthal orientations display a tilted-T configuration; while along the row, a here termed, titled-T displaced arrangement is found. Interestingly, while the rectangular and oblique phases show the same phenyl-phenyl geometries, the molecules aligned parallel to the molecular row possess different symmetries; namely, C_s in the former phase and C_2 in the latter. Of the benzene dimer geometries mentioned, it is the edge-to-face T-shape configuration which is reported as the energy minimum.²⁵ An earlier study of the aromatic-aromatic interactions of liquid benzene found that the T-shape configuration is ~ 30 meV lower in energy than the parallel stacked form.⁶⁷ On this basis, it follows that the phenyl-phenyl geometries of the latent phases represent a higher energy arrangement.

It is evident that the observed molecular rearrangement and the associated phenyl-phenyl geometries are induced by the exposure of the MnTPP overlayer to molecular oxygen. A recent study on the exposure of CoTPP on Ag(111) to nitrogen monoxide (NO) also reported a rearrangement of the initially square overlayer lattice.¹⁸ Here, the axial coordination of NO to the CoTPP complex was found to occur at much lower exposures (than rearrangement) and an increase in the unit cell size was observed with increasing exposure. It was concluded, therefore, that the NO coadsorbed between the CoTPP molecules, directly on the Ag(111) substrate. In the present case, however, the molecular rearrangement and axial coordination of the dioxygen ligand to central Mn atom occur together. Furthermore, while the primitive unit cells of the latent phases are larger than the initial square phase, it is noted that the corresponding molecular number densities differ by less than 2%. It follows that the observed lateral rearrangement of the MnTPP molecules results directly from the formation of the dioxygen adduct.

From the RDF of the O_2 -MnTPP molecules (see above) a higher probability for a $(\sqrt{2} \times \sqrt{2})R45^\circ$ overlayer structure is found. Hence, at coverages above 0.5 ML, occupation of the (initially) lower probability neighbour sites takes place. The apparent absence of the molecular rearrangement for O_2 -MnTPP coverages below 0.5 ML suggests, therefore, that the rearrangement might be induced by the occupation of the lower probability neighbour sites. The lateral intermolecular interaction by which the molecular assembly arises can be expected to be strongly influenced by the configuration of adjacent phenyl groups.²⁴⁻²⁶

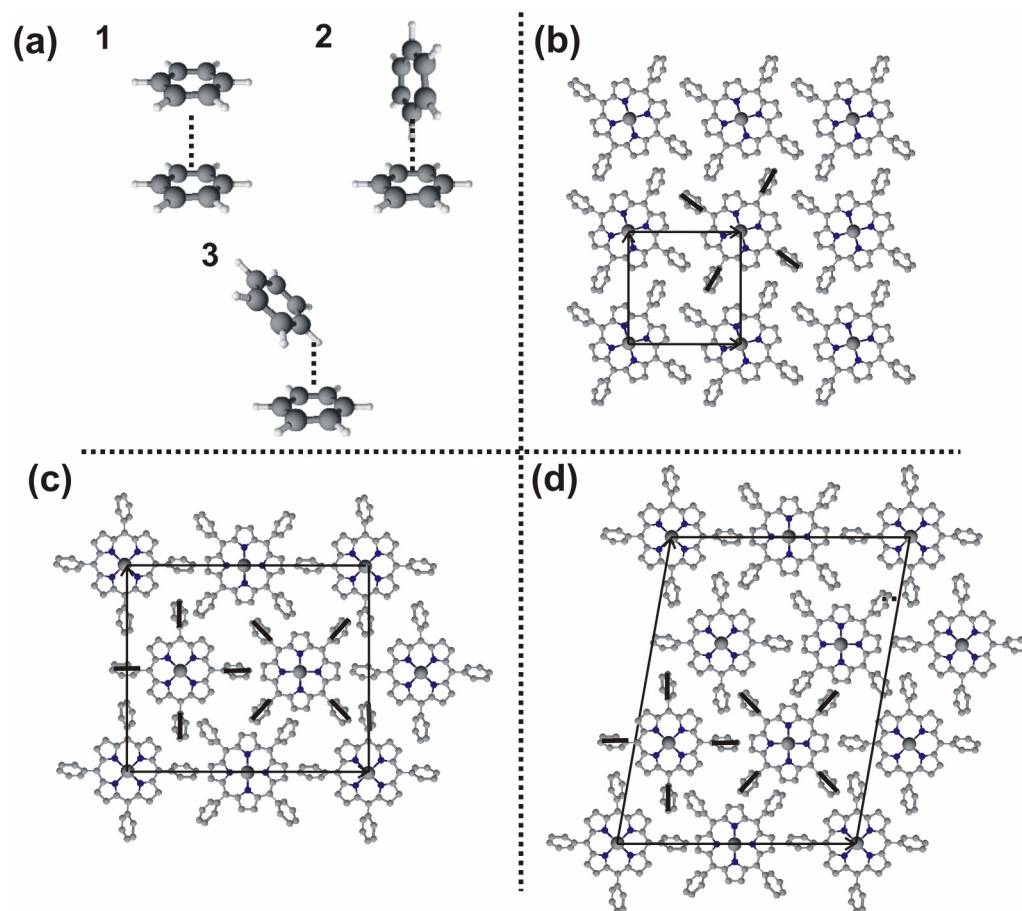


Figure 5.12. (a) Benzene dimer configurations: the so-called parallel stacked (1), edge-to-face T-shaped (2), and tilted-T (3) structures. Molecular arrangements and phenyl-phenyl geometries for the observed overlay lattices; (b) square, (c) rectangular and (d) oblique.

Here, it is noted that the energy difference between the higher and lower probability neighbour sites (~ 34 meV), is on the order of that reported (~ 30 meV) for the T-shape and paralleled stacked arrangement (in liquid benzene) of the benzene dimer.⁶⁷ As such, it is plausible that the distribution of the dioxygen adducts, as reflected by the RDF, is influenced by the configuration of adjacent phenyl groups.

5.3.4. Controlling axial coordination: thermal lability and the presence of the axial Cl ligand

The coordinated dioxygen ligand of the O₂-MnTPP molecules is found to be thermally labile. By annealing to 423 K (for ~ 1 hour), the complete deoxygenation of the O₂-MnTPP molecules for coverage approaching that of a monolayer is observed. This is evidenced in STM images by a transition from the oxygenated molecular profile, to that solely of the MnTPP precursor. A slight reduction in the molecular coverage (< 0.1 ML) is observed following annealing of the exposed surface, likely arising from the loose molecular packing seen at domain boundaries (Fig. 5.11(a)). The MnTPP molecules, following the deoxygenation, are found to be quadrilaterally arranged; the latent phase molecular arrangements are not observed. Thus, the oxygenation of the MnTPP molecules is reversible, with the molecular monolayer behaving as a so-called oxygen carrier. In addition, exposure of the deoxygenated MnTPP overlayer to molecular oxygen was found to result in the formation of the O₂-MnTPP species once again. This was established, however, only for limited molecular oxygen exposure. Such thermal lability has previously been reported for the (solid state) dioxygen adduct of oxo(5,10,15,20-tetramesitylporphyrinato)molybdenum(IV) (Appendix, Figure 13); wherein, peak liberation of the coordinated dioxygen is noted to occur at 349.2 K.⁶⁸

The oxygenation of the deposited Cl-MnTPP molecules, with exposure to molecular oxygen, is found to be self-limited. Figure 5.2(b) (Sec. 5.3.1) shows a typical occupied state STM image of the deposited Cl-MnTPP molecules on the Ag(111) surface at monolayer coverage. For the present deposition conditions, the C 1s and Cl 2p XPS spectra (Sec. 5.3.2), yield a C/Cl atomic ratio of 44 : 0.8 (± 0.3), consistent with a partial loss of the axial Cl ligand. It is apparent, however, that the Cl-MnTPP and MnTPP molecules are observed with the same molecular profile - for the given applied bias-voltages. Following exposure of the deposited Cl-MnTPP monolayer to ~ 7.0 x 10⁴ L of molecular oxygen, an O₂-MnTPP coverage of ~ 0.2 ML is observed. This is considerably less than that expected (~ 0.5 ML) for exposure of the MnTPP monolayer. Figure 5.13(b) shows an occupied state STM image of the deposited Cl-MnTPP monolayer following exposure ~ 1.5 x 10⁵ L of molecular oxygen. On this doubling of the molecular oxygen exposure, it is found that the fractional

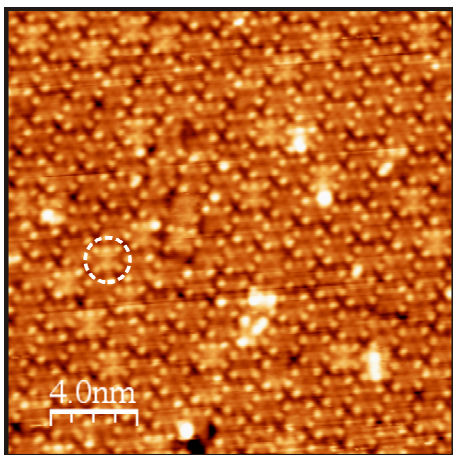


Figure 5.13. Occupied state STM image obtained from the Cl-MnTPP monolayer on the Ag(111) surface following exposure to $\sim 1.5 \times 10^5$ L of molecular oxygen; $V_{\text{sample}} = -1.20$ V, $I_t = 0.25$ nA, size 20 nm \times 20 nm. A O₂-MnTPP molecule is circled.

coverage of the molecules (for a set > 1000) which are oxygenated ($\sim 0.2\text{ML}$) remains unchanged. The fraction of the deposited Cl-MnTPP molecules which undergo oxygenation is approximately equal, within the uncertainty, to that which seemingly lose the Cl ligand at deposition. It follows that the presence of the axial Cl ligand inhibits the coordination of the dioxygen ligand.

Accordingly, the observed self-limited oxygenation confirms the presence of two chemically distinct species; despite the apparent similarity of the MnTPP molecules on the Ag(111) surface with or without the axial Cl ligand. A recent study of the Cl-MnTPP complex on metallic and oxygen-covered Co(001) substrates reveals a striking dependence of the molecular profile (observed in occupied state STM images) on the oxidation state of the central Mn atom.⁶⁹ On the Co(001) surface, the Mn atom of the adsorbed Cl-MnTPP molecules is found to exist predominantly in a +3 oxidation state. Corresponding STM images of the Mn(III) d^4 complex reveal a characteristic depression in the apparent core height - as found in the present work. Following adsorption of the Cl-MnTPP molecules on the oxygen-covered Co(001) substrate, however, the central Mn atom is found to principally exist in a +2 oxidation state. Notably, arising from the reduced oxidation state of the Mn(II) d^5 complex, a distinctive protrusion in the apparent height at the porphyrin core is revealed.

5.4. Summary

The conformation, thermal lability and oxygenation of Cl-MnTPP molecules on the Ag(111) surface, have been investigated using STM, LEED and XPS. The Cl-MnTPP molecules are found to self-assemble on Ag(111) surface at room-temperature, forming an ordered molecular overlayer described by a square unit cell. The axial Cl ligand is found to be orientated away from the Ag(111) surface, whereby the average plane of the porphyrin macrocycle lies parallel to that of the substrate. When adsorbed on the Ag(111) surface, the Cl-MnTPP molecules display a latent thermal lability resulting in the dissociation of the axial Cl ligand at ~ 423 K. The thermally induced dissociation of the Cl ligand leaves the porphyrin complex otherwise intact, giving rise to the coordinatively unsaturated Mn(III) derivative. Upon exposure of the MnTPP molecules to molecular oxygen, a dioxygen adduct is formed. The dioxygen ligand is found to be coordinated to the central Mn atom in a symmetric egde-on geometry. The radial distribution of the dioxygen adducts is distinctly non-random, with a higher probability for a $(\sqrt{2} \times \sqrt{2})R45^\circ$ overlayer structure observed. As the dioxygen adduct approaches monolayer coverage, a molecular rearrangement occurs, whereby, along a row, the principal molecular axes of adjacent molecules are aligned at an angle of $\sim 45^\circ$. The dioxygen adduct is found to be thermally labile, with deoxygenation brought about by annealing to 423 K. Subsequent exposure of the deoxygenated MnTPP overlayer to molecular oxygen gives rise to the dioxygen adduct once more. A fraction of the deposited Cl-MnTPP molecules, equal to the number which lose the axial Cl ligand at deposition, undergo oxygenation. The formation of an adduct between dioxygen and the Cl-MnTPP molecules is not observed.

5.5. References

- (1) Meunier, B. Metalloporphyrins as versatile catalysts for oxidation reactions and oxidative DNA cleavage. *Chem. Rev.* **1992**, 92, 1411-1456.
- (2) Rose, E.; Andrioletti, B.; Zrig, S.; Quelquejeu-Ehteve, M. Enantioselective epoxidation of olefins with chiral metalloporphyrin catalysts. *Chem. Soc. Rev.* **2005**, 34, 573-583.

- (3) Traylor, T. G.; Miksztal, A. R. Alkene epoxidations catalyzed by iron(III), manganese(III), and chromium(III) porphyrins - effects of metal and porphyrin substituents on selectivity and regiochemistry of epoxidation. *J. Am. Chem. Soc.* **1989**, *111*, 7443-7448.
- (4) Merlau, M.; Grande, W.; Nguyen, S.; Hupp, J. Enhanced activity of manganese(III) porphyrin epoxidation catalysts through supramolecular complexation. *J. Mol. Catal. A: Chem.* **2000**, *156*, 79-84.
- (5) Haber, J.; Matachowski, L.; Pamin, K.; Poltowicz, J. Supported polyhalogenated metalloporphyrins as catalysts for the oxidation of cycloalkanes with molecular oxygen in Lyons system. *Catal. Today* **2004**, *91-2*, 195-198.
- (6) Gottfried, J. M.; Marbach, H. Surface-confined coordination chemistry with porphyrins and phthalocyanines: aspects of formation, electronic structure, and reactivity. *Z. Phys. Chem.* **2009**, *223*, 53-74.
- (7) K. M. Kadish; K. M. Schmith; R. Guilard, (Eds.). (2000) *The porphyrin handbook, applications: past, present and future*, Vol. 6. Academic Press: San Diego.
- (8) Groves, J. T.; Kruper, W. J.; Haushalter, R. C. Hydrocarbon oxidations with oxometalloporphyrins - isolation and reactions of a (porphinato)manganese(V) complex. *J. Am. Chem. Soc.* **1980**, *102*, 6375-6377.
- (9) Liu, W.; Groves, J. T. Manganese Porphyrins Catalyze Selective C-H Bond Halogenations. *J. Am. Chem. Soc.* **2010**, *132*, 12847-12849.
- (10) Liu, W.; Huang, X.; Cheng, M.; Nielsen, R. J.; Goddard, W. A.; Groves, J. T. Oxidative aliphatic C-H fluorination with fluoride ion catalyzed by a manganese porphyrin. *Science* **2012**, *337*, 1322-1325.
- (11) Groves, J. T.; Stern, M. K. Olefin epoxidation by manganese(IV) porphyrins - evidence for 2 reaction pathways. *J. Am. Chem. Soc.* **1987**, *109*, 3812-3814.
- (12) Srour, H.; Le Maux, P.; Simonneaux, G. Enantioselective manganese-porphyrin-catalyzed epoxidation and C-H hydroxylation with hydrogen peroxide in water/methanol solutions. *Inorg. Chem.* **2012**, *51*, 5850-5856.
- (13) Hulsken, B.; Van Hameren, R.; Gerritsen, J. W.; Khoury, T.; Thordarson, P.; Crossley, M. J.; Rowan, A. E.; Nolte, R. J. M.; Elemans, J. A. A. W.; Speller, S. Real-time single molecule imaging of oxidation catalysis at a liquid-solid interface. *Nat. Nanotechnol.* **2007**, *2*, 285-289.

- (14) Boucher, L. J. Manganese Porphyrin Complexes .5. Axial interactions in manganese(III) porphyrins. *Ann. N. Y. Acad. Sci.* **1973**, *206*, 409-419.
- (15) Lyons, J. E.; Ellis, P. E.; Myers, H. K. Halogenated metalloporphyrin complexes as catalysts for selective reactions of acyclic alkanes with molecular-oxygen. *J. Catal.* **1995**, *155*, 59-73.
- (16) Haber, J.; Matachowski, L.; Pamin, K.; Poltowicz, J. Manganese porphyrins as catalysts for oxidation of cyclooctane in Lyons system. *J. Mol. Catal. A: Chem.* **2000**, *162*, 105-109.
- (17) Haber, J.; Matachowski, L.; Pamin, K.; Poltowicz, J. The effect of peripheral substituents in metalloporphyrins on their catalytic activity in Lyons system. *J. Mol. Catal. A: Chem.* **2003**, *198*, 215-221.
- (18) Buchner, F.; Seufert, K.; Auwaerter, W.; Heim, D.; Barth, J. V.; Flechtner, K.; Gottfried, J. M.; Steinrueck, H.; Marbach, H. NO-induced reorganization of porphyrin arrays. *Acs Nano* **2009**, *3*, 1789-1794.
- (19) Horcas, I.; Fernandez, R.; Gomez-Rodriguez, J. M.; Colchero, J.; Gomez-Herrero, J.; Baro, A. M. WSXM: A software for scanning probe microscopy and a tool for nanotechnology. *Rev. Sci. Instrum.* **2007**, *78*, 013705.
- (20) Adler, A. D.; Longo, F. R.; Kampas, F.; Kim, J. On preparation of metalloporphyrins. *J. Inorg. Nucl. Chem.* **1970**, *32*, 2443-2445.
- (21) Auwaerter, W.; Seufert, K.; Klappenberger, F.; Reichert, J.; Weber-Bargioni, A.; Verdini, A.; Cvetko, D.; Dell'Angela, M.; Floreano, L.; Cossaro, A.; Bavdek, G.; Morgante, A.; Seitsonen, A. P.; Barth, J. V. Site-specific electronic and geometric interface structure of Co-tetraphenyl-porphyrin layers on Ag(111). *Phys.Rev.B* **2010**, *81*, 245403.
- (22) Comanici, K.; Buchner, F.; Flechtner, K.; Lukasczyk, T.; Gottfried, J. M.; Steinrueck, H.; Marbach, H. Understanding the contrast mechanism in scanning tunneling microscopy (STM) images of an intermixed tetraphenylporphyrin layer on Ag(111). *Langmuir* **2008**, *24*, 1897-1901.
- (23) Scudiero, L.; Barlow, D. E.; Hipps, K. W. Physical properties and metal ion specific scanning tunneling microscopy images of metal(II) tetraphenylporphyrins deposited from vapor onto gold (111). *J Phys Chem B* **2000**, *104*, 11899-11905.

- (24) Buchner, F.; Kellner, I.; Hieringer, W.; Goerling, A.; Steinrueck, H.; Marbach, H. Ordering aspects and intramolecular conformation of tetraphenylporphyrins on Ag(111). *Phys. Chem. Chem. Phys* **2010**, *12*, 13082-13090.
- (25) Jennings, W. B.; Farrell, B. M.; Malone, J. F. Attractive intramolecular edge-to-face aromatic interactions in flexible organic molecules. *Acc. Chem. Res.* **2001**, *34*, 885-894.
- (26) Brede, J.; Linares, M.; Kuck, S.; Schwoebel, J.; Scarfato, A.; Chang, S.; Hoffmann, G.; Wiesendanger, R.; Lensen, R.; Kouwer, P. H. J.; Hoogboom, J.; Rowan, A. E.; Broering, M.; Funk, M.; Stafstrom, S.; Zerbetto, F.; Lazzaroni, R. Dynamics of molecular self-ordering in tetraphenyl porphyrin monolayers on metallic substrates. *Nanotechnology* **2009**, *20*, 275602.
- (27) Tulinsky, A.; Chen, B. M. L. Crystal and Molecular-Structure of Chloro-Alpha,beta,gamma,delta - tetraphenylporphinatomanganese(III). *J. Am. Chem. Soc.* **1977**, *99*, 3647-3651.
- (28) Vanatta, R. B.; Strouse, C. E.; Hanson, L. K.; Valentine, J. S. [peroxotetraphenylporphinato]manganese(III) and [chlorotetraphenylporphinato]manganese(II) anions - syntheses, crystal-structures, and electronic-structures. *J. Am. Chem. Soc.* **1987**, *109*, 1425-1434.
- (29) Iancu, V.; Deshpande, A.; Hla, S. W. Manipulating Kondo temperature via single molecule switching. *Nano Lett.* **2006**, *6*, 820-823.
- (30) Curet-Arana, M. C.; Emberger, G. A.; Broadbelt, L. J.; Snurr, R. Q. Quantum chemical determination of stable intermediates for alkene epoxidation with Mn-porphyrin catalysts. *J. Mol. Catal. A: Chem.* **2008**, *285*, 120-127.
- (31) Hooks, D. E.; Fritz, T.; Ward, M. D. Epitaxy and molecular organization on solid substrates. *Adv Mater* **2001**, *13*, 227-248.
- (32) Lambert, R. M.; Cropley, R. L.; Husain, A.; Tikhov, M. S. Halogen-induced selectivity in heterogeneous epoxidation is an electronic effect - fluorine, chlorine, bromine and iodine in the Ag-catalysed selective oxidation of ethene. *Chem. Commun.* **2003**, 1184-1185.

- (33) Turner, M.; Vaughan, O. P. H.; Kynakou, G.; Watson, D. J.; Scherer, L. J.; Papageorgiou, A. C.; Sanders, J. K. M.; Lambert, R. M. Deprotection, tethering, and activation of a one-legged metalloporphyrin on a chemically active metal surface: NEXAFS, synchrotron XPS, and STM study of [SAc]P-Mn(III)Cl on Ag(100). *J. Am. Chem. Soc.* **2009**, *131*, 14913-14919.
- (34) Turner, M.; Vaughan, O. P. H.; Kyriakou, G.; Watson, D. J.; Scherer, L. J.; Davidson, G. J. E.; Sanders, J. K. M.; Lambert, R. M. Deprotection, tethering, and activation of a catalytically active metalloporphyrin to a chemically active metal surface: [SAc](4)P-Mn(III)Cl on Ag(100). *J. Am. Chem. Soc.* **2009**, *131*, 1910-1914.
- (35) Nardi, M.; Verucchi, R.; Corradi, C.; Pola, M.; Casarin, M.; Vittadini, A.; Iannotta, S. Tetraphenylporphyrin electronic properties: a combined theoretical and experimental study of thin films deposited by SuMBD. *Phys. Chem. Chem. Phys.* **2010**, *12*, 871-880.
- (36) Buchner, F.; Flechtner, K.; Bai, Y.; Zillner, E.; Kellner, I.; Steinrueck, H.; Marbach, H.; Gottfried, J. M. Coordination of iron atoms by tetraphenylporphyrin monolayers and multilayers on Ag(111) and formation of iron-tetraphenylporphyrin. *J. Phys. Chem. C* **2008**, *112*, 15458-15465.
- (37) Lukasczyk, T.; Flechtner, K.; Merte, L. R.; Jux, N.; Maier, F.; Gottfried, J. M.; Steinrueck, H. Interaction of cobalt(II) tetraarylporphyrins with a Ag(111) surface studied with photoelectron spectroscopy. *J. Phys. Chem. C* **2007**, *111*, 3090-3098.
- (38) Kretschmann, A.; Walz, M.; Flechtner, K.; Steinrueck, H.; Gottfried, J. M. Tetraphenylporphyrin picks up zinc atoms from a silver surface. *Chem. Commun.* **2007**, 568-570.
- (39) Di Santo, G.; Blankenburg, S.; Castellarin-Cudia, C.; Fanetti, M.; Borghetti, P.; Sangaletti, L.; Floreano, L.; Verdini, A.; Magnano, E.; Bondino, F.; Pignedoli, C. A.; Manh-Thuong Nguyen; Gaspari, R.; Passerone, D.; Goldoni, A. Supramolecular engineering through temperature-induced chemical modification of 2H-tetraphenylporphyrin on Ag(111): flat phenyl conformation and possible dehydrogenation reactions. *Chem. Eur. J.* **2011**, *17*, 14354-14359.
- (40) Gupta, R. P.; Sen, S. K. Calculation of multiplet structure of core p-vacancy levels. 2. *Phys.Rev.B* **1975**, *12*, 15-19.

- (41) Nesbitt, H. W.; Banerjee, D. Interpretation of XPS Mn(2p) spectra of Mn oxyhydroxides and constraints on the mechanism of MnO₂ precipitation. *Am. Mineral.* **1998**, *83*, 305-315.
- (42) Petraki, F.; Peisert, H.; Biswas, I.; Chasse, T. Electronic structure of Co-phthalocyanine on gold investigated by photoexcited electron spectroscopies: indication of Co ion-metal interaction. *J. Phys. Chem. C* **2010**, *114*, 17638-17643.
- (43) Boucher, L. J. Manganese porphyrin complexes. *Coord. Chem. Rev.* **1972**, *7*, 289-329.
- (44) Lu, X.; Hipps, K. W.; Wang, X. D.; Mazur, U. Scanning tunneling microscopy of metal phthalocyanines: d(7) and d(9) cases. *J. Am. Chem. Soc.* **1996**, *118*, 7197-7202.
- (45) Muellegger, S.; Schoefberger, W.; Rashidi, M.; Reith, L. M.; Koch, R. Spectroscopic STM studies of single gold(III) porphyrin molecules. *J. Am. Chem. Soc.* **2009**, *131*, 17740-17741.
- (46) Teugels, L. G.; Avila-Bront, L. G.; Sibener, S. J. Chiral domains achieved by surface adsorption of achiral nickel tetraphenyl- or octaethylporphyrin on smooth and locally kinked Au(111). *J. Phys. Chem. C* **2011**, *115*, 2826-2834.
- (47) Rosa, A.; Ricciardi, G.; Baerends, E. J. Synergism of porphyrin-core saddling and twisting of meso-aryl substituents. *J. Phys. Chem. A* **2006**, *110*, 5180-5190.
- (48) Buchner, F.; Comanici, K.; Jux, N.; Steinrueck, H.; Marbach, H. Polymorphism of porphyrin molecules on Ag(111) and how to weave a rigid monolayer. *J. Phys. Chem. C* **2007**, *111*, 13531-13538.
- (49) Auwarter, W.; Weber-Bargioni, A.; Riemann, A.; Schiffrin, A.; Groning, O.; Fasel, R.; Barth, J. V. Self-assembly and conformation of tetrapyridyl-porphyrin molecules on Ag(111). *J. Chem. Phys.* **2006**, *124*, 194708.
- (50) Hoffman, B. M.; Weschler, C. J.; Basolo, F. Dioxygen adduct of meso-tetraphenylporphyrinmanganese(II), a synthetic oxygen carrier. *J. Am. Chem. Soc.* **1976**, *98*, 5473-5482.
- (51) Jones, R. D.; Summerville, D. A.; Basolo, F. Manganese(II) porphyrin oxygen carriers - equilibrium-constants for reaction of dioxygen with para-substituted meso-tetraphenylporphyrinmanganese(II) complexes. *J. Am. Chem. Soc.* **1978**, *100*, 4416-4424.

- (52) Watanabe, T.; Ama, T.; Nakamoto, K. Matrix-isolation infrared-Spectra of (octaethylporphyrinato)manganese(II) and (phthalocyaninato)manganese(II) and their dioxygen Adducts. *Inorg. Chem.* **1983**, *22*, 2470-2472.
- (53) Lever, A. B. P.; Wilshire, J. P.; Quan, S. K. Manganese phthalocyanine-dioxygen molecular adduct. *J. Am. Chem. Soc.* **1979**, *101*, 3668-3669.
- (54) Moxon, N. T.; Fielding, P. E.; Gregson, A. K. Manganese 4,4',4'',4'''-tetrasulfonated phthalocyanine, its dioxygen adduct, and electron-spin-resonance evidence for intramolecular electron-transfer in solution. *J. Chem. Soc., Chem. Commun.* **1981**, 98-99.
- (55) Dismukes, G. C.; Sheats, J. E.; Smegal, J. A. Mn²⁺/Mn³⁺ and Mn³⁺/Mn⁴⁺ mixed-valence binuclear manganese complexes of biological interest. *J. Am. Chem. Soc.* **1987**, *109*, 7202-7203.
- (56) Jones, R. D.; Summerville, D. A.; Basolo, F. Synthetic oxygen carriers related to biological-systems. *Chem. Rev.* **1979**, *79*, 139-179.
- (57) Vaska, L. Dioxygen-metal complexes - toward a unified view. *Acc. Chem. Res.* **1976**, *9*, 175-183.
- (58) Collman, J. P.; Brauman, J. I.; Rose, E.; Suslick, K. S. Cooperativity in O₂ binding to iron porphyrins. *Proc. Natl. Acad. Sci. U. S. A.* **1978**, *75*, 1052-1055.
- (59) Weschler, C. J.; Hoffman, B. M.; Basolo, F. Synthetic oxygen carrier - dioxygen adduct of a manganese porphyrin. *J. Am. Chem. Soc.* **1975**, *97*, 5278-5280.
- (60) Vanatta, R. B.; Strouse, C. E.; Hanson, L. K.; Valentine, J. S. [peroxotetraphenylporphinato]manganese(III) and [chlorotetraphenylporphinato]manganese(II) anions - syntheses, crystal-structures, and electronic-structures. *J. Am. Chem. Soc.* **1987**, *109*, 1425-1434.
- (61) Collman, J. P.; Gagne, R. R.; Reed, C. A.; Robinson, W. T.; Rodley, G. A. Structure of an iron(II) dioxygen complex; a model for oxygen carrying heme proteins. *Proc. Natl. Acad. Sci. U. S. A.* **1974**, *71*, 1326-1329.
- (62) Wayland, B. B.; Minkiewi, J. V.; Abdelmag, M. E. Spectroscopic studies for tetraphenylporphyrincobalt(II) complexes of Co, No, O₂, RNC, and (RO)₃p, and a bonding model for complexes of Co, No, and O₂ with cobalt(II) and iron(II) porphyrins. *J. Am. Chem. Soc.* **1974**, *96*, 2795-2801.

- (63) Guillard, R.; Fontesse, M.; Fournari, P.; Lecomte, C.; Protas, J. 1st peroxometalloporphyrin with dioxygen symmetrically bonded by both atoms - synthesis and x-ray crystal-structure of peroxotitaniumoctaethylporphyrin. *J. Chem. Soc., Chem. Commun.* **1976**, 161-162.
- (64) Hanson, L. K.; Hoffman, B. M. Griffith model bonding in dioxygen complexes of manganese porphyrins. *J. Am. Chem. Soc.* **1980**, *102*, 4602-4609.
- (65) Bai, Y.; Buchner, F.; Kellner, I.; Schmid, M.; Vollnhals, F.; Steinrueck, H.; Marbach, H.; Gottfried, J. M. Adsorption of cobalt (II) octaethylporphyrin and 2H-octaethylporphyrin on Ag(111): new insight into the surface coordinative bond. *New J. Phys.* **2009**, *11*, 125004.
- (66) Bagus, P. S.; Kaefer, D.; Witte, G.; Woell, C. Work function changes induced by charged adsorbates: origin of the polarity asymmetry. *Phys. Rev. Lett.* **2008**, *100*, 126101.
- (67) Laatikainen, R.; Ratilainen, J.; Sebastian, R.; Santa, H. NMR-study of aromatic-aromatic interactions for benzene and some other fundamental aromatic systems using alignment of aromatics in strong magnetic-field. *J. Am. Chem. Soc.* **1995**, *117*, 11006-11010.
- (68) Tachibana, J.; Imamura, T.; Sasaki, Y. A reversible metalloporphyrin oxygen carrier both in the solid state and in solution: preparation, characterization, and kinetics of formation of a molybdenum(VI) 5,10,15,20-tetramesitylporphyrin dioxygen complex. *Bull. Chem. Soc. Jpn.* **1998**, *71*, 363-369.
- (69) Chylarecka, D.; Kim, T. K.; Tarafder, K.; Mueller, K.; Goedel, K.; Czekaj, I.; Waeckerlin, C.; Cinchetti, M.; Ali, M. E.; Piamonteze, C.; Schmitt, F.; Wuestenberg, J. -.; Ziegler, C.; Nolting, F.; Aeschlimann, M.; Oppeneer, P. M.; Ballav, N.; Jung, T. A. Indirect magnetic coupling of manganese porphyrin to a ferromagnetic cobalt substrate. *J. Phys. Chem. C* **2011**, *115*, 1295-1301.

Conclusions and future work

This thesis focuses on the synthesis and characterisation of surface-confined metalloporphyrin systems. Distinct aspects of on-surface synthesis are investigated; namely, templated self-assembly, covalent coupling and axial coordination chemistry. Characterisation of the different metalloporphyrin systems has been performed under ultra-high-vacuum (UHV) conditions using scanning tunnelling microscopy (STM), low energy electron diffraction (LEED) and x-ray photoelectron spectroscopy (XPS). The following presents the principal conclusions of the thesis together with an outlook on the possible direction of future work.

6.1. Conclusions

6.1.1. Surface-templated assembly of nickel(II) porphine molecules

In Chapter 3, the templated self-assembly of (porphyrinato)nickel(II) (NiP) molecules on both the Ag(111) and Ag/Si(111)-($\sqrt{3} \times \sqrt{3}$)R30° (Ag/Si(111)- $\sqrt{3}$) surfaces is investigated. To this end, the growth and ordering of the NiP molecules on the Ag/Si(111)- $\sqrt{3}$ and Ag(111) surfaces have been examined using STM and LEED. The NiP molecules self-assemble on both Ag/Si(111)- $\sqrt{3}$ and Ag(111) surfaces, growing epitaxially in a manner consistent with coincidence on the former, and point-on-line (POL) coincidence on the latter. In both cases the coincident registry is achieved by an azimuthal rotation of the NiP overlayer lattice relative to that of the substrate. This results in the formation of mirror domains where the mirror plane follows substrate high symmetry directions. The angle between the mirror domains differs by only 2° for the different substrates, suggesting that

the large relative size of the overlayer unit cell together with the underlying three-fold symmetry are the principal factors governing the azimuthal rotation. Though the NiP molecules display the same closed-packed monolayer structure on both substrates, the configuration of the second overlayer differs significantly. While no transition from the lattice structure of the first layer is found on the Ag/Si(111)- $\sqrt{3}$ surface, the formation of parallel molecular rows aligned along the primitive lattice vectors of the underlying layer is observed on Ag(111). This suggests stronger intralayer interactions (relative to those between the overlayer and substrate) on the Ag(111) surface compared to Ag/Si(111)- $\sqrt{3}$.

6.1.2. On-surface synthesis of covalently coupled zinc(II) porphyrins

An investigation of the covalent coupling of [5,10,15,20-(tetra-5-bromothiophen-2-yl)porphyrinato]zinc(II) (ZnTBrThP) molecules on the Ag(111) and Au(111)-($22 \times \sqrt{3}$) surfaces is presented in Chapter 4. Here, the organisation and thermal lability of the ZnTBrThP molecules on the Ag(111) and Au(111)-($22 \times \sqrt{3}$) surfaces have been examined using STM, LEED and XPS. A pronounced substrate dependence is displayed in the assembly of the ZnTBrThP molecules on the Ag(111) and Au(111)-($22 \times \sqrt{3}$) surfaces. The molecular assembly on the Ag(111) surface is consistent with metal-directed polymerisation, where linkage of the ZnTBrThP molecules is mediated by coordination to substrate atoms via the bromothiophenyl groups; the abstraction of Ag atoms is revealed in the formation of substrate vacancy islands. Weaker substrate bonding of the ZnTBrThP molecules on the Au(111)-($22 \times \sqrt{3}$) surface permits a greater influence of direct intermolecular interaction in the self-assembled molecular overlayer. Here attractive dipole-dipole interactions between S and Br moieties of adjacent molecules can be expected to stabilise the observed face-to-face alignment of the bromothiophenyl groups. When adsorbed on both surfaces, the ZnTBrThP molecules display a latent thermal lability, which results in the fragmentation of the bromothiophenyl groups upon annealing. The elimination of the bromide moiety is common a feature on both the Au(111)-($22 \times \sqrt{3}$) and Ag(111) surfaces, however, in the latter case, the cleavage of the thiophenyl moiety is also observed. This effect is tentatively attributed to the apparent oxidative addition of substrate atoms to the bromothiophenyl groups of ZnTBrThP molecules adsorbed on the Ag(111) surface.

Subsequent on-surface covalent coupling follows a divergent linkage pattern. Despite the multiplicity of structural motifs, the principal linkages can be attributed to covalent coupling at either the meso-bridge carbons, or α carbons of the meso-thienyl groups.

6.1.3. Control of the axial coordination of a surface-confined manganese(III) porphyrin complex

In Chapter 5, the axial lability of chloro(5,10,15,20-tetraphenylporphyrinato)manganese(III) (Cl-MnTPP) molecules on the Ag(111) surface is investigated. In this regard, the conformation, thermal lability and oxygenation of Cl-MnTPP molecules on Ag(111) surface, have been examined using STM, LEED and XPS. The self-assembled Cl-MnTPP layer grows epitaxially on the Ag(111) surface, in a manner consistent with POL coincidence. The surface conformation of the Cl-MnTPP molecules is such that the axial Cl ligand points upwards relative to the Ag(111) surface. In this conformation the axial binding site at the vacuum interface is occupied by the Cl ligand; thus it can be expected that further axially coordination is inhibited. When adsorbed on the Ag(111) surface, the Cl-MnTPP molecules display a latent thermal lability which results in the dissociation of the Cl ligand upon annealing. The thermally induced dissociation of the Cl ligand occurs through a heterolytic cleavage of the metal-ligand bond, without the demetallation of the porphyrin complex. In this manner, an ordered array of coordinatively unsaturated MnTPP molecules is created, capable of axial coordination at the vacuum interface. Upon exposure of the MnTPP molecules to molecular oxygen, dioxygen axially coordinates to the central Mn atom in a symmetric edge-on geometry, consistent with a peroxo-like oxidation state. Irreversible oxidation through the formation a μ -oxo dimer species is prevented by the parallel alignment of the porphyrin macrocycle to the substrate, likely permitting the apparent hopping of the coordinated dioxygen to adjacent MnTPP molecules. The higher probability for a $(\sqrt{2} \times \sqrt{2})R45^\circ$ overlayer structure exhibited by the O_2 -MnTPP molecules, coincides with the coincident structure of the MnTPP lattice with that of the Ag(111) substrate. It follows, therefore, that the underlying adsorption site may influence the dioxygen adduct formation. Occupation of the initially lower probability sites for adduct formation give rise to a lateral molecular rearrangement; the resulting configurations of

adjacent phenyl groups reflect a transition to a higher energy arrangement. In addition to its apparent hopping, the coordinated dioxygen displays a thermally lability through which deoxygenation O₂-MnTPP molecules may be brought about; exposure to molecular oxygen results in adduct formation once again. As such, the oxygenation of the MnTPP molecules is reversible, with the molecular monolayer behaving as a so-called oxygen carrier. Oxygenation of the deposited Cl-MnTPP molecules is consistent with the degree to which the axial Cl ligand lost during thermal deposition. It follows that the presence of the axial Cl ligand inhibits the coordination of the dioxygen ligand.

6.2. Future work

6.2.1. Selective peripheral substitution of surface-templated metalloporphyrin assemblies

The surface-templated assembly of NiP molecules on both the Ag(111) and Ag/Si(111)- $\sqrt{3}$ surfaces presents a highly ordered scaffold for porphyrin derivatization. Distinct to their templated assembly, porphyrins in solution tend to self-organise into aggregate type structures.¹ In this regard, porphine undergoes selective mono-bromination at one of the eight open β -pyrrole positions to give 2-bromoporphine.² By contrast, the magnesium(II) chelate of porphine is found to undergo tetra-bromination at the four meso-carbon positions to give (5,10,15,20-mesotetrabromoporphine)magnesium(II).² Such halogenations of porphine and its metal chelates provide a view of the possible synthetic utility of surface-confined metalloporphyrins under UHV conditions. Due to the corrosive action of halogens on UHV components, however, controlled dosing necessitates *in situ* generation.³ A recognised method involves the use of an electrochemical source, in which a silver halide is electrolyzed to silver and halogen, for the generation and dosing of halogens in UHV - the source design and implementation are outlined in reference 3. This method facilitates the deposition of low halogen coverages at a controlled rate, making possible the study of on-surface reaction kinetics. Metalloporphyrins bearing low-spin d⁸ metals (such as Ni(II)) form predominantly square-planar complexes, which do not readily add further axial ligands.⁴ In addition, the introduction of a divalent metal produces a more electronegative porphyrin

ligand, activating substitution at the meso-carbon positions. Accordingly, the on-surface halogenation of self-assembled NiP molecules holds significant promise for a future study of site-selective peripheral substitution of surface-confined metalloporphyrins.

6.2.2. On-surface covalent coupling of metalloporphyrins catalysed by both intrinsic and extrinsic adatoms

Common to the thermally induced coupling of the ZnTBrThP molecules on both the Ag(111) and Au(111)-(22 × √3) surfaces is the elimination of the terminal bromide moiety. Here the resulting structural motif arises from covalent coupling at the α carbons of the meso-thienyl groups. Unique to the coupling reactions catalysed on the Ag(111) surface, however, is the cleavage of the thienyl moiety and the subsequent covalent coupling at the meso-bridge carbons. This has been tentatively attributed to the coordination of Ag substrate adatoms to the bromothienyl groups of the ZnTBrThP molecules. Similar coordination polymerization has previously been reported for pyridine-substituted porphyrins on both the Ag- and Cu- (111) surfaces; whereby coordination to intrinsic and codeposited (Cu) adatoms takes place via the pyridine end-group.⁵ Therefore, to further probe the nature of the adatom coordination (and contingent coupling), a control experiment on the Au(111)-(22 × √3) surface involving the co-deposition of Ag adatoms could be performed. Such a complementary study would yield a valuable insight into the coupling of metalloporphyrins catalysed by both intrinsic and extrinsic adatoms.

6.2.3. Axial coordination of dinitrogen to a surface-confined metalloporphyrin complex

The formation of a reversible dioxygen adduct of the surface-confined MnTPP molecules, with exposure to molecular oxygen, suggests that a similar approach could lead to analogous dinitrogen adduct. Nitrogen atom transfer reactions catalyzed by metal complexes are considered among the most attractive methodologies for the synthesis of nitrogen containing molecules.⁶ Complexes of manganese porphyrins are known to catalyze a wide range of reactions including alkane amination and alkene aziridination;⁷ the aza analogues of hydroxylation and epoxidation, respectively. The putative formation of a

dinitrogen adduct (or a metal nitrido complex) may yield a novel nitrogen source, eliminating the general need for source presynthesis⁸. As such, a future examination of the axial coordination of molecular nitrogen to surface-confined MnTPP molecules is of fundamental interest.

6.3. References

- (1) Ryan, A. A.; Cafolla, A. A.; Senge, M. O. Chemical synthesis in solution and Porphyrin nanostructures on surfaces - similar concepts, different results. *ECS Transactions* **2013**, *45*, 77-90.
- (2) Dogutan, D. K.; Ptaszek, M.; Lindsey, J. S. Direct synthesis of magnesium porphine via 1-formyldipyrromethane. *J. Org. Chem.* **2007**, *72*, 5008-5011.
- (3) Spencer, N. D., Goddard, P. J., Davies, P. W., Kitson, M., and Lambert, R. M. A simple, controllable source for dosing molecular halogens in UHV. *J. Vac. Sci. Technol. A* **1983**, *1*, 1554.
- (4) K. M. Kadish, K. M. Schmith, and R. Guilard, Ed. (2000) *The Porphyrin Handbook, Applications: Past, Present and Future*, Vol. 6. Academic Press: San Diego.
- (5) Heim, D.; Eciija, D.; Seutert, K.; Auwaerter, W.; Aurisicchio, C.; Fabbro, C.; Bonifazi, D.; Barth, J. V. Self-assembly of flexible one-dimensional coordination polymers on metal surfaces. *J. Am. Chem. Soc.* **2010**, *132*, 6783-6790.
- (6) Golubkov, G.; Gross, Z. Nitrogen atom transfer between manganese complexes of salen, porphyrin, and corrole and characterization of a (nitrido) manganese (VI) corrole. *J. Am. Chem. Soc.* **2005**, *127*, 3258-3259.
- (7) Fantauzzi, S.; Caselli, A.; Gallo, E. Nitrene transfer reactions mediated by metallo-porphyrin complexes. *Dalton Trans.* **2009**, *28*, 5434-5443.
- (8) Yu, X. Q.; Huang, J. S.; Zhou, X. G.; Che, C. M. Amidation of saturated CH bonds catalyzed by electron-deficient ruthenium and manganese porphyrins. A highly catalytic nitrogen atom transfer process. *Org. Lett.*, **2000** *2*(15), 2233-2236.

Publications

Referred papers

(1) Beggan, J. P.; Krasnikov, S. A.; Sergeeva, N. N.; Senge, M. O.; Cafolla, A. A. Control of the axial coordination of a surface-confined manganese(III) porphyrin complex. *Nanotechnology* **2002**, *23*, 235606.*

(2) Murphy, B. E.; Krasnikov, S. A.; Cafolla, A. A.; Sergeeva, N. N.; Vinogradov, N. A.; Beggan, J. P.; Shvets, I. V. Growth and ordering of Ni(II) diphenylporphyrin monolayers on Ag(111) and Ag/Si(111) studied by STM and LEED. *J. Phys.: Condens. Matter.* **2012**, *4*, 045005.

(3) Krasnikov, S. A.; Beggan, J. P.; Sergeeva, N. N.; Senge, M. O.; Cafolla, A. A. Ni(II) porphine nanolines grown on a Ag(111) surface at room temperature. *Nanotechnology* **2009**, *13*, 135301.*

(4) Beggan, J. P.; Krasnikov, S. A.; Sergeeva, N. N.; Senge, M. O.; Cafolla, A. A. Self-assembly of Ni(II) porphine molecules on the Ag/Si(111)-($\sqrt{3} \times \sqrt{3}$)R30° studied by STM/STS and LEED. *J. Phys.: Condens. Matter.* **2007**, *1*, 015003.*

Conference abstracts

(1) S.A. Krasnikov, C. Hanson, J.P. Beggan, D. Brougham, A.A. Cafolla, Electronic structure and surface conformation of TtertBuCuPc and TtertBuH₂Pc thin films on Ag/Si(111), Si(111) and SiO₂/Si(111) substrates studied by NEXAFS and XPS using synchrotron radiation and STM/STS. Abstracts of the 13th Intern. Conf. on Surface Science (ICSS-13), Stockholm, Sweden, July 2-6, 2007.

* Some parts of this thesis are published in the above papers.

(2) N.N. Sergeeva, S.A. Krasnikov, J.P. Beggan, M.O. Senge, A.A. Cafolla, Self-assembled layers of Ni(II) porphine on the Ag/Si(111) surface studied by STM/STS and LEED. Abstracts of the 6th annual CSCB symposium, Dublin, Ireland, December 14, 2007.

(3) S.A. Krasnikov, J.P. Beggan, N.N. Sergeeva, N.A. Vinogradov, M.O. Senge, A.A. Cafolla, Self-assembled layers of Ni(II) porphine and Ni(II) diphenylporphyrin on the Ag/Si(111)-($\sqrt{3} \times \sqrt{3}$)R30° and Ag(111) surfaces studied by STM/STS and LEED. Abstracts of the 3rd Intern. Conf. on Nanomaterials and Nanomanufacturing (Nano2007), Dublin, Ireland, December 17-18, 2007.

(4) A.A. Cafolla, S.A. Krasnikov, J.P. Beggan, N.N. Sergeeva, N.A. Vinogradov, M.O. Senge, Self-assembled layers of Ni(II) porphine and Ni(II) diphenylporphyrin on the Ag-passivated Si(111) and Ag(111) surfaces studied by STM/STS and LEED. Abstracts of the E-MRS 2008 Spring Meeting, Symposium Q (Functional supramolecular architectures for organic electronics and nanotechnology), Strasbourg, France, May 26-30, 2008.

(5) M. L. Ng, A. B. Preobrajenski, A. Zakharov, A. S. Vinogradov, S. A. Krasnikov, J. P. Beggan, A. A. Cafolla and N. Mårtensson, Epitaxially grown pentacene on the h-BN nanomesh. Abstracts of the International Conference on Functional Materials & Devices 2008 (ICFMD 2008), Kuala Lumpur, Malaysia, June 16-19, 2008.

(6) J. P. Beggan, S. A. Krasnikov, N. Boyle, M. T. Pryce and A.A. Cafolla, Self-assembly of Zn(II) tetrabromothienylporphyrin on the Ag(111) surface studied by STM and LEED. Abstracts of the 26th European Conference on Surface Science (ECOSS), Parma, Italy, August 30 - September 04, 2009.

Reaction schemes and molecular structures

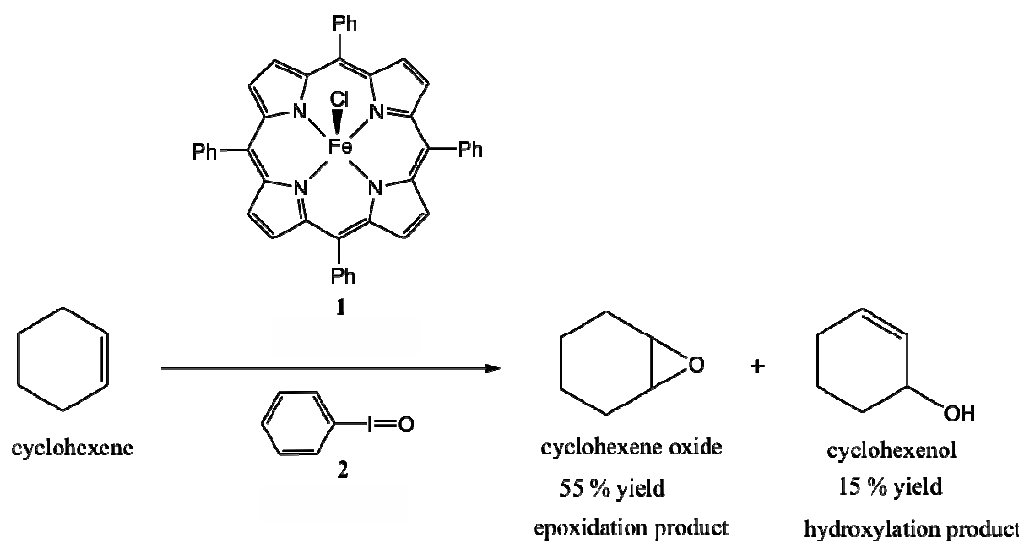


Figure 1. (1) chloro(5,10,15,20-tetraphenylporphyrinato)iron(III), (2) iodosobenzene.

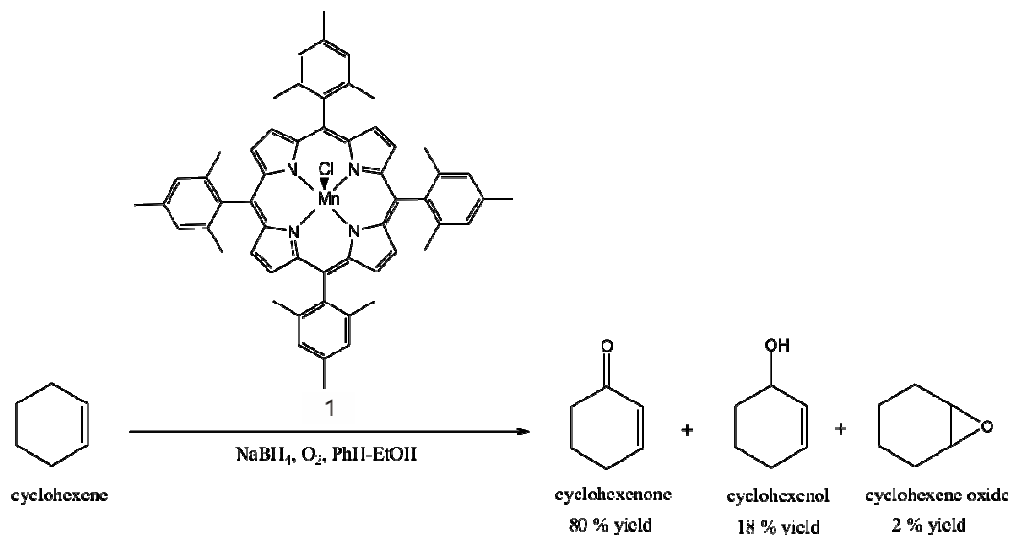


Figure 2. (1) chloro(5,10,15,20-tetramesitylporphyrinato)manganese(III).

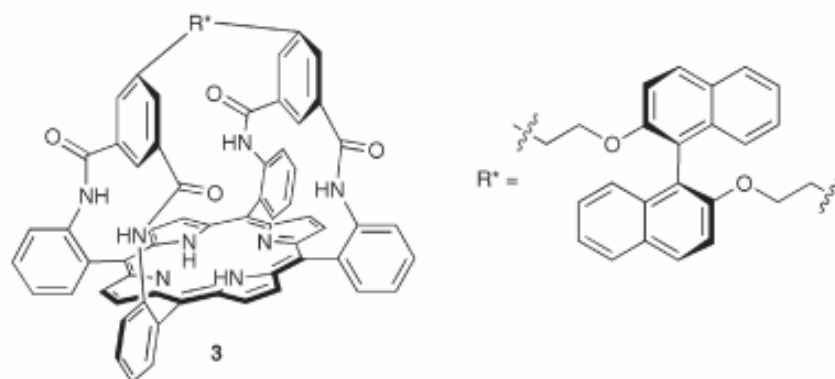


Figure 3. (3) The “picnic basket” porphyrin.

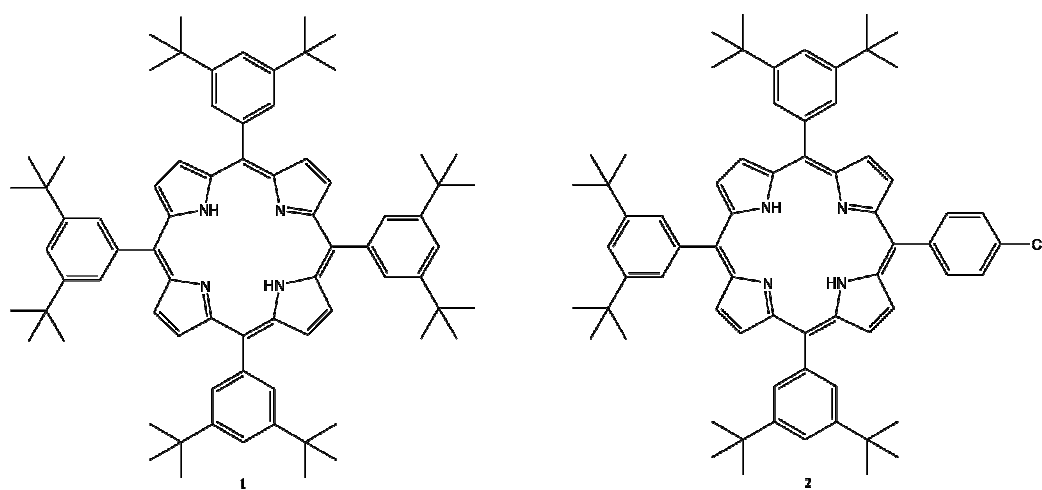


Figure 4. (1) 5,10,15,20-tetrakis-(3,5-di-tert-butylphenyl)porphyrin, (2) cyanophenyl substituted derivative.

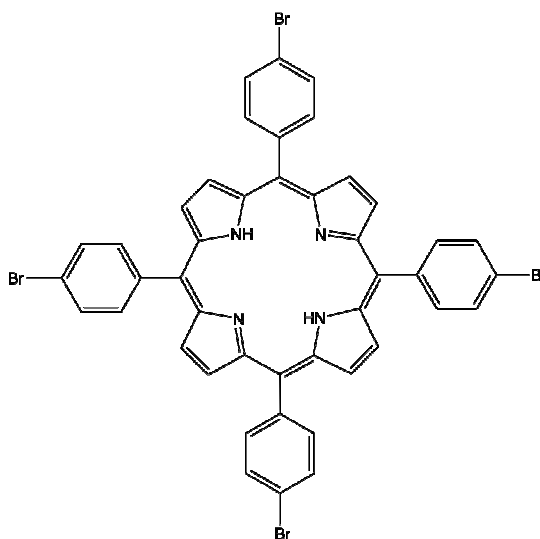


Figure 5. 5,10,15,20-tetrakis(4-bromophenyl)porphyrin.

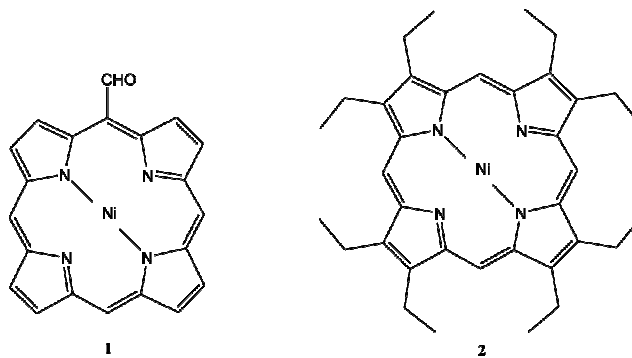


Figure 6. (1) nickel(II) porphyrin formylated at meso position, (2) nickel(II) octaethylporphyrin.

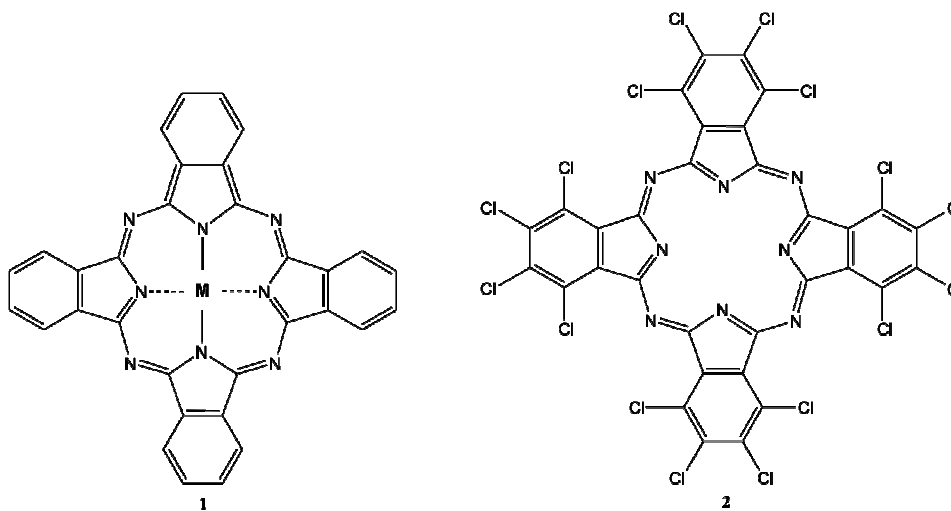


Figure 7. (1) metallophthalocyanine, (2) hexadecachlorophthalocyanine.

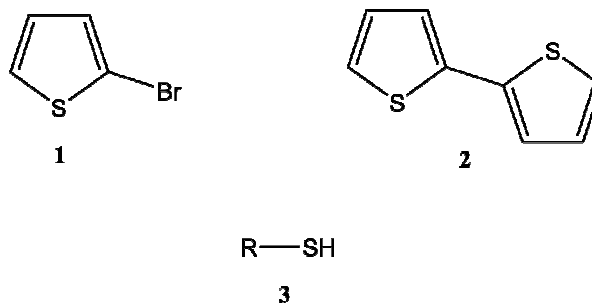


Figure 8. (1) 2-bromothiophene, (2) 2,2-bithiophene, (3) thiol moiety bound to alkane R.

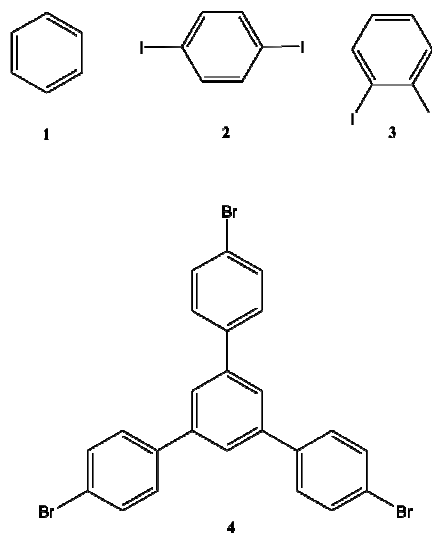


Figure 9. (1) benzene, (2) 1,2-diiodobenzene, (3) 1,3-diiodobenzene, (4) 1,3,5-tris(4-bromophenyl)benzene.

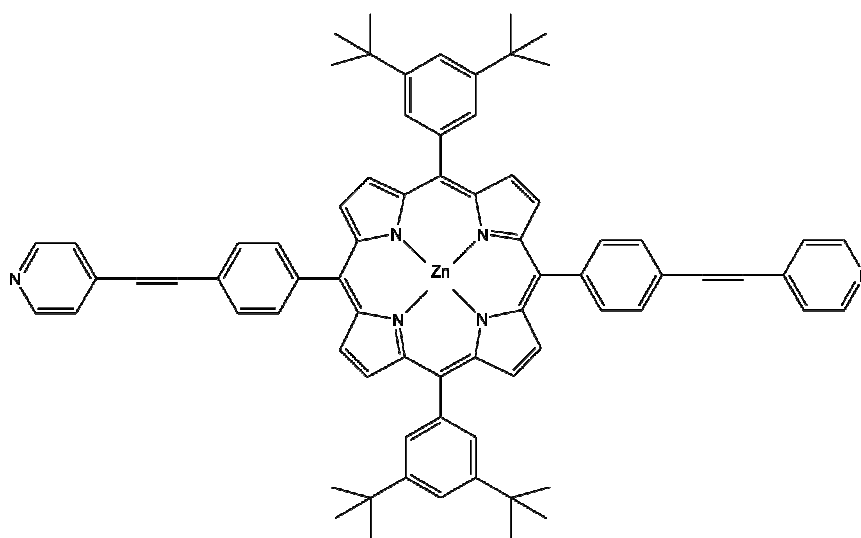


Figure 10. Porphyrin derivative presenting two phen-1,4-diyl-ethynyl-pyridyl and two 3,5-di-tert-butylphenyl substituents at the 5,15 and 10,20 meso-positions, respectively.

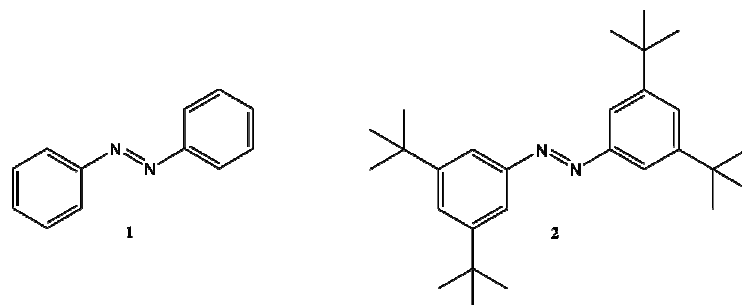


Figure 11. (1) azobenzene, (2) 3,3,5,5-tetra-*tert*-butylazobenzene.

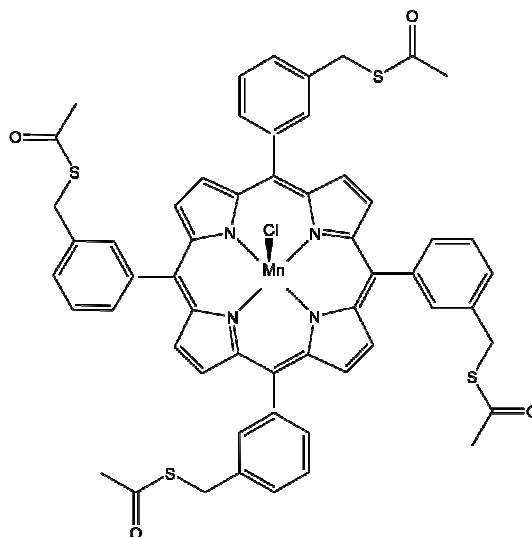


Figure 12. (acetyl-protected) thiol-terminated chloromanganese porphyrin.

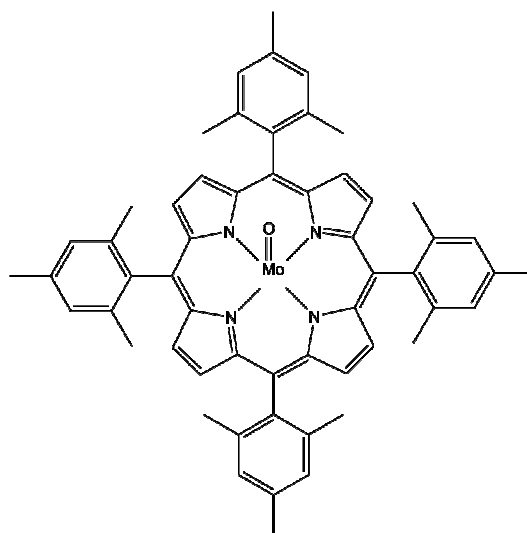


Figure 13. oxo(5,10,15,20-tetramesitylporphyrinato)molybdenum(IV).